A study of Spin Polarization in Potential Half-Metals

by

Eoin Aidan Clifford

A thesis submitted to the University of Dublin in application for the degree of Doctor of Philosophy

Department of Physics
Trinity College Dublin

October 2005

Declaration

This thesis is submitted by the undersigned for examination for the degree of Doctor of Philosophy at the University of Dublin. It has not been sub,itted as and exercise for a degree at any other university. This thesis, apart from the advice, assistance and joint effort mentioned in the acknowledgements and in the text, is entirely my own work.

I agree that the library may lend or copy this thesis freely on request

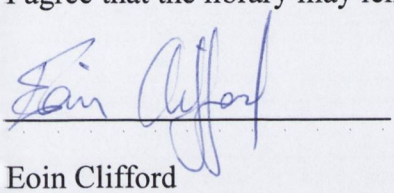

Eoin Clifford

Summary

The study presented in this thesis has been concerned with measuring spin polarisation in magnetic materials using two methods: i) measurement of magnetoresistance in room temperature point contacts and ii) Point Contact Andreev Reflection (PCAR). Two novel techniques were developed to measure PCAR data. One of these involved the use of an eight-step lithographical fabrication process to produce lateral nanojunctions. The second involved the use of an atomic-force microscopy (AFM) tip to puncture a nanohole in a soft polymer layer. A superconducting nanocontact was then deposited through this nanohole.

Huge magnetoresistance values were observed in several materials using the room temperature point contact method. A model was developed to explain these values, involving a combination of spin polarised electron transport through a domain wall and spin-polarised tunneling across a sharp interface. The method was used to estimate spin-polarisation values in several interesting and topical materials, giving an indication of there suitability for use in spin-electronic devices.

The first of the novel PCAR techniques, in which lateral nanojunctions were produced, was marginally successful. It was used to measure the spin-polarisation of nickel, giving a large value. As far as the author is aware this is the first time that an attempt has been made to measure the spin-polarisation of an in-plane current in a thin film system, and as such is a major development. However the difficulty in producing the devices required for this measurement technique meant that its applications are somewhat limited.

The second technique involves AFM nano-indentation. The technique was compared to a standard one used for these measurements involving a sharpened superconducting tip. Both techniques gave similar results, proving the suitability of our innovative method. However our technique has several advantages over this standard one. The profile of the point contact can be imaged, giving us an approximate value for the size of the nanocontact. Also, only one conduction path is created between the subject material and the superconductor. The standard method is believed to produce many conduction paths, which cause a smearing of the data and affect the measured polarization.

This procedure was used to examine some interesting materials. In particular, a film of ε-$Fe_{2-3}N$ was studied using this system, the first time that the spin polarisation of this material had been measured. The results obtained were interesting and significant; a high value of spin polarisation was observed, in spite of the materials low magnetic moment. This paves the way for more studies of this material, which is expected to generate significant interest within the scientific community.

Acknowledgements

First and foremost I would like to give thanks to Prof J. M. D. Coey for his support and guidance throughout the past four years. I would also like to thank everyone who has helped me in the lab over the last few years, starting with Janko who pushed me along the way with the point contact measurements (though I'm pretty sure he'll never read this), and Oscar for his work on the lateral nanojunctions and AFM, Millatron and FIB training. I also must give a big thank you to Plamen, who assisted me with the electrical measurements, evaporation, fitting, low-temperature measurements – I'm sure there was more. Big thanks to Venki for his help in producing all the materials, SQUID and VSM training, and for his general advice, both on magnetism and soccer gambling strategies. Thanks to Fernando for his help with electronics and for answering all my questions, to Richard for FIB training, to Sebastian, Emma, Matt and Gen Feng for making me films, and to Wang for working with me on the nanocontacts.

I would also like to thank Lucio for introducing me to the delights of local Brazilian radio advertising, and to Robbie for his meticulous monitoring of my sleeping habits (not as gay as it sounds – although considering some of the clothes he wears….). I would also like to thank everyone else on the front of this monthly report cover sheet I am looking at – Mazhar, Treasa, Adriele, Nandu, Gregory, Catherine, Anna, Karl, Ciaran, Peter and Chris.

Finally I would like to thank my family and also Aoife for giving me support and patience.

Table of Contents

Chapter 1

Introduction

The impact of the microchip on modern life cannot be overestimated - the times we live in now are often referred to as the Information Age, primarily due to the vast amounts of data accessible to people on the internet using just a simple PC and a telephone connection. People's desire for easier access to more information has driven scientific research at a hectic pace. The number of transistors that can be stored per unit area has been systematically doubling roughly every 18 months for the last 35 years in what has been dubbed "Moore's law", and the industry expect the trend to continue well into the next decade. A similar trend has been experienced with magnetic storage.

However for Moore's law to continue researchers have to keep finding new ways to downsize the fundamental devices required to store and process data. As a result, much research has been recently carried out on new types of electronic devices based on the spin of the electron. Precise control of the electron spin adds a new degree of freedom to the engineering of such devices. This research has already led to many developments, including the manufacturing of commercially viable products such as GMR based read heads and MRAM. Researchers hope that further developments in this new field of spin electronics will lead the way to the production of single electron transistors, which in turn would pave the way for a new wave of technological devices such as quantum computers.

The success of spin electronics may depend on the development of half metallic materials - that is materials where the electrons at the fermi energy are all of one spin direction. Such materials could provide fully spin-polarised currents, which is not possible with con-

ventional ferromagnets such as Fe, Co or Ni. In this thesis, I have examined the half metallic properties of a variety of materials.

1.1 Spin Transport

In the 1930's Mott [1] suggested a new model for electronic transport in metallic ferromagnetic materials. He proposed that currents in such materials could be divided into two distinct spin channels - one for spin up and one for spin down electrons. These channels would have different transport properties and would thus contribute differently to the electrical transport process. The difference in the properties of these two bands is due to the ferromagnetic exchange field. This creates different band structures for the spin up and spin down channels, thus affecting their density of states at the Fermi energy, which in turn affects their mobility and transport properties.

As electrons get scattered while travelling through a material, they can also undergo spin-flip scattering. This is a process where the electron is 'flipped' from one spin channel into another due to electron-electron collisions etc. The average path length an electron can travel before undergoing a spin-flip transition is known as the spin diffusion length, λ_{sd}, and is calculated using

$$\lambda_{sd} = \sqrt{\frac{\lambda \nu_F \tau_{\uparrow\downarrow}}{3}} \tag{1}$$

where λ is the mean free path, ν_F is the velocity of the spin (the Fermi velocity) and $\tau_{\uparrow\downarrow}$is the time taken for the spin to flip. An electron may experience many scattering events before there is one that flips its spin. As a rule of thumb, λ_{sd} is typically 10 times greater than λ.

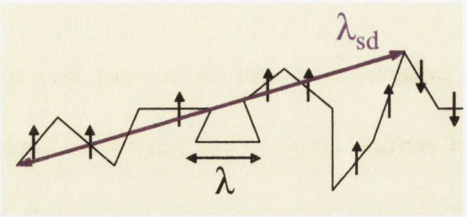

Figure 1.1 *Illustration of spin travelling through a material, where λ is the mean free path and λ_{sd} is the spin diffusion length*

Due to this relationship, factors which reduce the mean free path, such as impurities, will also reduce the spin diffusion length. Also, since the Fermi velocity and the mean free path may be different for each spin channel in a ferromagnet, λ_{sd} will be different for the spin up and spin down electrons. Spin diffusion lengths vary from microns in high purity metals to a few nm in silver doped with 10% Au. Detailed measurements of the diffusion length in various metallic multilayers have been made by Yang et al [2]. Impurities with strong spin-orbit coupling are efficient spin scatterers.

1.2 Spin Polarisation and half metals

For spin-electronics to be truly successful, it is necessary to be able to completely isolate the spin channels i.e. to be able to produce currents of one spin only. One method for producing such spin currents involves using materials where only spins of one direction are present at the Fermi energy. Such a material would thus only be able to provide electrons of one spin, and if it were to be used as an electrode in a device would provide a fully spin-polarised current.

Spin polarisation is a measure of the ratio of the electron density for each spin at the Fermi energy, and is generally given by

$$P_n = \frac{n_\uparrow - n_\downarrow}{n_\uparrow + n_\downarrow} \cdot 100\ \% \tag{2}$$

where P_n is the spin polarisation and $n_\uparrow, n_\downarrow$ are the spin up and spin down density of states at the Fermi level respectively. One major setback with this definition however is that it is only truly valid at zero temperatures - above 0 K the actual value of the spin polarisation is reduced by spin flip excitations, such as spin waves. A half metal is a metallic solid with $P_n = 100\%$.

For a half metal, the density of states at the Fermi energy differs significantly for majority and minority spins. For electrons of one spin it is a metal with a Fermi surface, but for the opposite spin there is a gap in the spin polarised density of states, as in a semiconductor or an insulator, and there is no Fermi surface. As a result of this only electrons of one spin direction contribute towards conduction. While half metals have to be ferromagnetic or ferrimagnetic, a ferromagnet is not necessarily a half metal. This is because the Fermi energy may cross unpolarised electron bands, such as the 4s bands in Fe, Ni, and Co, or else it may cross both $\uparrow$ and $\downarrow$ d-bands as in Fe.

The following nomenclature has been developed for half metals [3], [4]. Type IA (IB) are half metals that only have majority (minority) spin electrons appearing at the Fermi level. An example of a type IA half metal is CrO_2, where the 4s states are pushed above E_F due to hybridization with the O(2p) state, leaving only majority d electrons at the Fermi energy. Sr_2FeMoO_6 is a type IB half metal. In type II half metals, the electrons lie in a band that is sufficiently narrow for them to be localized. The heavy carriers may then form polarons, where conduction takes place via electron hopping between spin polarised sites. Fe_3O_4 is a type IIB material, where conduction takes place by $\downarrow$ electrons hopping between B sites in the spinel structure.

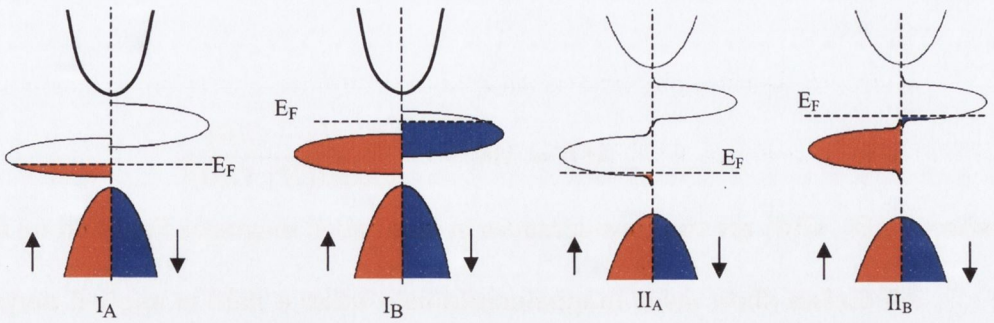

Figure 1.2 *Density of states for type I and type II half metals.*

Type III half metals have electrons of both spin directions at the Fermi level, however one of the spin bands is narrow enough to leave these electrons strongly localised. These heavy carriers contribute very little towards conduction. An example of such a half metal is $(La_{0.7}Sr_{0.3})MnO_3$. Type IV half metals are semimetallic half metals. A semimetal has small and equal number of holes and electrons because of a small overlap between the conduction and valence bands. In type IV half metals there is a huge difference in effective mass between the electrons and holes, and the conduction process is similar to that of a type III half metal.

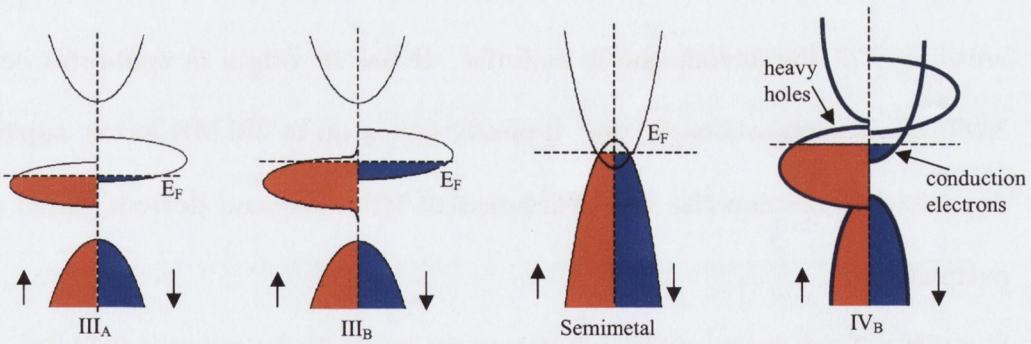

Figure 1.3 *Density of states for type III and type IV half metals, as well as for a semimetal*

1.3 Magnetoresistance

Magnetoresistance (MR) is when the resistance of a device changes upon application of a magnetic field. The definition used in this work is as follows

$$MR = 100\% \times \frac{G(H) - G(0)}{\max[G(H), G(0)]}, \tag{3}$$

where G(H), G(0) are the conductances in an applied magnetic field and no field respectively.

All metals show some magnetoresistance when a field is applied perpendicular to the current direction. This magnetoresistance is called normal magnetoresistance (NMR) and is caused by the Lorentz force, $\vec{F} = e\vec{v} \times \vec{B}$. Charge carriers experience the Lorentz force in the presence of an applied field and are then deflected from the current direction. This reduces the mean free path of the carriers and thus increases the resistance. For small fields the NMR has a B^2 dependence (the cyclotron effect). This dependence becomes linear and eventually saturates at higher fields. A typical value in normal metals is $\approx 0.1\%$ in 1 T. Semimetals such as bismuth exhibit higher values.

Higher values of magnetoresistance can be also observed in ferromagnetic materials, with the MR depending on the angle between the current and the magnetization of the sample. This form is called Anisotropic magnetoresistance (AMR) as it depends on the anisotropy of the ferromagnetic material. It has its origin in spin-orbit coupling [5]. The AMR effect is quite a useful one, typically giving up to 3% MR in low applied fields. It has been used to develop the first generation of MR read-head devices, based on the AMR of permalloy.

The dependence of the resistance on an applied magnetic field for a ferromagnetic material can be represented by the following equation

$$\overrightarrow{E} = \rho_{perp}(B)\vec{j} + [\rho_{para}(\vec{B}) - \rho_{perp}(\vec{B})](\overrightarrow{M}.\vec{j})\overrightarrow{M} + \rho_H(\vec{B})\overrightarrow{M} \times \vec{j} + \rho_{DW}(\vec{B})\vec{j} \tag{4}$$

where $\overrightarrow{E}$ is the electric field, $\overrightarrow{M}$ is the magnetic moment, $\overrightarrow{j}$ is the current density, and ρ_{perp} and ρ_{para} are the perpendicular and parallel components of the resistivity. The first term in

this equation accounts for the NMR and the second term accounts for the AMR. The third term (the ρ_H term) takes into account the Hall effect (both ordinary and extraordinary) and the fourth (the ρ_{DW} term) is the change in resistivity due to spin diffusion. This final term can give the greatest values of magnetoresistance and accounts for the giant magnetoresistance (GMR) effect. It also accounts for effects caused by domain wall scattering.

Another form of magnetoresistance is powder magnetoresistance (PMR) [6]. PMR occurs in pressed powders of metallic materials. The resistance of these pressed pellets is dominated by the interparticle contacts. The relatively high resistance of these pressed pellets as compared to single pieces suggests that the intergranular contacts are mostly tunnel barriers rather than metallic point contacts. Nevertheless, it is likely that there will be a very broad distribution of contact resistances, ranging from milliohms to gigaohms, and that the conduction is confined to a limited number of highly conducting paths through this random resistor network.

It is easy to reduce the number of these highly-conducting paths by diluting the conducting powder with an insulating powder of similar particle size. Close to the percolation threshold the conduction is restricted to a small number of paths which may involve grains which are surrounded by tunnel barriers. The maximum MR that could be expected in a type I or type II half-metallic powder compact can be deduced by assuming that the magnetization directions are random in the zero-field state, and fully aligned in a sufficiently large applied field. Transmission when electron transport is uninfluenced by any domain wall at the contact between two grains i and j is given by

$$T = \cos^2\left(\frac{\theta_{ij}}{2}\right) = \frac{1}{2}(1 + \cos(\theta_{ij})), \tag{5}$$

where θ_{ij} is the misalignment of the magnetization between the two grains. However, if the directions of magnetization on either side of the contact are random, the mean value of $\cos(\theta_{ij})$ becomes zero; hence, T changes from $\frac{1}{2}$ in the random case to 1 in the fully aligned case. Since the conductance is proportional to the transmission, the maximum observable PMR is 50%. This will be reduced if there is any tendency to alignment of the magnetization of contiguous grains in zero field, as might be expected in a remanent state after saturation of the magnetization. If the material is imperfectly polarized, the maximum MR is

$$MR = \frac{P^2}{1+P^2} \times 100\%. \tag{6}$$

1.4 Spin Electronics

Conventional electronics has ignored the spin of the electron [7]

Up until recently electronic devices were based solely on the principle of manipulating electron charges using electric fields. However these neglect the fact that the electron is a magnet of its own right (a free electron has a magnetic moment of μ_B) which can thus be manipulated using magnetic fields. Making use of the spin in an electron adds a new degree of freedom. Within the past 17 years devices have been developed which do make use of this property of the electron. Such devices - called spin electronic devices - are primarily based on magnetoresistance effects, primarily GMR and TMR.

The GMR effect was discovered in the late 1980s by two European scientists working independently: Peter Grunberg of the KFA research institute in Julich, Germany [8], and Albert Fert of the University of Paris-Sud [9]. They saw quite large resistance changes – 6 percent and 50 percent, respectively – in devices comprising of alternating very thin layers of ferromagnetic and non-ferromagnetic elements. These results were only obtained at low

temperatures and in the presence of very high magnetic fields, and thus the devices were unsuitable for mass production. However their results inspired further research to optimize the necessary properties and it wasn't long before room-temperature GMR devices were being manufactured on an industrial scale. Many of the pioneering developments that took place were carried out by Stuart Parkin and his colleagues in IBM [10], [11].

The spin-valve was the first device to make use of the GMR effect. It consists of two ferromagnetic layers separated by a non-magnetic spacer layer. This structure was then modified slightly by the addition of an antiferromagnetic layer. One of the ferromagnetic layers, called the pinned layer, is adjacent to the antiferromagnetic layer, thus coupling with it so that the orientation of its magnetisation does not change. The other ferromagnetic layer is called the free layer as the orientation of its magnetisation can be easily switched by application of a small magnetic field. When the alignment of the magnetic layers is switched from parallel to anti-parallel the resistance of the device increases. GMR values are generally much larger than those obtained by AMR and as a result spin-valve read heads have taken over the market. A good review of the GMR effect can be found in [12].

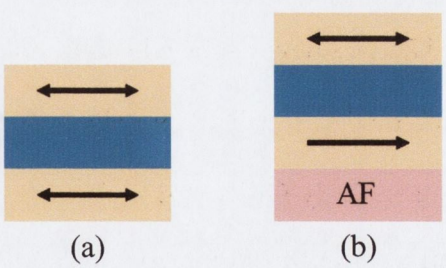

Figure 1.4 *(a) The original spin valve structure where both ferromagnetic layers (orange) are free to change the direction of their magnetisation and (b) the direction of magnetisation of the lower ferromagnetic layer is pinned by the antiferromagnetic (AF) layer*

Another device similar in structure is the Magnetic Tunnel junction (MTJ). MTJ's are based on what is called Tunneling magnetoresistance (TMR) [13]. MTJ's are very similar

structures to spin valves, except a very thin insulating tunnel barrier is now used to separate the two ferromagnetic layers, and the current is passed perpendicular to the plane. When the ferromagnetic layers are aligned anti-parallel, it is difficult for electrons to tunnel from one layer to the other since there may be few or no vacant states of the correct spin in the case of a half metal, and as a result the resistance of the device is relatively high. This drops significantly upon application of a field to align the layers parallel, and large (up to 69% using eq. (3) at room temperature [14]) values of MR are achieved.

For both TMR and GMR, the MR is related to $P_1$and P_2, the spin polarisation of the two ferromagnet layers, by the Jullière formula [15]

$$MR = \frac{2P^2}{1+P^2}. \tag{7}$$

From this it is clear that to have more efficient spin-electronic devices we need materials with as high a spin polarisation as possible. A review of recent advances in the field of spin electronics is given by Bobo et al [16]. Other good reviews can be found in [17] and [18].

References

[1] N. F. Mott, Proc. R. Soc., **153** 699 (1936).

[2] Q. Yang, P. Holody, S. F. Lee, L. L. Henry, R. Loloee, P. A. Schroeder, W. P. Pratt, Jr., and J. Bass, Phys. Rev. Lett. **72,** 3274 (1994).

[3] J. M. D. Coey and M. Venkatesan, J. Appl. Phys. **91,** 8345 (2002).

[4] J. M. D. Coey and C. L. Chien, MRS Bulletin **28,** 720 (2003).

[5] V. A. Marsocci, Phys. Rev. **137,** 1842 (1965).

[6] J. M. D. Coey, A. E. Berkowitz, L. I. Balcells, F. F. Purtis, and A. Barry, Phys. Rev. Lett. **80,** 3815 (1998).

[7] J.M.D. Coey in "Spin electronics", M. Ziese and M.J. Thornton eds., Springer (2001).

[8] G. Binasch, P. Grunberg, F. Saurenbach, and W. Zinn, Phys. Rev. B **39**, 4828 (1989).

[9] M. N. Baibich, J. M. Broto, A. Fert, F. Nguyen Van Dau, F. Petroff, P. Etienne, G. Creuzet, A. Friederich, and J. Chazelas, Phys. Rev. Lett. **61**, 2472 (1988).

[10] B. Dieny, V. S. Speriosu , S. S. P. Parkin, B. A. Gurney, D. R.Wilhoit, and D. Mauri, Phys. Rev. B **43,** 1297 (1991).

[11] S. S. P. Parkin, R. Bhadra, and K. P.Roche, Phys. Rev. Lett. **66,** 2152 (1991).

[12] B. Dieny, J. Magn. Magn. Mater. **136,** 335 (1994).

[13] J. S. Moodera, L. R. Kinder, T. M. Wong and R. Meservey, Phys. Rev. Lett. **74,** 3273 (1995).

[14] S. S. P. Parkin, C. Kaiser, A. Panchula, P. M. Rice, B. Hughes, M. Samant, S.H. Yang, Nat. Mater. **3**, 862 (2004).

[15] M. Jullière, Phys. Lett. A, **54,** 225 (1975).

[16] J. F. Bobo, L. Gabillet and M. Bibes, J. Phys.: Condens. Matter **16,** S471 (2004).

[17] G. Prinz, Science **282**, 1660 (1998).

[18] S. A. Wolf, D. D. Awschalom, R. A. Buhrman, J. M. Daughton, S. von Molnar, M. L. Roukes, A. Y. Chtchelkanova, and D. M. Treger, Science **294,** 1488 (2001).

Chapter 2

Theory

2.1 Point Contacts

A point contact is a small region of atomic scale continuity between two crystallites. Unlike a nanoconstriction, there is generally no crystallographic coherence across the contact, and a grain boundary is present. Point contacts are made by bringing two pieces of a material together until they touch, then slowly pulling them apart. The region of contact between two pieces of metal may stretch out, like chewing gum, forming a narrow neck or nanoconstriction. In the following section we will go through some of the basic physical processes which are important in electron transport through point contact geometries.

2.1.1 Ballistic Transport and Quantised Conductance

Ballistic transport is when an electron can pass through a region (such as a point contact) without being scattered. This requires that the radius of the contact, r, is smaller than the mean free path of the electron, λ, and thus the only collisions are elastic collisions at the edge of the contact. The resistance R of such a contact is given by the Sharvin formula [1]

$$R = \frac{h}{2e^2}\frac{4\pi}{k_F^2 A} \tag{1}$$

where k_F is the Fermi wave vector and A is the cross sectional area of the contact. For a circular contact in copper ($k_F = 1.36 \times 10^{10}$ m^{-1}), with a radius of 10 nm, this would give a resistance of 2.8 Ω.

For extremely small contacts the conductance becomes quantized. Consider two elec-

tron gas reservoirs connected by a nanoconstriction with a radius r. Since $r < \lambda$, transport through the constriction should be ballistic. The electrons would then behave like a 1-D electron gas: the momentum will be quantised in the x and y directions (assuming transport is in the z direction). The energy of the electron is described by the following

$$E_n(k) = (n_x^2 + n_y^2)\frac{\pi^2\hbar^2}{4mr^2} + \frac{\hbar^2 k_z^2}{2m} \tag{2}$$

where n_x and n_y are the indices for the discrete allowed transverse modes, m is the electron mass and k_z is the component of the wave vector in the z-direction. The first term on the right hand side of equation (2) is the quantized term, while the other term represents the continuous contribution in the z direction. Applying a small potential difference between the two reservoirs, $V_{bias} = (\mu_1 - \mu_2)/e$, leads to a difference in chemical potentials $(\mu_1 - \mu_2)$. The number of electrons N then contributing to the current is:

$$N = \frac{1}{2} g_n(E_F)\,(\mu_1 - \mu_2)\,, \tag{3}$$

with $g_n(E_F)$ the density of states at the Fermi level for mode n. This leads to an expression for the charge current I_n due to mode n

$$I_n = e v_{Fn} N = \frac{e v_{Fn}}{2} g_n(E_F)\,(\mu_1 - \mu_2)\,, \tag{4}$$

with v_{Fn} the group velocity of mode n at the Fermi level. The density of states at the Fermi level for a 1D electron gas is given by

$$g_n(E_F) = \left(2\pi \frac{dE_n(k)}{dk}\right)^{-1} = \frac{1}{h v_{Fn}}. \tag{5}$$

Finally, substituting equation (5) into (4) gives a conductance G_0 per mode of

$$G_0 = \frac{I_n}{V_{bias}} = \frac{2e^2}{h}, \tag{6}$$

or for the total conductance G

$$G = NG_0 = \frac{2e^2}{h}N, \tag{7}$$

with N the number of available modes below the Fermi level.

When changing the size of the constriction, we see from (1) and (2) that the number of allowed modes available for transport changes too, and this leads to a stepwise change in the observed conductance. For constrictions a few atoms in size, the energy level spacing becomes larger than the thermal energy, and conductance quantization can be observed at room temperature.

In the above derivation it is assumed that each electron emitted from the left reservoir will reach the right reservoir and vice versa. This implies complete transmission for each electron wave in each mode. In general, this condition need not hold, and this leads to the Landauer formula, a generalization of equation (7).

$$G = \frac{e^2}{h}\left(\sum_{1}^{N_\uparrow} T_{i\uparrow} + \sum_{1}^{N_\downarrow} T_{i\downarrow}\right), \tag{8}$$

where the conductance is the sum over all available modes of the spin-dependent transmission probabilities T_i. For systems with spin degeneracy, and completely open or closed modes (T_i either 0 or 1), the Landauer formula reduces to equation (7). The factor 2 in (7) comes from spin degeneracy, and some authors [2], [3] claim to have removed this degeneracy by application of a magnetic field, giving conductance steps of e^2/h.

This quantization of the conductance is only possible at a nano-sized, impurity-free region, and thus its observation requires the fabrication of samples of that scale and purity. As a result this effect was not experimentally observed until 1988, when Van Wees et al. [4] measured the transport through a small constriction in a two dimensional electron gas (2DEG) where the width of this constriction was varied. This quantization has since been system-

atically observed in electrodeposited, point and breaking metallic contacts. Widespread use is made of STM, where the tip is driven into the sample and then pulled back. This causes a nanowire to be formed, a behaviour similar to pulling some chewing gum apart. Both the electrical and mechanical properties of these nanowires can then be measured ([5]-[8]). A good review of the field is given in [8]

Mechanically-controlled break junctions, where the resistance of a wire is monitored while it is breaking, allow the measurement of quantum conductance steps. This was first demonstrated at the start of the 90s by Muller et al. [9] and has been used more recently to successfully measure the magnetoresistance of atomic nickel contacts [10].

2.1.2 Domain Walls

In a ferromagnet, electrons tend to align in the same direction because of the exchange interaction. These interactions are a direct consequence of Pauli's exclusion principle, which is due to the fermionic nature of the electron itself. In an infinite bulk sample at zero Kelvin, the ground state would therefore be a homogeneously magnetized single domain. In finite samples however, one single domain would lead to magnetic charges at the surface, and with it demagnetizing fields H_d. This would increase the magnetostatic energy of the system by $-\frac{1}{2}\mu_0 \overrightarrow{H_d} \cdot \overrightarrow{M}$ (this is positive as both H_d and M are oppositely directed). This is why, in a non-magnetized ferromagnetic material, the electron spins in the whole material are not aligned. Rather, they organize into magnetic domains in which the electrons spin in one direction.

This multiple domain structure, with alternating directions of magnetization [11] implies that, in between domains, the magnetization vector has to rotate from one direction to another. The resulting magnetic structure is called a domain wall. The rotation can be

parallel (Bloch) or perpendicular (Néel) to the direction of the domain interface, as depicted by figure 2.1. In bulk structures, Bloch walls are energetically favorable, however Néel walls are more common in thin films.

Clearly, the magnetization in a domain wall is non-uniform, leading to an increase in exchange, anisotropy and dipole energies. The process of domain formation is therefore a balance between the energy cost of forming the domain walls and the decrease in the magnetostatic energy. This balance will determine the number and size of the domains. If the magnetostatic energy is very small, it is easy to form a single domain state. As this energy increases, more and more smaller domains form until you get to the limit of a normal metal.

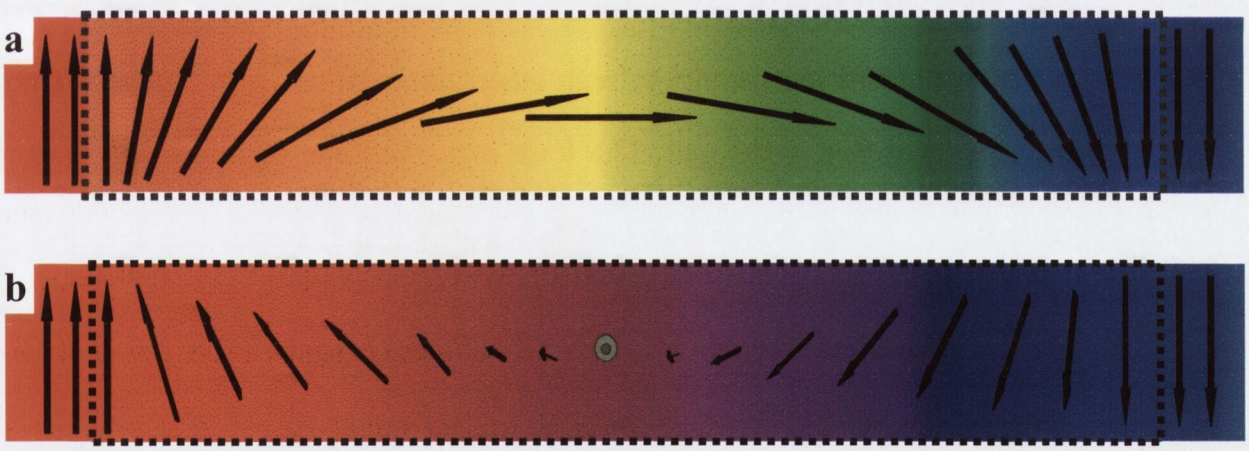

Figure 2.1 *Magnetic domain walls. a) Rotation in plane of the magnetization (Neel wall) and b) rotation out of plane (Bloch wall). Neel walls are energetically favourable for thin films. The change from out of plane to in plane for permalloy films occurs at about 30 nm.*

The width of a domain wall [12], or how quickly the moments rotate from one direction to the other, is determined by the exchange energy and the anisotropy. The former favors a parallel alignment of the moments, which tends to broaden the wall, with only a very gradual rotation of the magnetization vector. The latter favors an abrupt change and hence

a narrow wall. The total energy E of the wall, is given by

$$E = E_{ex} + E_a + E_d = \int_{-\infty}^{\infty} \left[A \left(\frac{\partial \theta}{\partial z} \right)^2 + f_a(\theta) - \frac{1}{2} \mu_0 \overrightarrow{H_d} \cdot \overrightarrow{M} \right] dV, \tag{9}$$

where A is the exchange stiffness, f_a is the anisotropy energy density and θ is the rotation of the magnetization between two adjacent moments in the rotation axis. E_{ex}, E_a, and E_d are the exchange, anisotropy and demagnetisation energies respectively. Here we neglect energy due to applied stress and magnetostriction. A stable wall configuration requires a minimization of the total energy with respect to the rotation of magnetization; $\frac{\partial E}{\partial \theta} = 0$.

The commonest type of domain wall is the 180° Bloch wall where the magnetization rotates in the plane of the wall. The Bloch wall has the remarkable property that it creates no divergence of the magnetization. Each of the three terms in $\nabla \cdot M$, $\partial M_x/\partial x + \partial M_x/\partial x + \partial M_x/\partial x$ is zero; there is no component of magnetization in the x-direction, and the spins in each $yz-$plane are parallel to each other. Since $\nabla \cdot M = 0$, there are no sources of demagnetizing field in the wall. This leads us to the Euler equation for a Bloch wall:

$$\frac{\partial f_a}{\partial \theta} - 2A \frac{\partial^2 \theta}{\partial z^2} = 0. \tag{10}$$

For the uniaxial anisotropy case, with $f_a = K_u \sin^2 \theta$, where K_u is the uniaxial anisotropy constant, the wall profile can be calculated analytically:

$$\theta(z) = \arctan \left[\sinh \left(\frac{\pi z}{\delta_w} \right) \right] + \frac{\pi}{2}, \tag{11}$$

where $\delta_w = \pi (A/K_u)^{\frac{1}{2}}$ is the domain wall width. Typical values for δ_w in bulk are given in table 2.1.

Material	A (pJm^{-1})	K (kJm^{-3})	δ_w (nm)
Permalloy	10	0.15	810
Fe	8	50	40
Co	10	530	14
$Nd_2Fe_{14}B$	8	4900	3.9

Table 2.1 *Domain wall width δ_w for 3d ferromagnets, permalloy and an Nd-Fe-B magnet.*

2.1.3 Domain Wall Resistance

The resistivity of a ferromagnetic metal can be expressed as:

$$\rho(T) = \rho_i + \rho_{ph}(T) + \rho_{e-e}(T) + \rho_m(B,T), \tag{13}$$

where ρ_i is the intrinsic resistivity of the material, ρ_{ph} is due to electron-phonon interaction (which depends on the temperature), ρ_{e-e} is the electron-electron interaction (neglected in a free electron model) and ρ_m is the contribution due to magnetic fields or scattering with domain walls and spin disorder.

The magnetic contribution to the resistivity can be found from the general expression for the electric field in ferromagnetic materials in the presence of a magnetic field (see eq. 1.4). The domain wall magnetoresistance in a classical approximation [13], [14] is due to the changing local magnetic field experienced by a single electron, and the resultant misalignment of the electron spin with this field, which leads to the expression:

$$\frac{\Delta R_w}{R} = \frac{2p}{(1-P)^2}\left(\frac{\hbar v_F}{J_{ex}}\right)\frac{1}{\delta_w^2}, \tag{14}$$

with J_{ex} the exchange energy, P the polarization of the material and δ_w the domain wall width. The estimated increase in resistance in (Bloch) domain walls for 3d ferromagnets is given in table 2.2.

	Fe	Co	Ni
$\frac{\Delta R_w}{R}$	1.3 %	7.1 %	1.2 %

Table 2.2 *Magnetoresistance due to domain wall scattering calculated from* (14).

In a quantum model, the resultant magnetoresistance for a current perpendicular or parallel to the domain wall is [15]

$$\begin{aligned} \frac{\delta\rho_{perp}}{\rho_{perp}} &= \left[\frac{\xi^2}{5}\frac{\left(\rho^{\uparrow}-\rho^{\downarrow}\right)^2}{\rho^{\uparrow}\rho^{\downarrow}}\left(3+\frac{10\sqrt{\rho^{\uparrow}\rho^{\downarrow}}}{\rho^{\uparrow}+\rho^{\downarrow}}\right)\right] \\ \frac{\delta\rho_{para}}{\rho_{para}} &= \frac{\xi^2}{5}\frac{\left(\rho^{\uparrow}-\rho^{\downarrow}\right)^2}{\rho^{\uparrow}\rho^{\downarrow}}, \end{aligned} \tag{15}$$

where $\xi \equiv \dfrac{\pi\hbar k_F}{4mJ\delta_w}$, ρ_{perp} and ρ_{para} are the perpendicular and parallel components of the resistivity, and $\rho^{\uparrow}$ and $\rho^{\downarrow}$ are the resistivities for each spin channel. Again the increase in resistance scales as R_w^{-2}.

In the above calculations, the geometry of the sample is assumed to be of no importance, however this is untrue as we approach the nanometre scale. Bruno calculated the structure and properties of a geometrically constrained domain wall in a nanoconstriction separating two wider regions [16]. He found different analytical expressions for the domain wall width depending on the model used (see table 2.3).

Model	Shape	Formula	δ_w
I	isthmus	$S = \begin{cases} S_0 \text{ for } \lvert x\rvert \leq d \\ S_1 > S_0 \text{ for } \lvert x\rvert \geq d \end{cases}$	$\frac{8d}{\pi^2}$
II	hourglass	$S = S_0\left(1 + \frac{x^2}{d^2}\right)$	$\frac{8d}{\pi}$
III	hourglass	$S = S_0 \cosh(x/d)$	$2d$

Table 2.3 *Expressions for domain wall width at nanoconstriction calculated for three different geometrical constraints* [16] *(S is width of structure, d is size of constriction).*

One remarkable result of the calculation is that for these nano-scaled constrictions, the domain wall width is independent of material parameters and depends only on the geometry of the constriction. Now the width δ_w will depend only on the size of the constriction, d. These results are confirmed by Monte Carlo simulations of "isthmus" and "hourglass" geometries (similar to Model I and II, respectively) [17]. These simulations also show that the wall goes from a Néel-like configuration for narrow constrictions, via a cross-over region to Bloch-type for larger constrictions due to the demagnetising energy E_d. In the absence of this term, the wall would always be Bloch-type. The Monte Carlo simulations also indicated that there are thermally-excited fluctuations between a Néel-type and a Bloch-type domain walls with different chirality depending on the shape and size of the point contacts [17], [18].

In the bulk, the domain wall width δ_w is much larger than the Fermi wave length λ_F, whereas for nanometric constrictions, the wall can become very narrow, in fact, as narrow as the constriction itself. This has important implications for the resistivity of the domain wall. The wall energy γ_w, which is $2\sqrt{AK}$ for a bulk wall, is now $\frac{\pi^2 A S_0}{2d}$ for the "isthmus" geometry, i.e. independent of the anisotropy constant K. Since the width of the domain wall will be roughly the size of the constriction, it could be possible to increase the contribution of the domain wall resistance to the total resistance merely by decreasing the size of the constriction.

This could be a way to increase the magnetoresistance of nano-scaled structures for sensor applications.

2.1.4 Tunneling

When an electron encounters an energy barrier whose height is bigger that an applied difference of potential, the electron can still cross the barrier thanks to its quantum-wave behaviour. In a point contact, this barrier will usually consist of a narrow insulating region between two conductive crystallites. Since it is at the interface of the point contact, this barrier is essentially of one-dimensional nature in the direction of the electron flow.

For a square barrier ($\sim$ square well) the Schrödinger equation will have the simple form

$$E\psi = \left(\frac{p^2}{2m} + V\right)\psi, \tag{16}$$

where m is the electron mass, p the linear momentum, ψ the wave function, E the energy of the electron and V is constant in a given region. The general solution of (16) has the well-known form

$$\psi(x) = ae^{ikx} + be^{-ikx}, \tag{17}$$

$$\frac{\hbar^2 k^2}{2m} = E - V. \tag{18}$$

When $E - V > 0$ the wave functions are plane waves. When $E - V < 0$ we will write $\kappa = ik$ and

$$\psi(x) = ae^{-\kappa x} + be^{\kappa x}. \tag{19}$$

If we assume real plane waves in regions I and III (figure 2.2 a and b) and tunneling in region II, and defining k_j (κ_j) with j=1,2,3 as the k (κ) vector at the j region, we can neglect $e^{-\kappa_2 w}$ in comparison to $e^{\kappa_2 w}$; in other words, we consider only a strongly attenuating barrier. Then

we have

$$a_3 = \frac{4k_1\kappa_2\varphi e^{-\kappa_2 w}}{\left(k_1^2+\kappa_2^2\right)^{\frac{1}{2}}\left(k_3^2+\kappa_2^2\right)^{\frac{1}{2}}}a_1, \tag{20}$$

$$\varphi = ie^{-i\alpha}\exp\left(ik_1x_1 - ik_3x_2\right). \tag{21}$$

The wave functions are now exponentially growing and decaying waves characteristic of barrier penetration problems. In a square, strongly attenuating barrier, it can be shown [19] that the ratio of the transmitted current j_t to the incident current j_i is

$$\frac{j_t}{j_i} = \frac{16k_1k_3\kappa_2^2}{\left(k_1^2+\kappa_2^2\right)\left(k_3^2+\kappa_2^2\right)}e^{-2\kappa_2 w}. \tag{22}$$

In typical problems of interest the barrier penetration factor $e^{-2\kappa_2 w}$ may be 10^{-5}-10^{-10}, so that it tends to dominate (22). This factor can seldom be calculated accurately, so that usually any experimental determination of the prefactor is doubtful or impossible [20].

The resistance and current, assuming that the electron conserves its energy when it tunnels through the barrier, can be approximated to

$$R_T \propto \exp\left[\left(\frac{2t}{\hbar}\right)(\varphi m)^{\frac{1}{2}}\right], \tag{23}$$

$$I \propto V\exp\left[-\left(\frac{2t}{\hbar}\right)(\varphi m)^{\frac{1}{2}}\right], \tag{24}$$

where t is the separation distance between the metallic electrodes and φ the work function. Note that a small change in the separation distance would change the resistance significantly.

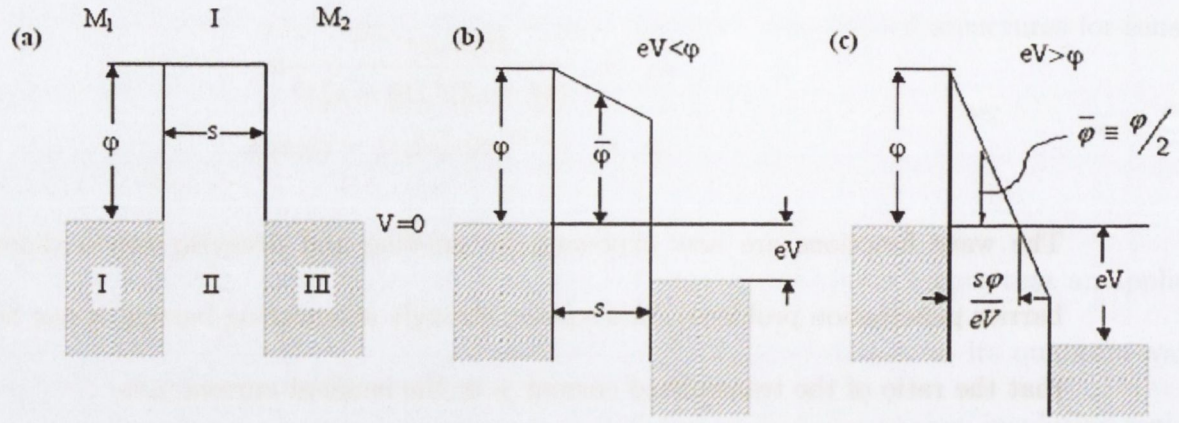

Figure 2.2 *Schematic of the energy diagram for a square metal-insulator-metal barrier. a) Before a voltage is applied, b) when the applied voltage is small compared with the barrier height and c) when the applied voltage is bigger that the barrier height (field-emission).*

A simple method to determine the thickness and height of an ideal barrier from the $j - V$ characteristic was described by Simmons et al. [21]. At low voltages, the expression for tunneling current across a metal-insulator-metal structure can be reduced to give

$$j = \beta \left(V + \gamma V^3 \right) \tag{25}$$

with

$$\beta = \frac{3}{2s} \left(\frac{e}{\hbar} \right)^2 (2m\varphi)^{1/2} \exp \left[- \left(\frac{4\pi s}{\hbar} \right) (2m\varphi)^{1/2} \right] \tag{26}$$

$$\gamma = \frac{\pi m}{3\varphi} \left(\frac{es}{\hbar} \right)^2, \tag{27}$$

where φ is the height and s is the thickness of the barrier, j is the tunneling current density, and V is the device voltage. The expressions for s and φ are obtained from (26) and (27). Thus,

$$s = 4.94 \gamma^{\frac{1}{4}} L^{\frac{1}{2}} \tag{28}$$

and

$$\varphi = \left(\frac{0.266}{\gamma^{\frac{1}{2}}} \right) L, \tag{29}$$

where

$$L = \log_{10}\left[\left(4.87 \times 10^{13}\right)/\beta\gamma^{\frac{1}{2}}\right]. \tag{30}$$

The value of s is given in angstroms and φ is in electron volts.

If the height of the energy barrier is smaller that the applied difference of potential (e.g. in a narrow air gap between conducting electrodes where the electric field overcomes the electron work function), the transport is in the field-emission regime (see figures 2.2 and 2.3). The current I can then be expressed in function of the applied voltage V in terms of the Fowler-Nordheim equation [22]:

$$I = \left(\frac{aV^2}{w^2}\right)\exp\left(\frac{-b\varphi^{\frac{3}{2}}s}{V}\right), \tag{31}$$

where a and b are material constants, φ is the barrier height (or work function) and s is the gap width. A plot of $\ln\left(\frac{I}{V^2}\right)$ vs. V^{-1} is shown below (Fig.2.3).

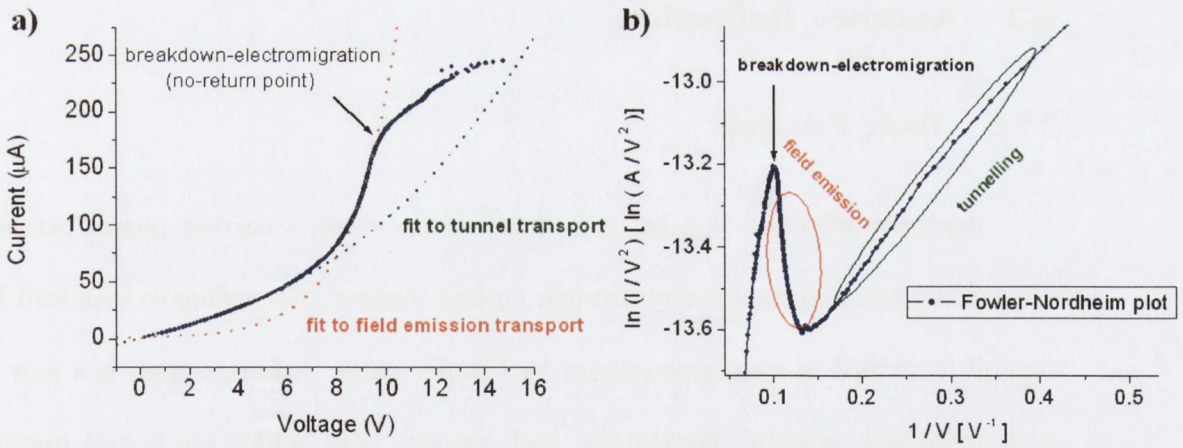

Figure 2.3 *a) I-V characteristic for a magnetite nanocontact fitted for tunnelling (Simmons) and field-emission regimes. At high voltages the sample is destroyed. b) Fowler-Nordheim plot of the same data. The negative slope is a sign of field-emission transport* [20],[22].

2.1.5 Grain Boundaries

Since there is no crystalline continuity across a point contact, there will be a grain boundary present. We thus need to examine transport across such a boundary. A precise

understanding of the nature of grain boundaries and their transport properties is still lacking, but several models have been proposed [24]-[29]. From one point of view, the grain boundary is considered to be insulating layer, of order a nanometer wide, and transport takes place through spin dependent tunneling. The opposing view is that a low resistance grain boundary acts as an interface between two ferromagnetic grains, and it is the scattering at this interface that leads to GMR type magnetoresistance [30].

Transport measurements of grain boundaries show non-linear IV curves that agree with the Glazman-Matveev model [31], suggesting resonant tunneling through grain boundaries via localized defect states. In this model, the grain boundary is modelled as an insulator, with one or more localized defects inside the barrier. When the Fermi level of the electrode coincides with the energies of these localized states, the conductivity is resonantly enhanced.

2.2 Andreev Reflection

2.2.1 Basic Principle

Andreev reflection is a process which occurs when a current passes between a superconducting and a normal metal through a point contact. According to standard BCS theory, current is carried in a superconductor by Cooper pairs. A Cooper pair is a pair of electrons with equal but opposite momentum, and opposite spin, which are bound together with an energy twice that of the superconducting gap Δ. For an electron to pass from a normal metal to a superconductor it must form a Cooper pair with another electron. This requires that the energy of the electron be greater than Δ. Thus at voltages lower than Δ/e there should be no conduction.

However there is a process where conduction can occur for lower voltages. This process

is known as Andreev reflection after its discoverer[32]. An electron passing through the interface can form a Cooper pair by pairing with an electron with an energy just below the Fermi energy of the normal metal. This leaves a hole in the normal metal, which is retro-reflected back from the interface. Thus for each electron passing through the interface with an energy below Δ, you get two conducting quasi-particles. We can thus say that the conductance at the normal/superconducting interface, G_{NS}, is double that for a normal/normal interface, G_{NN}, i.e.

$$\frac{G_{NS}}{G_{NN}} = 2. \tag{32}$$

The process requires ballistic transport to eliminate the effect of bulk scattering, and a point contact between the metal and the superconductor provides this. For this reason the process is often referred to as Point Contact Andreev Reflection (PCAR).

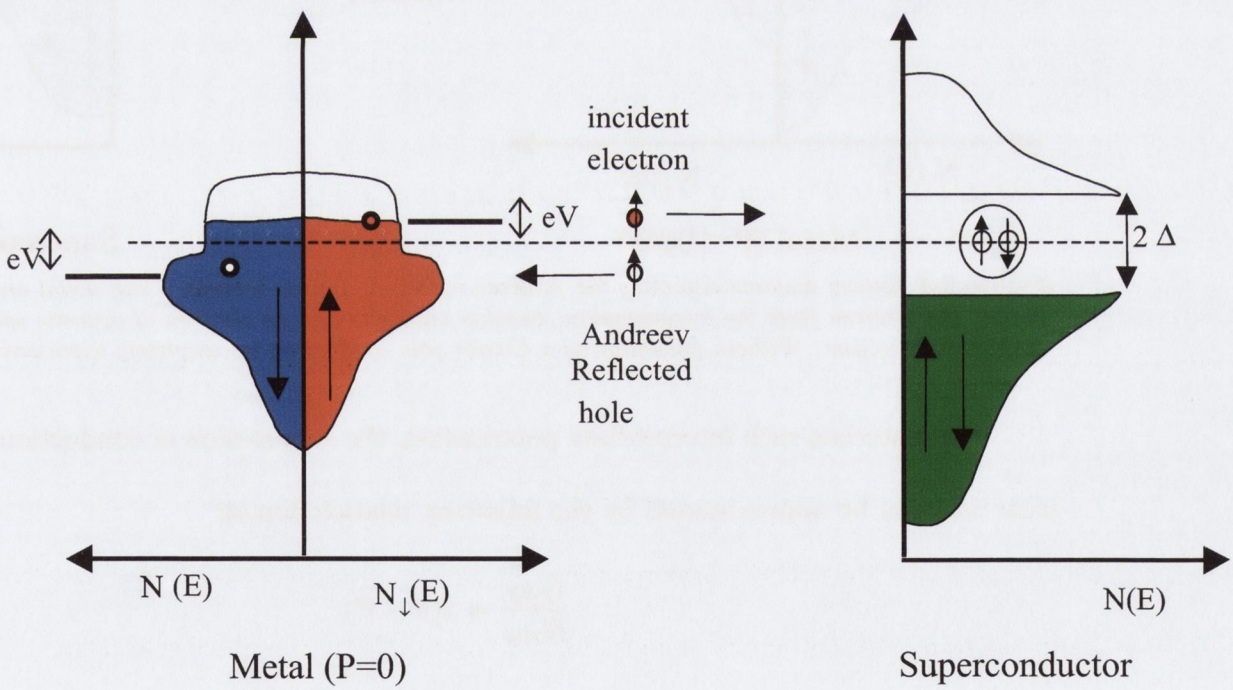

Figure 2.4 *Energy diagram depicting the Andreev reflection process between a normal metal and a superconductor. The pairing process leaves a hole in the normal metal which is reflected back from the interface, effectively doubling the current.*

If the normal metal is replaced by a half-metal the situation is different. Since one of

the spin channels is effectively empty around the Fermi energy, Cooper pairs are unable to form, since electrons of both spins are required to form a pair. In this case no conduction is allowed for voltages less than Δ/e, i.e.

$$\frac{G_{NS}}{G_{NN}} = 0. \tag{33}$$

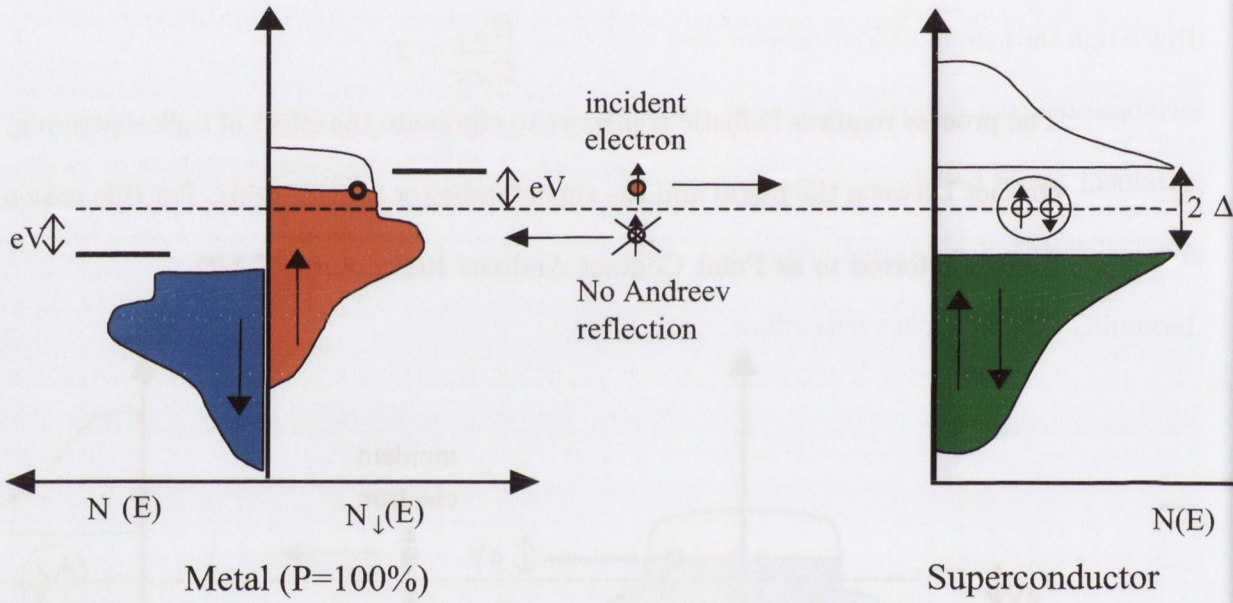

Figure 2.5 *Energy diagram depicting the Andreev reflection process between a half metal and a superconductor. An electron from the ferromagnetic metal is unable to find an electron of opposite spin with which to pair. Without formation of a Cooper pair conduction is completely supressed*

For materials with intermediate polarisation, the suppression of conduction is not complete and can be approximated by the following relationship[33]

$$\frac{G_{NS}}{G_{NN}} = 2(1 - P). \tag{34}$$

As we can see from above, we can use the Andreev Reflection process to measure the spin polarisation of a material. However the situation as described here is somewhat oversimplified: a temperature of 0 K is assumed, and it does not take into account scattering effects at the interface, caused by an insulating oxide barrier layer or impurities for example.

To take these factors into account a better model must be used. Such a model has been devised by Blonder, Tinkham, and Klapwijk [34].

2.2.2 BTK Theory

The BTK (Blonder-Tinkham-Klapwijk) model is used to describe the conductance vs. voltage curves obtained from the PCAR process. It assumes transport is ballistic through the point contact. The reflection and transmission coefficients for electrons at the interface are then determined by solving the Bogoliubov-de Gennes equation.

When a superconductor is at a temperature above 0 K, not all of the electrons form Cooper pairs. These unpaired electrons are known as quasi-particles, since they can be found in two base states: 'electron-like' , where the electron is above the average energy of the Cooper pairs, and 'hole-like', where the electron is below the average energy of the Cooper pairs. They can be described using the Bogoliubov-de Gennes equation

$$i\hbar\frac{\partial\Psi}{\partial t} = \begin{pmatrix} H & \Delta \\ \Delta & -H \end{pmatrix}\Psi \tag{35}$$

where H is described by

$$H = -\frac{\hbar^2}{2m}\frac{d^2}{dx^2} - E_F + V(X) \tag{36}$$

and Ψ is the wavefunction of the quasiparticle,

$$\Psi(x,t) = f(x,t) \mid e\rangle + g(x,t) \mid h\rangle, \tag{37}$$

where $f(x,t)$ and $g(x,t)$ give the probability of finding the quasi-particle in an electron-like state $\mid e\rangle$ and a hole-like state $\mid h\rangle$ respectively. The Bogoliubov-de Gennes equation tells us that, apart from the coupling $\Delta(x)$, the quasi-particle obeys the Schrödinger equation when it is in $\mid e\rangle$ and the time-reversed Schrödinger equation when it is in $\mid h\rangle$.

In BTK, the mismatch in transport properties at or near the contact interface is mod-

eled as elastic scattering, using a repulsive delta function energy barrier of height S, where $E(x) = S\delta(x)$. S thus has units J.m, and the scattering is described by a dimensionless and temperature independent barrier strength parameter $Z = \frac{Sk_F}{2E_F}$, where k_F is the Fermi wave number. One main reason for using a delta function shaped barrier is that it is numerically solvable - more realistic shapes for the barrier make the solution of the equations nigh impossible.

Solving the Bogoliubov-de Gennes equation for this scenario allows the reflection and transmission probabilities for the interface to be determined. The Andreev reflection probability, A, the normal reflection probability, B, the electron-like transmission probability, C and the hole-like transmission probability, D, are calculated for different particle energies. The following equations are obtained for the reflection coefficients:

$E < \Delta$	$E > \Delta$
$A = \dfrac{\Delta^2}{E^2 + (\Delta^2 - E^2)(1+2Z^2)^2}$	$A = \dfrac{\varepsilon^2 - 1}{[\varepsilon + (1+2Z^2)]^2}$
$B = 1 - A$	$B = \dfrac{4Z^2(1+Z^2)}{[\varepsilon + (1+2Z^2)]^2}$

(38)

where ε is given by

$$\varepsilon = \frac{E}{\sqrt{E^2 - \Delta^2}}.$$

The transmission coefficients can then be determined using

$$A + B + C + D = 1.$$

When A and B are known the transmission probability $(C + D)$ can be easily calculated, however here we focus on A and B to calculate the total Andreev current. In figure 2.6, the Andreev and normal reflection coefficients have been plotted against the particle energy for different Z values. As Z increases the probability of Andreev reflection reduces, and reflection

becomes more normal. For very high values of Z, representing a tunneling transport regime, Andreev reflection is completely suppressed for low energies. At sub-gap energies the incident electron cannot enter the superconductor as a quasiparticle, i.e. A + B = 1. At above gap energies, the Andreev Reflection process no longer occurs.

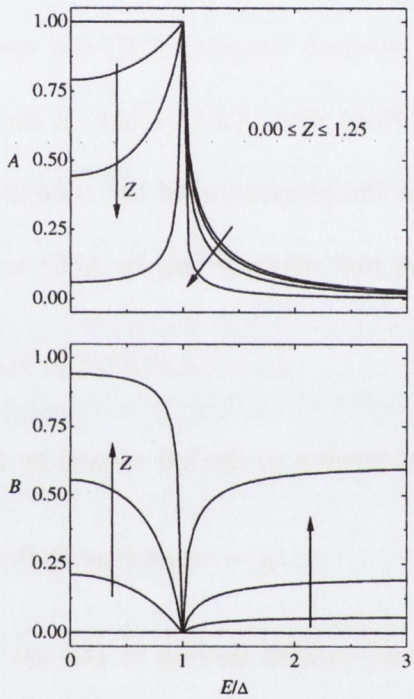

Figure 2.6 *Reflection coefficients A and B plotted as a function of particle energy for different values of Z. As Z increases the probability of Andreev reflection drops.*

At above-gap energies, the transmission $C + D$ equals $1 - (A + B)$. To find the transmission of the N/N interface we let $\Delta = 0$ or $\varepsilon = 1$. In this limit, evaluation of $1 - (A + B)$ gives the transmission = $1/(1+Z^2)$, which is the standard transmission for a δ-function barrier.

The known probabilities A and B are used to calculate the current at a given bias voltage. For simplicity's sake the current is calculated in the normal metal using the model of an electron incident from the normal side. In the normal metal there are currents flowing

to the right and to the left. The current flowing to the right consisting of the incident electrons with an energy in $[E, E + dE]$ is given by

$$I = eA_c v(E)\rho(E)f(E)dE, \tag{39}$$

where e is the charge of the electron, A_c the cross sectional area of the normal/superconducting interface, $v(E)$ the electron velocity, $\rho(E)$ the density of states and $f(E)$ the Fermi distribution function. Note that $\rho(E)f(E)dE$ is the density of electrons with an energy in $[E, E + dE]$. To find the proportion of the current which is given by Andreev reflection of incident electrons, we just multiply (39) by A(E) to get

$$I_A = eA_c v(E)\rho(E)A(E)f(E)dE. \tag{40}$$

Similarly, the current flowing to the left caused by normally reflected electrons is given by

$$I_B = eA_c v(E)\rho(E)B(E)f(E)dE. \tag{41}$$

There is a second current flowing to the left originating from particles incident from the superconducting side. This current can be written as

$$I_X = eA_c v(E)\rho(E)X(E)f(E)dE. \tag{42}$$

In the absence of an externally applied bias voltage, the total current is zero, implying that $X = 1 + A - B$. If we raise the potential of the normal side with respect to the superconducting side by V, the distribution of the incoming electrons from the normal side becomes $f(E - eV)$, while the particles incident from the superconducting side still have the distribution $f(E)$. Replacing accordingly, and summing (40), (41) and (42), we get

$$I(V) = eA_c \int v(E)\rho(E)[1 + A(E) - B(E)][f(E - V) - f(E)]dE. \tag{43}$$

The function $f(E-eV)-f(E)$ is nonzero only in a region of size eV in the vicinity of the E_F. Since $eV \approx \Delta << E_F$, the velocity and the density of states of the normal metal can be taken as constants, giving

$$I(V) = eA_c v\rho \int [1 + A(E) - B(E)][f(E-V) - f(E)]dE, \tag{44}$$

where now v and ρ are the electron velocity and density of states of the normal metal at E_F. The conductance $G_{NS} = dI/dV$ then becomes

$$G_{NS} = -e^2 A_c v\rho \int [1 + A(E) - B(E)]f'(E-V)dE. \tag{45}$$

where f' is the derivative of the Fermi distribution function. The function $-f'(E)$ is zero everywhere except near $E = 0$, where it has a pulse-shape similar to a delta-function with a width proportional to $k_B T$. When both sides of the interface are normal metal ($\Delta = 0$), equation (45) reduces to

$$G_{NN} = \frac{e^2 A_c v\rho}{1+Z^2}. \tag{46}$$

The conductance in the superconducting state normalized by the conductance in the normal state becomes

$$\frac{G_{NS}}{G_{NN}} = -(1+Z^2) \int ([1 + A(E) - B(E)]f'(E-V)dE, \tag{47}$$

which is the main result of the BTK theory. In figure 2.7, the normalised conductance values have been plotted as a function of bias voltage for different barriers at two different temperatures. As Z reaches very high values we essentially have tunneling across the interface, and application of a magnetic field must be used to determine spin polarisation - the famous Tedrow-Meservey experiment [35]. For higher temperatures we see a smearing of the conductance peaks at Δ. As expected, higher barrier values impede the Andreev reflection process

and the conductance drops for voltage values below Δ/e.

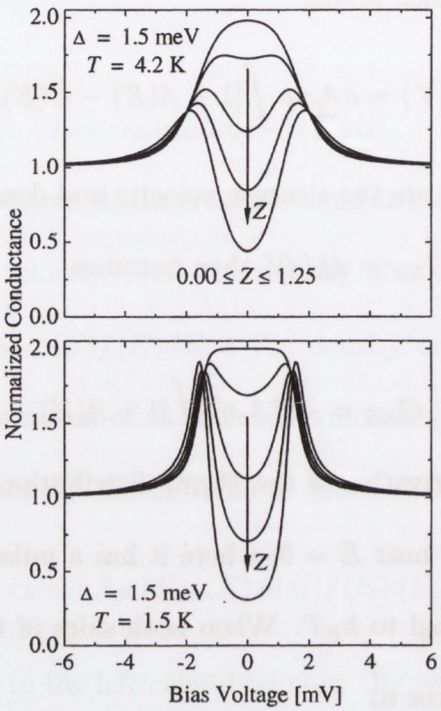

Figure 2.7 *Normalised conductance as a function of applied voltage for an Andreev point contact. Curves are shown for different values of Z at two different temperatures.*

2.2.3 Modifications of BTK theory

The BTK theory, while being quite complex, still has many limitations. The exact interpretation of the Z-parameter is somewhat unclear. The superconducting proximity effect, where the superconducting wavefunction decays a small distance into the normal metal, has been ignored. Perhaps most importantly in the scope of this thesis, the BTK theory does not take spin-polarisation into account. In this section I will review the attempts that have been made to modify these limitations, and give an overview on recent developments on the theory of Andreev reflection.

The first theoretical account dealing with spin polarisation in PCAR was given by

deJong and Beenakker in 1995 [33]. Experimental results were then obtained by Soulen [36] on certain spin polarised materials such as Fe, LSMO and CrO_2. In this paper the authors created a model to fit their results and extract a value for the spin polarisation at the normal-superconducting interface. To do this they separated the current into two channels - one polarised, I_{pol} and one non-polarised, I_{unpol}, so that

$$I = I_{pol} + I_{unpol}$$

The unpolarized current, I_{unpol}, is calculated using the conventional BTK theory. The remaining current, I_{pol}, is also calculated using BTK, however here the probability of Andreev reflection, $A(E)$, is set to zero, and only normal reflection and transmission can take place. The spin polarisation, P, can be extracted from the dI/dV curves by noting that

$$\frac{d}{dV}I(V,T,P,Z) = (1-P)\frac{d}{dV}I_{unpol}(V,T,Z) + P\frac{d}{dV}I_{pol}(V,T,Z)$$

If we take the limit of minimal interfacial scattering (i.e. $Z \approx 0$), then for low voltages and temperatures we get

$$\frac{d}{dV}I_{unpol}(V,T,Z) = 2G_{NN}$$

and

$$\frac{d}{dV}I_{pol}(V,T,Z) = 0$$

to give

$$\frac{G_{NS}}{G_{NN}} = 2(1-P),$$

a result which was predicted in the paper by de Jong and Beenakker [33]. One should be aware that this model assumes that the ratio between normally reflected and transmitted probabilities $B/(C+D)$ is the same for the polarised and unpolarised channels. However this assumption has been shown to be valid elsewhere [42].

Another model is presented by Strijkers et al. [37]. This model takes into account the proximity effect as well as spin polarisation. The proximity effect is when Cooper pairs from a superconducting metal in close proximity to a normal metal diffuse into the metal, causing a thin layer of the normal metal to become superconducting [38]. This superconducting proximity layer has a lower transition temperature and a lower Δ than the bulk. The Andreev reflection process, occurring at the metal/proximity-layer interface, is therefore limited to bias voltages smaller than the superconducting gap value of the proximity layer. However, quasiparticles can only enter the superconductor for voltages higher than the bulk gap of the superconductor.

The authors account for the proximity effect by using two values for the superconducting energy gap, one for the Andreev reflection process (Δ_1), and one for the quasiparticle transport (Δ_2). The reflection probabilities are then calculated, and from this the conductance vs. voltage curves can be calculated. The proximity layer is observed as dips in the conductance at voltages between Δ_1/e and Δ_2/e (see fig 2.8). This model is the one used in this thesis to fit the data obtained from PCAR measurements. A good review of the proximity effect is given in [39] and [40], and [41] studies the effect in ferromagnet/superconductor structures.

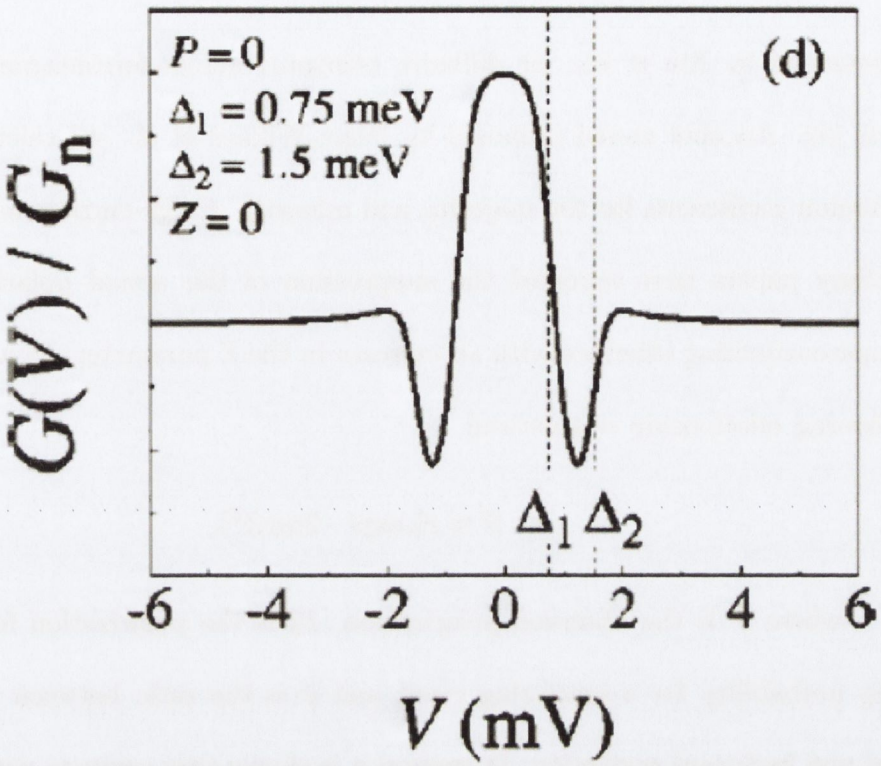

Figure 2.8 *Conductance curve from Strijkers et al.*[37] *produced by a model which takes into account the superconducting proximity effect.*

A paper by Mazin et al. [42] proposed a different approach in the treatment of the polarised conduction channel at the ferromagnet/superconductor interface. Instead of setting the Andreev reflection probability to zero, the model describes the Andreev-reflected hole as a spatially decaying evanescent wave with finite probability but carrying no net current. The author is able to use this model to calculate the conductance vs. voltage curves in the diffusive transport regime. They show that the value of spin polarisation obtained is independent of the model used; the only parameter affected is the strength of the Z parameter. This means that a correct value for P can be obtained using a ballistic model (such as Strijkers) to fit data, even if the data is obtained from a diffusive contact. Other publications have since backed up this claim[43],[44], however it is also claimed elsewhere that different polarisation values can be obtained depending on which model is used [45]. A similar model

was developed by Xia et al. for diffusive transport across ferromagnetic/superconductor contacts [46]. Another model proposed by Pérez-Willard et al. [47] calculates two separate transmission coefficients for the majority and minority charge carriers in the ferromagnet.

Many papers have reported the suppression of the actual polarisation of the normal/superconducting interface with an increase in the Z parameter. In a paper by Kant[48], the following relationship was derived

$$P \approx P_0 \exp(-2\alpha\psi Z^2),$$

where P is the observed polarization, P_0 is the polarization for $Z = 0$, α is the spin-flip probability for a scattering event and ψ is the ratio between the probability for forward and backward scattering. In general it is shown that contacts with a lower value for Z will give higher spin polarization values.

More recently attempts have been made to use PCAR to measure spin polarisation in magnetic semiconductors. In a paper by Panguluri et al.[49], PCAR measurements were carried out on $In_{1-x}Mn_xSb$, a magnetic semiconductor. Measurements were then carried out on its nonmagnetic analog, $In_{1-y}Be_ySb$. Comparisons were then made between the results obtained from the two materials, and a spin polarisation value of $53 \pm 2\%$ was estimated for $In_{1-x}Mn_xSb$. Attempts have also been made to measure Andreev reflection in other magnetic semiconductor systems [50], [51]. However for a truly accurate value to be obtained from such results, a model has to be produced for PCAR across a semiconductor/superconductor interface.

References

[1] Y. V. Sharvin, Sov. Phys. JETP **21** (1965).

[2] C. Shu, C. Z. Li, H. X. He, A. Bogozi, J. S. Bunch, and N. J. Tao, Phys. Rev. Lett. **84,** 5197 (2002).

[3] T. Ono, Y. Ooka, H. Miyajima and Y. Otani, Appl. Phys. Lett. **75** 1622 (1999).

[4] B. J. van Wees, H. van Houten, C. W. J. Beenakker, J. G. Williamson, L. P. Kouwenhoven, D. van der Marel, and C. T. Foxon, Phys. Rev. Lett. **60**, 848 (1988).

[5] J. I. Pascual, J. Mendez, J. Gomez-Herrero, A. M. Baro, N. García, and V. T. Binh, Phys. Rev. Lett. **71**, 1852 (1993).

[6] J. I. Pascual, J. Mendez, J. Gomez-Herrero, A. M. Baro, N. García, U. Landman, W. D. Luedtke, E. N. Bogachek, and H. P. Cheng, Science **267**, 1793 (1995).

[7] L. Olesen, E. Lægsgaard, I. Stensgaard, F. Besenbacher, J. Schiøtz, P. Stoltze, K.W. Jacobson, and J.K. Nørskov, Phys. Rev. Lett. **72**, 2251 (1994).

[8] N. Agraït, G. Rubio, and S. Vieira, Phys. Rev. Lett. **74**, 3995 (1995).

[9] C. J. Muller, J. M. van Ruitenbeek, and L. J. de Jongh, Phys. Rev. Lett. **69**, 140 (1992).

[10] M. Viret, S. Berger, M. Gabureac, F. Ott, D. Olligs, I. Petej, JF Gregg, C. Fermon, G. Francinet, and G. Le Goff, Phys. Rev. B **66**, 220401 (2002).

[11] P. Weiss, J. de Phys. Rad. **6**, 661 (1907).

[12] F. Bloch, Z. Phys. **74**, 295 (1932); L. Landau and E. Lifshitz, Phys. Z. Sowjetunion **8**, 153 (1935).

[13] M. Viret, D. Vignoles, D. Cole,J. M. D. Coey, W. Allen, D. S. Daniel, and J. F. Gregg,

Phys. Rev. B **53**, 8464 (1996)

[14] J. F. Gregg, W. Allen, K. Ounadjela, M. Viret, M. Hehn, S. M. Thompson, and J. M. D. Coey, Phys. Rev. Lett. **77**, 1580 (1996).

[15] P.M. Levy and S. Zhang, Phys. Rev. Lett. **79**, 5110 (1997).

[16] P. Bruno, Phys. Rev. Lett. **83**, 2425 (1999).

[17] Y. Labaye, L. Berger, and J. M. D. Coey, J. App. Phys. **91**, 5341 (2002).

[18] O. Céspedes, G. Jan, M. Viret, M. Bari, and J. M. D. Coey, J. Appl. Phys. **93**, 8433 (2003).

[19] E. O. Kane in Tunneling Phenomena in Solids, E. Burstein and S. Lundqvist eds., Plenum, (1973).

[20] I. Giaever in Tunneling Phenomena in Solids, E. Burstein and S. Lundqvist eds., Plenum, (1973).

[21] J. G. Simmons and G. J. Unterkofler, J. Appl. Phys. **34** 1828 (1963).

[22] R. H. Fowler and L. Nordheim, Proc. Roy Soc A **119**, 173 (1928).

[23] B. Raquet in "Spin Electronics", M. Ziese and M.J. Thornton eds., Springer (2001).

[24] J. E. Evetts, M. G. Blamire, N. D. Mathur, S. P. Isaac, B.S. Teo, L. F. Cohen and J. L. MacManus-Driscoll, Phil. Trans. R. Soc. Lond. A **356**, 1593 (1998).

[25] J. M. D. Coey, A. E. Berkowitz, L. Balcells, F. F. Putris, and A. Barry, Phys. Rev. Lett. **80**, 3815 (1998).

[26] F. Guinea, *Phys. Rev. B* **58**, 9212 (1998).

[27] M. Ziese, C. Srinitiwarawong, and C. Shearwood, J. Phys. Cond. Mat. **10**, L659 (1998).

[28] S. Lee, H. Y. Hwang, B. I. Shraiman, W. D. Ratcliff, S.W. Cheong, Phys. Rev. Lett.

82, 4508 (1999).

[29] J. Klein, C. Höfener, S. Uhlenbruck, L. Alff, B. Büchner, and R. Gross, Europhys. Lett. **47** (3), 371 (1999).

[30] T. Valet, and A. Fert, Phys. Rev. B **48**, 7099 (1993).

[31] L.I. Glazman, and K.A. Matveev, Sov. Phys. JETP **67**, 1276 (1988).

[32] A. F. Andreev, Zh. Eksp. Teor. Fiz. **46**, 1823 (1964) [Sov. Phys. JETP **19**, 1228 (1964)].

[33] M. J. M. de Jong and C. W. J. Beenakker, Phys. Rev. Lett. **74**, 1657 (1995).

[34] G. E. Blonder, M. Tinkham, and T. M. Klapwijk, Phys. Rev. B **25**, 4515 (1982).

[35] R. Meservey and P. M. Tedrow, Phys. Rep. **238**, 173 (1994).

[36] R. J. Soulen, J. M. Byers, M. S. Osofsky, B. Nadgorny, T. Ambrose, S. F. Cheng, P. R. Broussard, C. T. Tanaka, J. Nowak, J. S. Moodera, A. Barry, and J. M. D. Coey, Science **282**, 85 (1998).

[37] G. J. Strijkers, Y. Ji, F. Y. Yang, C. L. Chien, and J. M. Byers, Phys. Rev. B **63**, 104510 (2001).

[38] M. Tinkham, Introduction to Superconductivity, McGraw-Hill Inc., New York, (1996).

[39] B. Pannetier and H. Courtois, J. Low Temp. Phys. **118**, 599 (2000).

[40] T. M. Klapwijk, J. Supercond.:Incorp. Novel Magn. **17**, 593 (2004).

[41] Y.A. Izyumov, Y.N. Proshin, M.G. Khusainov, Physics-Uspekhi **45,** 109 (2002).

[42] I. I. Mazin, A. A. Golubov, and B. Nadgorny, J. Appl. Phys. **89**, 7576 (2001).

[43] G. T. Woods, R. J. Soulen, Jr., I. I. Mazin, B Nadgorny, M. S. Osofsky, J. Sanders, H. Srikanth, and W. H. Egelhoff, Phys. Rev. B **70**, 54416 (2004).

[44] Y. Ji, G. J. Strijkers, F. Y. Yang, and C. L. Chien, Phys. Rev. Lett. **64**, 224425 (2001).

[45] N. Auth, G. Jakob, T. Block and C. Felser, Phys. Rev. B **68**, 024403 (2003).

[46] K. Xia, P. J. Kelly, G. E. W. Bauer, I. Turek, Phys. Rev. Lett. **89,** 166603 (2002).

[47] F. Pérez-Willard, J. C. Cuevas, C. Sürgers, P. Pfundstein, J. Kopu, M. Eschrig, and H. v. Löhneysen, Phys. Rev. B **69**, 140502 (2004).

[48] C. H. Kant, O. Kurnosikov, A. T. Filip, P. LeClair, H. J. M. Swagten, and W. J. M. de Jonge, Phys. Rev. B **66**, 212403 (2002).

[49] R.P. Panguluri, B. Nadgorny, T. Wojtowicz, W.L. Lim, X.Liu, J.K. Furdyna, Appl. Phys. Lett. **84**, 4947 (2004).

[50] J. G. Braden, J. S. Parker, P. Xiong, S. Chun, and N. Samarth, Phys. Rev. Lett. **91**, 056602 (2003).

[51] R. P. Panguluri, K. C. Ku, T. Wojtowicz, X. Liu, J. K. Furdyna, Y. B. Lyanda-Geller, N. Samarth, and B. Nadgorny, Phys. Rev. B **72**, 054510 (2005).

Chapter 3

Experimental Procedure

Many of the materials examined within the scope of this thesis had to be fabricated in our lab. As a result it was important to carry out characterisation measurements, such as XRD and SEM imaging, to verify the purity and quality of our samples. In this section, the fabrication and characterisation techniques utilised will be outlined. For the section on Andreev reflection it was required to make device structures using our subject materials. The nanofabrication techniques utilised to create these devices will also be discussed.

3.1 Fabrication techniques

3.1.1 Thermal evaporation

Thermal evaporation is a technique used to deposit a thin film of a metal onto a substrate. The desired metal is evaporated in a vacuum environment, and the atomic cloud formed coats all the surfaces in the line of sight between the substrate and the metal source. This method can produce shiny, smooth films up to 0.5 μm. The coating, however, is fragile and peels off easily, thus rendering the technique unsuitable for high resolution lithography applications (see fig. 3.1). It is also unsuitable for metals with a high melting point. However, it is a very useful method for creating metallic contacts and also for deposition of thicker films. Evaporation was used in this thesis for the fabrication of the Andreev Reflection nano-indentation devices, where a film of lead is deposited onto a soft-baked PMMA layer. The evaporator is an Edwards Auto 306 evaporator, and the operating vacuum in the evaporation chamber is typically 5×10^{-7} mbar.

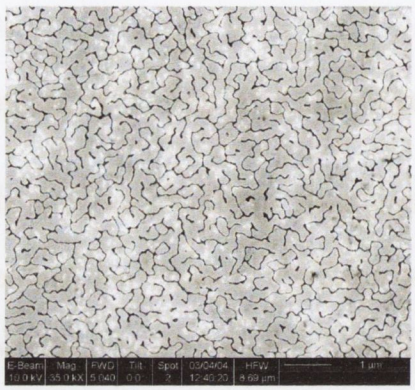

Figure 3.1 *Evaporated gold film 60 nm thick on top of a Fe_3O_4 sputtered film. Thermal evaporation produces good-conductivity films, but the topography does not have the same quality as sputtered or PLD-deposited films.*

3.1.2 Sputtering

Another technique used to make metallic films is sputtering. Sputtering is a vacuum process performed by applying a high voltage across a low-pressure gas (usually argon) to create a plasma. The ions in the plasma are accelerated towards a target, consisting of the desired deposition metal, by using a DC or RF voltage bias. Energized plasma ions strike the target and, under good vacuum, the struck target atoms will be ejected with enough energy to travel and form a bond with the substrate and subsequently form of a film of the extracted material on the substrate. To deposit on metallic substrates a DC bias is usually employed, whereas when the substrate is non-conductive, e.g. a polymer, radio-frequency (RF) sputtering is generally used. The resulting crystallographic phase of the film depends on the substrate type, temperature and the surrounding atmosphere. In the case of oxide films, e.g. magnetite, a partial pressure of oxygen is added to the argon. Films used in this study were grown either using a Leybold Z550-S DC-magnetron sputtering machine or a Shamrock DC-magnetron sputtering system. Substrates were cleaned using acetone and ethanol before deposition.

3.2 Characterisation Techniques

3.2.1 XRD

XRD (X-ray diffraction) analysis was used to determine the structural characterization of our samples. This technique probes the crystal lattice with copper K_α radiation (wavelength $\lambda = 1.5418$ Å). The X-rays are specularly reflected from the successive parallel planes of atoms in the crystal (see fig 3.2). At certain angles the diffracted beams interfere constructively, leading to a peaks in the detected intensity.

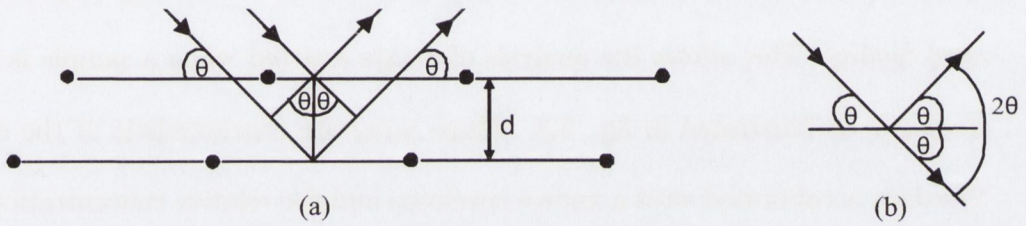

Figure 3.2 *(a) A Bragg reflection from a particular set of lattice planes separated by a distance d and (b) θ is just half of the total angle by which the incident beam is deflected*

The position and intensity of these peaks is unique to each crystalline material. X-ray diffraction is based on Bragg's condition:

$$n\lambda = 2d\sin(\theta), \tag{1}$$

stating that a diffraction pattern is observed only when the path difference between the reflected waves (the product of twice the lattice spacing d and the sine of the diffraction angle θ) equals an integral number of X-ray wavelength λ. Spectra were recorded on a Siemens D500 diffractometer. For polycrystalline samples, powders were made by crushing a portion of the sample in a mortar and pestle. For a single crystal sample, XRD was performed on a polished edge of the crystal.

3.2.2 Electron Microscopy

Sample morphology was studied using a Hitachi S - 3500N scanning electron microscope (SEM) in high vacuum mode with sub-micron resolution, in the Centre for Microscopy and Analysis (CMA), Trinity College. SEM involves the detection of secondary or back-scattered electrons following the bombardment of the sample with a beam of highly focused electrons. The electrons, which possess a much greater energy than optical photons, give rise to a much higher magnification and image resolution than an optical microscope.

This unit is also equipped with a PGT-Imix EDAX (energy dispersive analysis of X-rays) facility. This allows the analysis of x-rays emitted when a sample is bombarded with electrons, as illustrated in fig. 3.3. These x-ray are characteristic of the elements present. The data is calibrated with a known specimen and the relative concentration of the elements may then be concluded. The lighter elements such as O, H, N and C are difficult to detect due to the low energy of their characteristic x-rays. This technique is used to determine the chemical composition of compounds and to identify the impurities present. It is also used to see phase separation in metallic alloys.

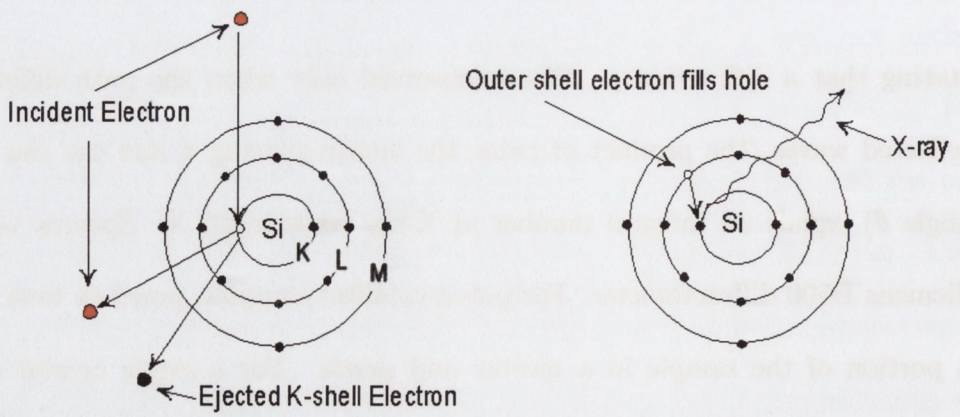

Figure 3.3 *The incident electron from the SEM column causes an inner shell (K) electron to be emitted from the silicon atom, which is replaced by an electron from an outer shell (L), also producing an x-ray.*

3.2.3 Atomic Force Microscopy

The atomic force microscope (AFM),was invented in 1986 by Binnig, Quate and Gerber [1]. The AFM utilises a sharp probe moving over the surface of a sample in a raster scan to reproduce the topography of the sample surface, thanks to a tip on the end of a cantilever which bends in response to the force between the tip and the sample.

The first AFM used a scanning tunnelling microscope at the end of the cantilever to detect the bending of the lever, but now most AFMs, including the Nanoscope Multimode III (Veeco) used in this work, employ an optical lever technique. In this optical update a laser is reflected at the edge of the cantilever and into a photodetector. As the cantilever flexes, the light from the laser is reflected onto different regions of the photodetector.

Contact mode is the easiest method of operation of the AFM. As the name suggests, the tip and sample remain in close contact as the scanning proceeds. By "close contact" we mean in the repulsive regime of the inter-molecular force curve, i.e., they are touching. The AFM measures the forces (at the atomic level) between the sharp probing tip and the sample surface by measuring the changes in the bending of the cantilever through the variation of the reflected laser spot position z in the photodetector. Images are taken by scanning the sample and measuring the deflection of the cantilever as a function of lateral position. As the scanner gently traces the tip across the sample, the contact force causes the cantilever to bend, and the electronics react maintaining a constant z using a positioning device in what is called the z-feedback loop.

The movement of the tip or sample is performed by an extremely precise positioning device made from piezoelectric ceramics in the form of a tube scanner. The scanner is capable of sub-angstrom resolution in x-, y- and z-directions (z-perpendicular to sample), but the

environmental conditions, such as vibrations, temperature and humidity fluctuations, lateral forces, sample roughness and adhesion of the tip to the gas-water layer on top of the sample, limit the resolution to approximately 2-5 nm laterally and to 0.1 nm for the z- direction for samples without sudden changes of topography (steps, as could be the case for focussed ion beam milled samples, see section 2.2.4) and 4-20 nm in lateral plus 1 nm in height for the more topographically challenged samples.

Another AFM technique is the tapping mode technique. Tapping mode is a patented technique by Veeco Instruments that maps the topography by lightly tapping the surface with an oscillating probe tip. The cantilever's oscillation amplitude changes with sample surface topography, and the topography image is obtained by monitoring these changes and closing the z feedback loop to minimize them. When operated in air or other gases, the cantilever is oscillated at its resonant frequency (typically 50 to 300 kHz) and positioned above the surface at a height h_T (amplitude setpoint) so that it only taps the surface for a very small fraction of its oscillation period. When imaging poorly immobilised (e.g., nanotubes or nanobeads spread on a substrate) or soft samples (like organic cells), tapping mode is generally a far better choice than contact mode for imaging.

In general, tapping mode is also much more effective for imaging larger scan sizes that may include large variations in sample topography. Tapping mode can be performed in gases, liquids, and some vacuum environments. A major advantage of the tapping mode is related to limitations that usually arise due to the thin layer of liquid that forms on sample surfaces in an ambient imaging environment, i.e. in air or some other gas. The amplitude of the cantilever oscillation in tapping mode is typically on the order of a few 10's of nanometers, which ensures that the tip does not get stuck in this liquid layer.

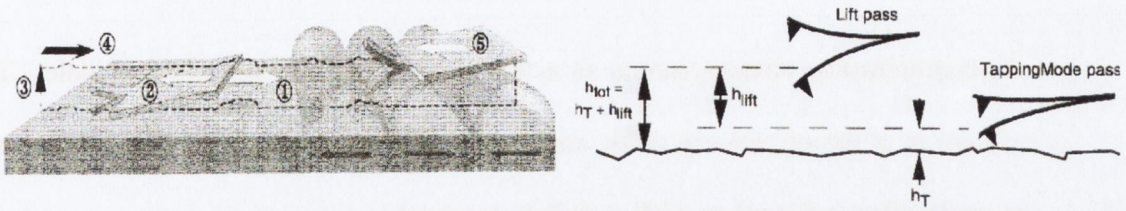

Figure 3.4 *Schematic of the tapping and lift modes. Left: 1 & 2 the cantilever traces the surface topography on first trace and retrace, 3 the cantilever ascends to the lift scan height, 4 and 5 the lifted cantilever profiles topography while responding to magnetic influences on second trace and retrace.*

Alternative methods of obtaining image contrast are also possible with tapping mode (fig. 3.4). In constant force mode, the feedback loop adjusts so that the amplitude of the cantilever oscillation remains (nearly) constant. An image can be formed from this amplitude signal, as there will be small variations in the oscillation amplitude, frequency or phase between the oscillations of the cantilever driving piezo and the detected oscillations in the photodetector (due to the control electronics not responding instantaneously to changes on the specimen surface).

3.2.4 VSM

To carry out room temperature magnetisation measurements, a VSM (vibrating sample magnetometer) was used. The VSM uses a variable field created by two concentric Halbach cylinders. The magnitude of the field was changed by rotating the cylinders so that the vector addition of their magnetisation added to the desired applied field, up to a maximum of 1.1 T. The sample was vibrated at 29.4 Hz along the bore of the cylinders (H $\perp$ bore). The displacement of the sample gives rise to a change in magnetic flux Φ over time. This induces a voltage V in the coils:

$$V = C\frac{\partial \Phi}{\partial t}, \tag{2}$$

where C is a constant. Integrating the voltage over time gives the total change in flux which is proportional to the magnetization. A hysteresis curve is obtained when doing a series

of magnetization measurements as a function of the applied external field. This induces a voltage in a set of pick-up coils, also inside the bore, which can be converted to magnetic moment after calibration with a nickel standard.

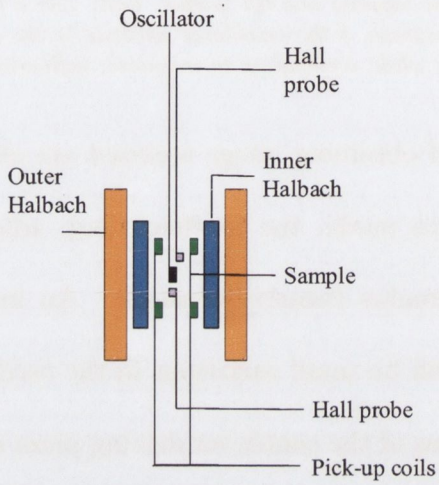

Figure 3.5 *Schematic diagram of a VSM (vibrating sample magnetometer).*

3.2.5 SQUID

For carrying out magnetisation measurements at lower temperatures, a Quantum Design Magnetic Property Measurement System (MPMS) sample magnetometer was used. A superconducting quantum interference device (SQUID) detection system is integrated with a temperature control unit, a high field superconducting magnet and a computer operating system. Liquid helium is necessary for refrigeration of the superconducting components as well as for low temperature measurements. Measurements can be made between 1.7 and 300 K in a field of up to 5 T, with a sensitivity of 10^{-11} Am^2.

Measurements used the Reciprocating Sample Option (RSO) where the sample is vibrated parallel to the field direction. Bulk samples were crushed into a powder using a mortar and pestle. These powders were weighed, then placed in gel caps and inserted into a straw, which could then be placed into the system for measurement.

3.2.6 Magnetostriction

Magnetostriction is when ferromagnetic materials undergo a change to their physical dimensions when subjected to a magnetic field. Magnetostriction measurements were carried out using a pair of strain gauges in a Wheatstone bridge (see fig. 3.6) with two precision wire wound resistors, mounted in a die-cast box to shield from noise. One of the gauges is fixed to the sample using cyanoacrylate (i.e. superglue), the other is used as a dummy. A change in the length of the sample (ΔL) corresponds to a change in the resistance of the gauge (ΔR) according to the following formula

$$\frac{\Delta R}{R} = K\frac{\Delta L}{L}$$

where K is a constant called the gauge factor and is 2.1 for the 5 mm aluminium gauges used here.

Since measured magnetostriction is typically of the order of microstrains, and one microstrain corresponds to a change in length of .0001%, a very sensitive detection device is required. The output of the bridge is measured using a circuit based around a variable low noise, low drift linear dc amplifier, with 1000 gain.

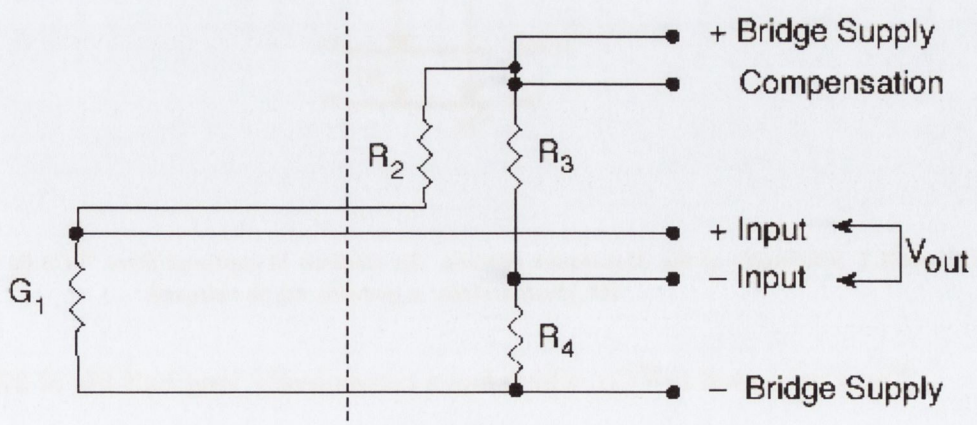

Figure 3.6 *Schematic of bridge used for magnetostriction measurements. G1 is the active gauge, R2 is the*

dummy gauge and R3 and R4 are precision wire wound resistors.

3.2.7 Mossbauer Spectroscopy

The presence of Fe and its properties were investigated in some samples using Mössbauer spectroscopy. The Mössbauer effect utilizes the fact that ^{57}Fe nuclei in a lattice can absorb gamma rays recoil-free. This is due to the fact that the atom is bound in the crystal lattice, and the lattice vibrations are quantised, effectively opening the possibility of zero-phonon processes with no recoil motion of the absorbing atom. The emitted gamma ray's energy is not affected. Any Fe nuclei can thus resonantly absorb the recoil-free radiation. In practice, the radiation is Doppler-shifted through a range of energies by movement of the source relative to the sample. The sample must be thin enough so as not to absorb the radiation completely in a non-resonant fashion and to discard the chance of re-emitted radiation to be re-absorbed.

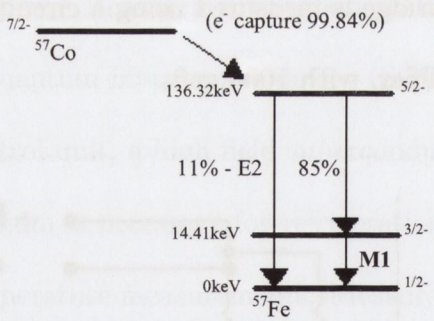

Figure 3.7 *Schematic of the Mossbauer process. An electron is captured from ^{57}Co by ^{57}Fe. As it drops to the ground state, a gamma ray is released.*

The source used is ^{57}Co, which has a conveniently long half-life of 270 days. The ^{57}Fe 14.41-keV level is efficiently populated by electron capture of ^{57}Co and subsequent γ-ray emission. The 14.41-keV state transition to ground state produces a γ-ray (fig. 3.7) and the

transition type is primarily M1 (with a tiny fraction of E2). The lifetime of this state give a Heisenberg width Γ_H of 0.192 mm s^{-1}.

3.3 Nanofabrication techniques

3.3.1 UV lithography

Lithography is a process used to transfer a pattern from a mask to the surface of a material. In UV-lithography this transfer is made by exposing to UV light a Cr-glass mask (which acts as a shield to the radiation), which is in contact with a photoresistive material whose properties vary when exposed to UV radiation (fig. 3.8). For the devices in this thesis we used a negative photoresist, which means that it becomes insoluble in certain solvents (in this case dilute acetone) after being exposed to UV light. After the exposure to UV light the exposed areas are removed in the solvent and we are left with the original pattern defined by the mask.

Our mask aligner is a Karl Suss MJB 3, which utilises a lamp with a UV wavelength λ of 250 nm which defines the resolution of the masks used. This method therefore cannot then produce real nano-scale devices, but is instead used as an initial step for the patterning of contact masks and μm tracks that can be reduced in size using other processes.

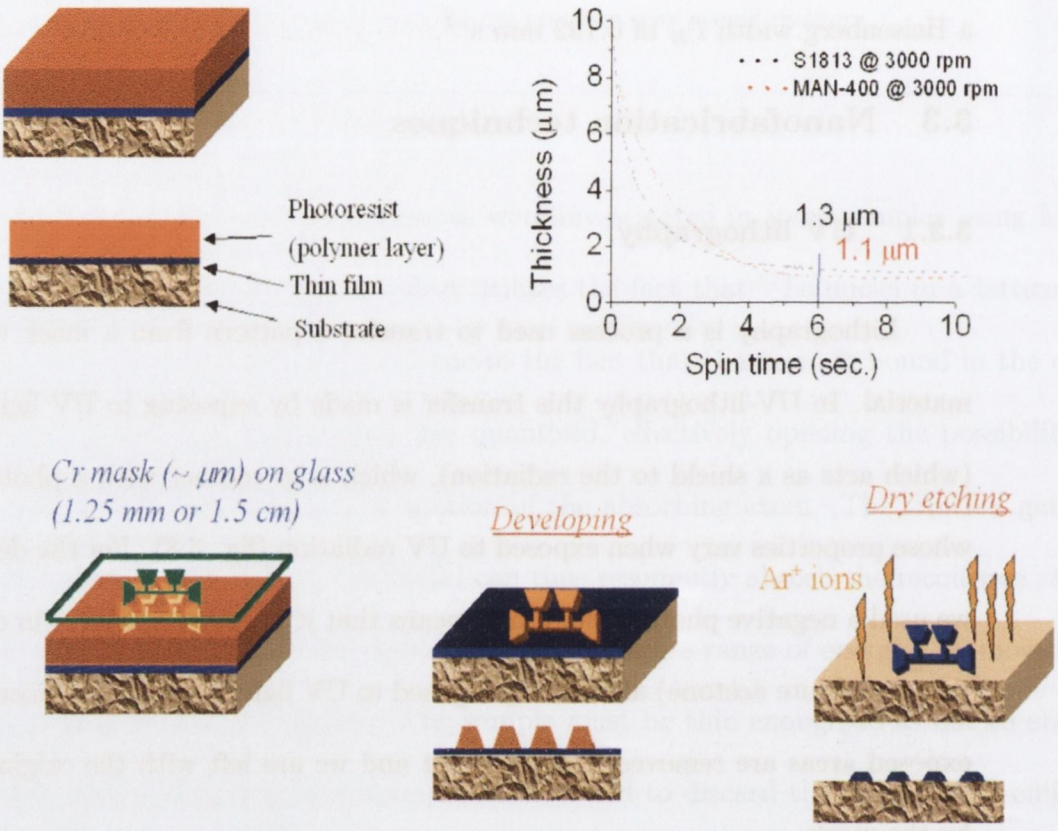

Figure 3.8 *UV lithography schematic. Top left: Photoresist deposition. Top right: Photoresist thickness vs. spinning time at a speed of 3000 rpm. Bottom: exposure, developing and etching processes.*

The resolution of the UV-lithography is reduced by vibrations and non-uniformities in the photoresist film, and the practical limit is 0.5 to 1 μm. The type of photoresist and the processing used will also determine this resolution. In general, the faster the spinning, the thinner the photoresist, giving initially better resolution due to a reduced shadowing effect.

However, as we thin the photoresist, any non-uniformities in the resist thickness become much more pronounced when compared with the actual thickness. This causes some areas to develop before others and may destroy the pattern. A compromise must thus be achieved between the speed, acceleration and time of the spinning to obtain layers which are thin and very uniform. The standard process used in this work is described in the table 3.1. For this work we used a spin coater EMS model 4000 with spin speed from 1 to 9000 rpm and

9 programmable steps, and a hot plate EMS model 1000-1 with temperatures from 50^o C to 150^o C, accuracy of $\pm 1\%$ across the working surface and a possible substrate size of up to 150 mm.

Action	Speed (rpm)	Acceleration (rpm/s)	Time (s)
Dispense Primer	**500**	**1000**	**2**
Spin Primer	**3000/1800**	**1000**	**15**
Dispense Photoresist	**0**	**0**	**0**
Spin Photoresist	**4500**	**3000**	**40**

Table 3.1 *Standard spinning process for the positive photoresist Shipley 1813 used for the lithography process described in section 3.5.8.*

Once the photoresist is developed, we can remove the area of the film that is not protected by the photoresist by milling. This milling is carried out using a Millatron VIII Kaufman type ion gun. This utilises accelerated Ar^+ ions, forming a 20 cm diameter beam which strikes the sample and remove the surface atoms (see fig. 3.9 for a schematic).

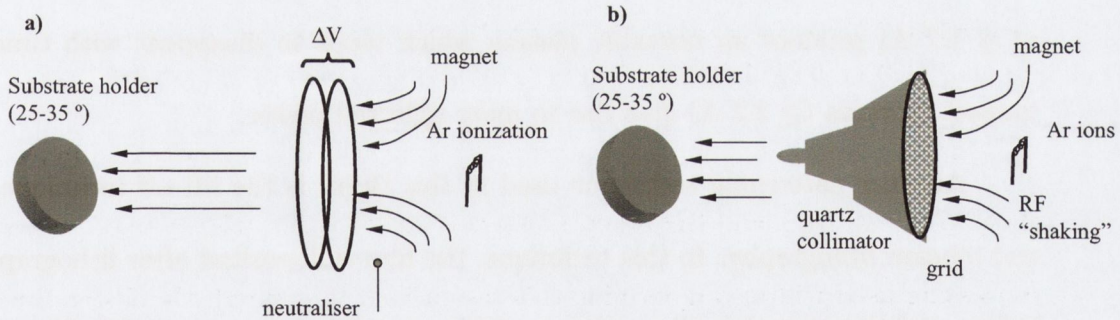

Figure 3.9 *Dry Ar^+ milling schematic for a) DC accelerated and b) RF oscillated and collimated beams. The sample is positioned at an angle for an optimum etching, but needs to be rotated to obtain good uniformity.*

The Ar^+ milling provides ideal atomic resolution for any material. However there are drawbacks with this technique, the main one being the non-selectivity of the ion beam - it will mill any surface in its path. The milling speed however will change between different surfaces, with the milling rate on any resist used being particularly slow. Some milling speeds for typical materials are listed in the table below.

Material	Milling ratio (*)
Gold	10
Silver	6
SiO_2	5
Copper	3
Nickel/Cobalt/Iron	2
LSMO/SFMO	1.5
Magnetite/Nb/Ti	1
Glass	< 1

* **nm/minute** @ 500 W RF power optimised

Table 3.2 *Milling ratios in the Millatron for some different materials.*

Our system is operated with a cryopump, under initial vacuum of $\sim 2 \times 10^{-7}$ torr, a working pressure of 1.8×10^{-5}, gas flow of 0.2 sccm, magnet current of 2 A and a RF power of 500 W. The use of higher gas flow ($\geq$ 0.25 sccm) produces a pink plasma (instead of blue-purple) with almost no milling power. Lower gas flow or magnet current ($\leq$ 0.19 sccm or $\leq$ 1.7 A) produce an unstable plasma which tends to disappear with time, and higher magnet currents ($\geq$ 2.2 A) give rise to more reflected power.

Another patterning technique used in this thesis is the lift-off technique, used in UV and e-beam lithography. In this technique, the film is deposited after lithography instead of before, and therefore doesn't require an etching or milling process. A thin film is deposited on top of a photoresist film previously exposed and developed. After the thin film deposition, the sample is immersed in a strong solvent (usually warm acetone) to dissolve the photoresist and the film on top of it. This way, the film will remain only at the areas which have previously been developed, i.e. the regions where we have removed the photoresist.

To enhance the resolution of optical lithography, extremely short wavelength UV (λ below 200 nm), mirror projection printing (steppers) and phase shift masks are employed in the semiconductor industry. Optical photolithography processes can then be capable of

resolution below 100 nm. However, for higher resolution, other techniques such as electrodeposition, e-beam lithography and ion-beam milling are required.

3.4 Point Contacts

To study of transport properties of nanocontacts one needs contacts that are stable for a sufficiently long time to perform the required measurements. Here we describe the set-up used to investigate the magnetotransport behaviour of point contacts. Point contact phenomena like quantum conductance are most widely studied in nanocontacts formed when two macroscopic electrodes are put into contact and then slowly pulled apart. Precise control over the movements of the electrodes is desirable for the formation of a stable nanocontact.

3.4.1 Point Contact Set-up

In our set-up (see fig. 3.10), the nanocontacts are made by putting two crystallites or metallic pieces into contact and then slowly pulling them apart again. One crystal is mounted on a block of aluminium, while the other is attached to the tip of a piezoactuator. This Physik Instrumente translator is made of stacks of piezo crystals and has a travel length of 45 μm at room temperature. The voltage needed to fully extend the piezo crystals is supplied by a Physik Instrumente E-861.10 Single Channel Amplifier. It accepts up to 10V at the input and amplifies it to up to 100V for the full travel length of the translator.

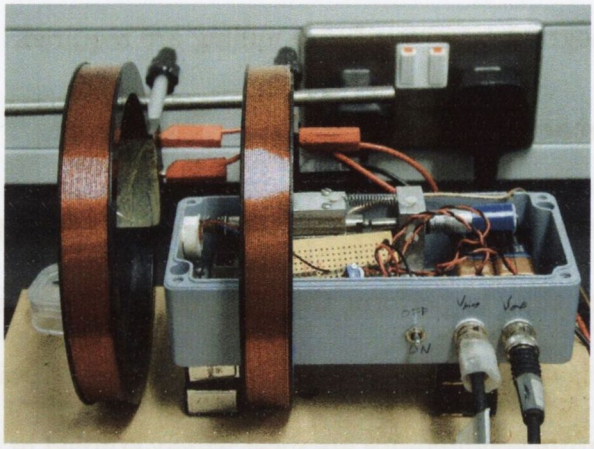

Figure 3.10 *Picture of set-up for creating point conacts.*

The translator itself is mounted on a precision ball slide which can be moved by micrometer screw. This assembly is used for the rough approach of the two crystals. The actual making and breaking of the contacts is done by the piezo translator.

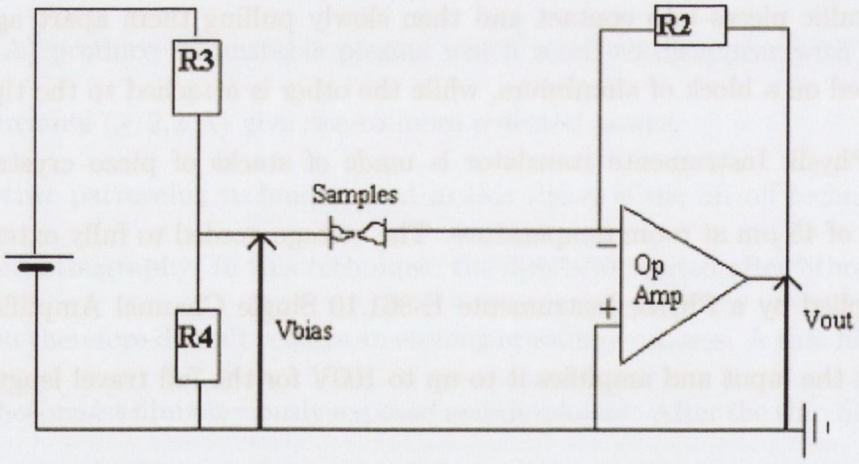

Figure 3.11 *Schematic drawing of the electronics used to measure the conductance of a nanocontact. The voltage source supplies a voltage over the contact, while the current through the contact is converted to a voltage using a OP37 op-amp.*

Both the mechanical set-up and the electronics are mounted in a die-cast box to shield from electrical noise. For vibration insulation, the whole set-up is mounted on a stack of plywood plates separated by Viton O-rings, which are placed on heavy metal plate on top of an inflated tube (from a bicycle tyre).

The voltage source for the set-up can be a battery, a power supply or the output from one of the DAC's from the ADA3100 data acquisition board, controlled by a PC, depending on the measurement required. The output from the I-V convertor can either be viewed and stored on an oscilloscope (Tektronix TDS220 digital storage oscilloscope), or fed directly into a PC using the ADA3100 card. The trace captured by the scope can be read into the computer using the RS232 serial port for further processing.

To study the transport behaviour of the nanocontacts in a small magnetic field, two coils are placed around the die-cast box. The coils are driven by a home-built amplifier which has a -5 V to +5 V input and a -30 V to +30 V output which produces a field of up to 10 mT, which can be applied both parallel and perpendicular to the contact. The field can be controlled by the ADA3100 card.

3.4.2 Software

All the data acquisition software developed for the quantum conductance experiments was written in QuickBasic. Each experiment has its own program: measuring the conductance while slowly breaking the contact, measuring the current-voltage characteristics of a stable nanocontact, and the magnetoresistance of a stable nanocontact.

For measuring the conductance of a breaking nanocontact, the program first initializes the ADA3100 card and communications port. The scope is also initialized, setting it to single shot mode, and its trigger level to a few multiples of G_0, the quantum of conductance (see section 2.1.1). The user has to manually bring the two crystallites into contact, using the micrometer screw, after which the program will make and break the contacts automatically using the piezo translator. After a contact has been established, the program reduces the voltage at the piezo amplifier input through one of the ADA3100 analogue output ports,

thereby retracting the translator, and checking the scope until it has been triggered. The scope stores the trace in its internal memory, which can be accessed through a serial port. The data is plotted on the screen and automatically saved as a file. The two crystals are then put into contact again, and the next trace is obtained and saved. In this way hundreds of breaking curves can be obtained automatically, which can then be analysed in the form of a histogram. This technique is used to observe quantised conductance in samples.

For measuring I-V curves of a stable nanowire, one of the analogue output ports of the ADA3100 has to be connected to the V_{source} input, and the V_{output} output has to be connected to one of the analogue input of the ADA3100. Once the contact is made the translator is slowly retracted. Using an applied bias voltage of 30 mV, the value of the conductance of the nanocontact is constantly measured. We can thus adjust the voltage across the piezo translator until we get the conductance we require. The voltage across the nanocontact, V_{bias}, is then swept from about -0.8 V to +0.8 V and back, at a preset speed. V_{output}, which is a function of the current, is plotted on screen against V_{bias} and stored in a file. After thus obtaining an I-V curve, the V_{bias} is set again at 30 mV, a new contact is made, and another I-V curve obtained.

The program for measuring the magnetoresistance of a nanocontact is much the same as that for obtaining I-V curves. The V_{source} input is now connected to a battery, giving a 30 mV voltage difference over the nanocontact, while one of the analogue output of the ADA3100 is connected to the input coils amplifier. Again, the contact is made and the translator slowly retracted. When the conductance of the nanocontact reaches the desired level, the magnetic field is cycled between +10 mT and -10 mT perpendicular to the current direction. The program plots V_{output} and the voltage output to the coil amplifier on the

screen and saves the data in a file. Magnetoresistance can also be observed by taking I-V curves as before both with and without an applied magnetic field. The resistances can be calculated from the I-V curves and then compared.

3.5 Andreev Reflection

As mentioned previously, Andreev reflection ideally requires the formation of a ballistic electrical contact between a subject material and a superconductor. Initially niobium was used as our superconducting material. Bulk niobium has a transition temperature of 9.25 K, however this reduces for thin films, depending on the thickness of the film[2]. We then started to use lead as it is an easier material to deposit, and its transition temperature (7.2 K) is sufficiently high for our requirements. Several techniques were used to create the actual nanocontacts. These are described in detail below.

3.5.1 Sharpened Niobium wire

In this technique, a section of niobium wire (0.25 mm diameter) was sharpened using a polisher and used to create a nanocontact with the subject metal. The actual nanocontact was created using a technique similar to that described in section 3.4.1. A specially designed probe is fitted with piezo actuators and a micrometer screw gauge. These are used to slowly control the distance between the wire and the sample until a nanocontact is formed. The resistance between the sample and the niobium wire is continually monitored and thus an estimation of the size of the point contact can be made. Point contacts could be made for several minutes, enough time for a few conductance curves to be measured. The sample rod was wired up using copper wire and EPOTEK E4110 conductive low-temperature epoxy, and silver wire with Agar Scientific quick drying silver paint. The sample holders and piezo

tube were mounted using EPOTEK H77 low-temperature nonconductive epoxy.

To cool the system below the transition temperature of the niobium wire, the sample probe is placed into a custom designed Oxford cryostat (fig. 3.12). The continuous flow cryostat has a Cernox temperature sensor and heating element placed just after the needle valve between cryogenic reservoir and sample space which controls the temperature in the cold region of the cryostat, which is situated inside the tail. The reservoir of the cryostat is precooled with liquid nitrogen overnight before filling with liquid helium.

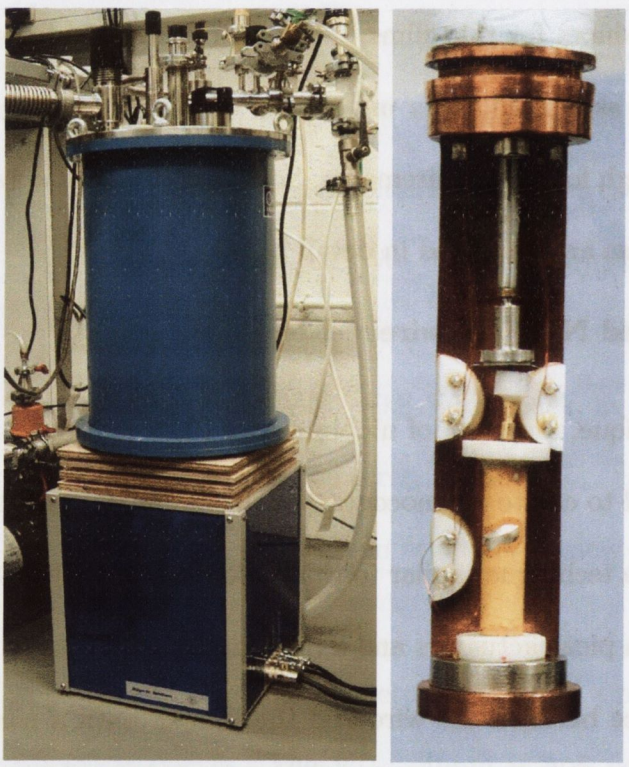

Figure 3.12 *Photo of the Niobium tip PCAR measurement set-up. a) Cryostat with its tail sitting inside a Multimag variable field source. b) Close up of the sample rod with piezo tube.*

To measure conductance curves, an AC lock-in technique is used (fig 3.13). A Keithley 6221 AC current source sends an oscillating current across the contact. A PerkinElmer 7265 lock-in amplifier is then used to measure the resulting voltage change across the sample, thus giving us a direct differential measurement of the resistance of the contact. A Keithley 2400 sourcemeter is used to step the bias voltage. The whole measurement process is controlled

by PC using a command programme written in Labview. The technique described here was successfully used to perform PCAR measurements on copper, cobalt and nickel.

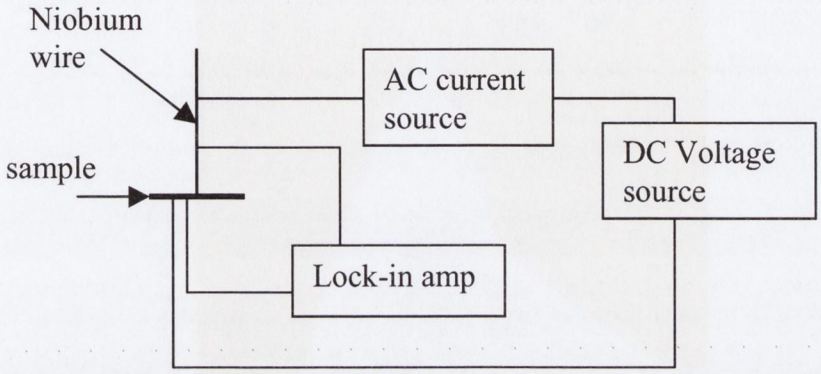

Figure 3.13 *Block diagram of circuit used for measurement of conductance as a function applied voltage.*

3.5.2 Deposition through a nanohole in PMMA

Another way of creating a nanocontact is to deposit through a nanohole made through a layer of PMMA (polymethyl-methacrylate) [3], [4]. The nanohole is made by penetrating the PMMA layer using an AFM tip. A layer of PMMA is spun onto a sample, which in this case should be a smooth film of the subject material. A spin speed of 7000 rpm was used for a duration of one minute, giving an even 80nm thick PMMA layer. The PMMA used was PMMA A2, an anisole based photoresist produced by Micro-Chem. The samples were then 'soft-baked' at 180° C for 2 minutes. This is so the PMMA layer is rigid enough to maintain the dimensions of any hole produced, but soft enough to allow the AFM tip to penetrate easily.

To create the nanoholes, a Veeco TESP tapping-AFM tip (fig. 3.14) is used in a Digital Instruments Multimode AFM. Such tips have an end diameter of < 15 nm and are thus ideal for this application. A 'sacrificial sample' is then used to test the conditions required to create the perfect nanohole, as they will change depending on such factors of the spring constant of the tip, the consistency of the PMMA etc. The AFM is set to contact mode and a deflection

setpoint is used to press the tip into the sample.

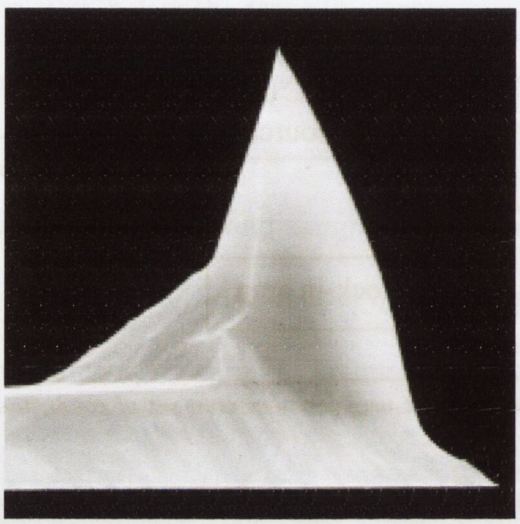

Figure 3.14 *Profile of tapping AFM tip used for creating nanoholes. The end radius is < 15 nm and the tip angle is typically 40°.*

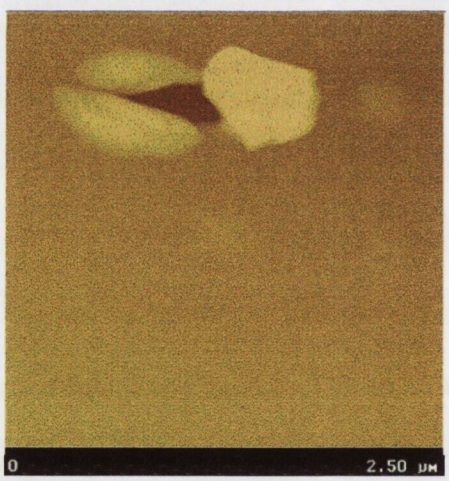

Figure 3.15 *Image of nanohole in PMMA layer taken in tapping mode.*

The tip deflection should be such that the tip just passes through the PMMA layer fully - any more will cause the tip to scrape along the surface of the sample as it is pushed against it, thus forming too large a contact. Various holes are made and imaged until a desirable hole is obtained - a deflection setpoint of ≈7 V is typical. The hole can then be imaged by switching the system to tapping mode and scanning the surface (fig. 3.15). A depth profile of the nanohole can then be obtained (fig. 3.16). Note that the imaged formed

is a convolution of the tip profile and the hole, which is the same size of the tip. However imaging still enables us to get a rough estimation of the hole width and depth. Once the settings and conditions are optimised, a nanohole can be made on each sample. A layer of lead is then deposited onto the samples using an evaporator. A reasonably thick layer (>100 nm) is used to ensure a good transition temperature. Kapton tape is placed around the edges before deposition to prevent shorting between the lead layer and the sample, and also to enable electrical contacts to be made onto the sample layer.

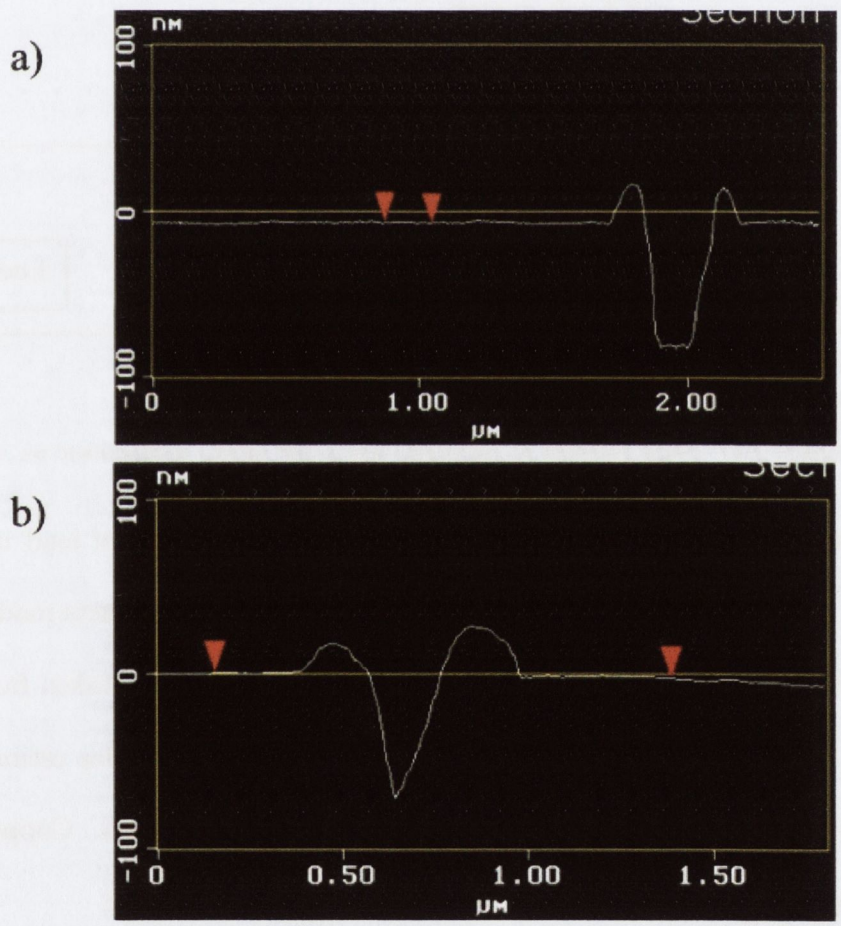

Figure 3.16 *Depth profile of nanoholes created using an AFM tip. In a), the tip has been pressed too hard and a plateau has formed at the base of the hole. In b), the tip has just about passed through 80 nm of PMMA, creating a good nanohole.*

Once the lead has been deposited, electrical contacts are made on the sample and on the lead layer using Agar silver paint. Conductance curves are then obtained using a lock-in

technique slightly different to the one described above. In this case we use two PerkinElmer 7265 lock-in amplifiers and an Agilent 33120A AC voltage source. One of the lock-ins is used to measure the differential voltage across a shunt resistor of known resistance, thus effectively measuring the current passing through the nanocontact. The other measures the differential voltage across the nanocontact. A Keithley 2400 sourcemeter is used to step the bias voltage and the whole measurement process is controlled using a Labview programme.

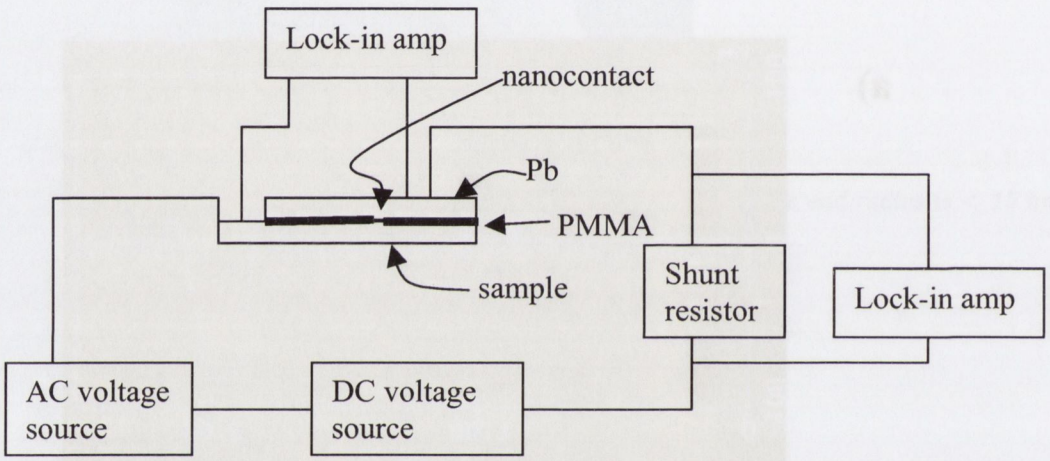

Figure 3.17 *Block diagram of electronic set-up for taking conductance vs. voltage curves.*

The sample is cooled below the transition temperature of lead in a SQUID magnetometer. Measurements were taken at 4.2 K and 2 K. Nanocontacts made using this method are extremely stable and an indefinite number of curves can be taken from one sample. The imaging technique also means that a reasonably accurate holesize estimation can be made, and also holes of various sizes can be produced for comparison. Copper, nickel, Co_2MnSi and ϵ-$Fe_{2-3}N$ were all successfully analysed using this technique.

3.5.3 Lateral Nanojunctions

A method was developed in collaboration with another PhD student (Dr. Oscar Cespedes) to create lateral Andreev contacts. An 8 step process was developed (see figure 3.18): a) a Nb film about 50 nm thick is deposited and the transition temperature measured, b)

half of the film is covered with photoresist, the other half is developed by UV lithography, c) half of the Nb film is etched by Ar^+ milling and the total milled depth is measured by AFM, d) a Cu or Ni film of equal thickness to the total milled depth is sputtered, e) the Cu or Ni on top of the photoresist is lifted off with acetone at 60 °C, f) contact pads and a 20 μm track are lithographed, g) the uncovered film is milled and h) a nanoconstriction is milled at the interface using focussed ion beam (FIB).

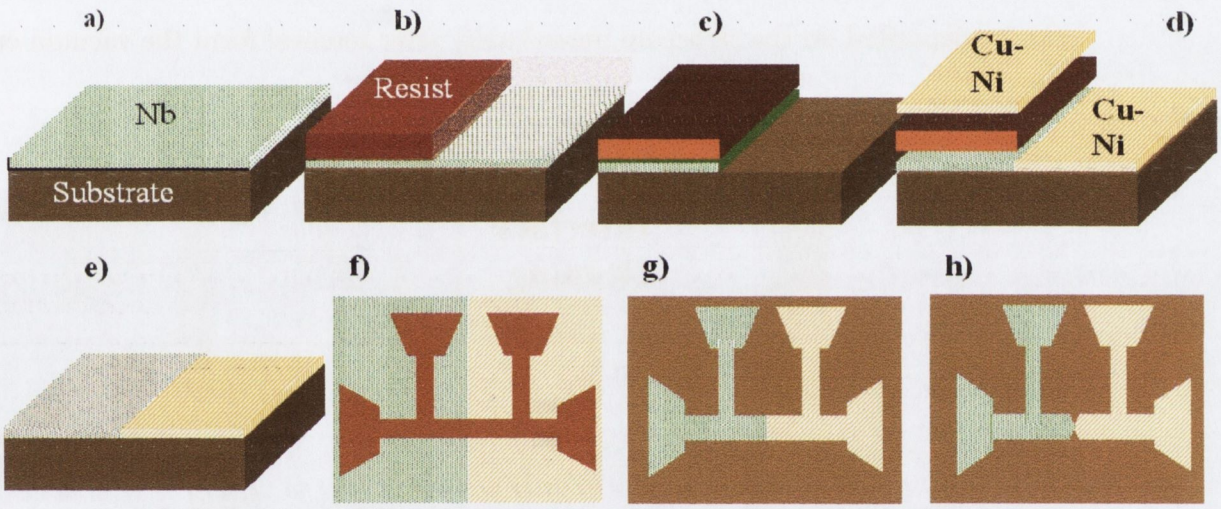

Figure 3.18 *Schematic of the eight steps fabrication process as described in the text.*

To fabricate an edge junction following this method, the first step is to measure the transition temperature of the deposited Nb film. The drop in transition temperature with film thickness is well documented for niobium [5], [6], and has its basis in an enhanced Coulomb repulsive interaction, which depresses the density of states [7].

One problem to take into consideration with this technique is that the Nb film is milled at a much slower rate than the SiO_2 substrate. As a result, a precise thickness measurement is required to find the exact amount of metal to be deposited so that both thin films are at the same height. Another problem is associated with the lift-off process, which sometimes leaves

a layer of the subject material overlapping the niobium film. To create a nanoconstriction at the boundary between both films we need to remove this overlapping metal layer (see fig. 3.19a). Furthermore, once the sample is taken out of the vacuum environment of the FIB system, it starts to oxidize. The top of the Nb film is covered by a Au capping layer, but the walls of the nanostructure are exposed. To prevent damage, a layer of insulator SiO_2 can be deposited on top of the nanostructure (see fig. 3.19b). Alternately, a layer of photoresist can be deposited on the structure immediately after removal form the vacuum environment of the FIB.

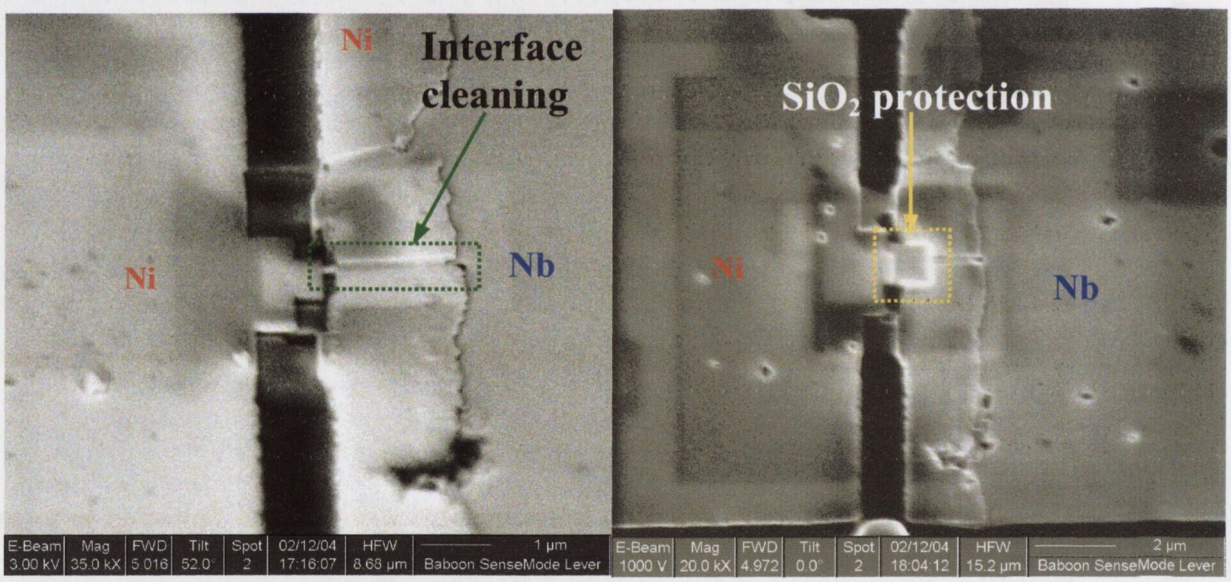

Figure 3.19 *a) The lift off process may leave a layer of subject metal overlapping the niobium film. This must be removed using the FIB. b) SiO_2 may be deposited to protect the walls of the constriction.*

The bad quality of the interface may enhance another problem: temperature-dependent strain of the films. This strain is in some instances large enough to open a gap between both films at low temperature. This process is reversible, and the nanocontact can be formed once more by increasing the temperature, but if the gap is opened at a temperature above the superconducting transition, the sample will obviously be useless for Andreev reflection measurements (an example is presented in fig. 3.20).

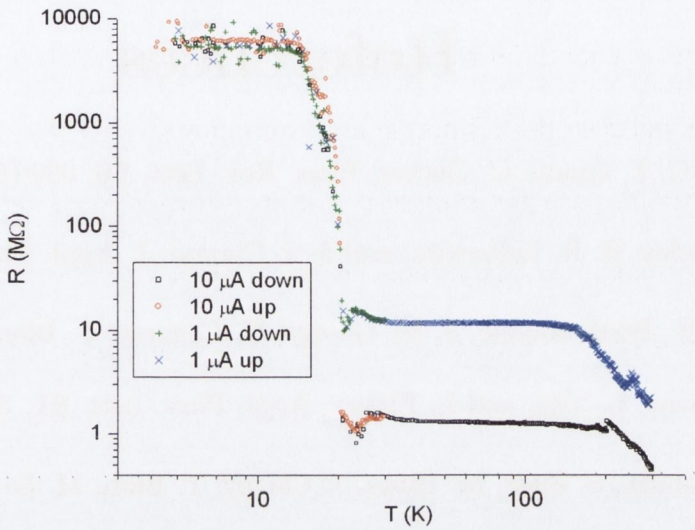

Figure 3.20 *Temperature induced strain on the metallic films, together with poor bonding at the interface, may lead to a jump in the resistance of a device, leaving it in the insulator regime. The effect is reversible with temperature and independent of the current used in the measuring process.*

All these experimental difficulties, together with the numerous patterning steps, have as consequence a very low success rate for Andreev reflection in the edge junctions. Only around 1% of the initially lithographed samples present a good contact with a clean interface. Conductance curves can be obtained from these samples at low temperatures using the SQUID magnetometer and the measurement set-up described on page 69. This technique was successfully used to measure polarisation in copper and nickel.

References

[1] G. Binnig, C. F. Quate, C. Gerber, Phys. Rev. Lett. **56**, 930 (1986).

[2] A. F. Mayadas, R. B. Laibowitz, and J. J. Cuomo, J. Appl. Phys. **43**, 1287 (1972).

[3] J. Carrey, K. Bouzehouane, J. M. George, C. Ceneray, T. Blon, M. Bibes, A. Vaurès, S. Fusil, S. Kenane, L. Vila, and L. Piraux, Appl. Phys. Lett. **81**, 760 (2002).

[4] K. Bouzehouane, S. Fusil, M. Bibes, J. Carrey, T. Blon, M. Le Dû, P. Seneor, V. Cros, and L. Vila, Nano Letters **3,** 1599 (2003).

[5] M. S. M. Minhaj, S. Meepagala, J. T. Chen, and L. E. Wenger, Phys. Rev. B **49**, 15235 (1994).

[6] Q. D. Jiang, Y.L. Xie, W.B Zhang, H. Gu, Z.Y. Ye, K. Wu, J.L. Zhang, C.Y. Li and D.L.Yin, J. Phys.: Condens. Matter **2,** 3567 (1990).

[7] S. Maekawa and H. Fukuyama, J. Phys. Soc. Jpn. **51**, 1380 (1981).

Chapter 4

Materials

In this chapter the materials studied within the scope of the thesis are discussed. These materials were examined to determine their spin polarisation and thus their suitability for spin-electronic applications. Many of them are predicted to be half-metallic.

4.1 Magnetite

Magnetite (Fe_3O_4) is the oldest known magnetic material. Naturally magnetized lodestone was used as a compass in China as far back as 100 A.D., and it has been the subject of intensive study due to its interesting magnetic and transport properties [1], [2]. It is a ferrimagnet with a Curie temperature of 860 K and a cubic inverse spinel lattice structure (see fig. 4.1), with the tetrahedral sites occupied by the ferric Fe^{3+} ions, and the octahedral sites shared by ferrous Fe^{2+} and Fe^{3+} ions. It can be seen as a face centered cubic lattice of oxygen anions with the iron cations situated on the interstices. The lattice parameter is 0.8398 nm [2].

From an ionic point of view, magnetite can thus be written as $Fe_A^{3+}[Fe^{3+}Fe^{2+}]_B O_4^{2-}$, where A and B denote the tetrahedral and octrahedal sites, respectively. Both the Fe^{2+} and Fe^{3+} ions are in the high-spin state, i.e. $S = 2$ and $S = \frac{5}{2}$, respectively. One half of the Fe^{3+} ions occupy tetrahedral A-sites, the other half half of the octahedral B-sites. Since these two sublattices are coupled antiferromagnetically via superexchange, their 5 μ_B moments cancel out, and the total net moment $\simeq 4\ \mu_B$ per formula unit Fe_3O_4 comes from the Fe^{2+} ion on the octrahedral B-site.

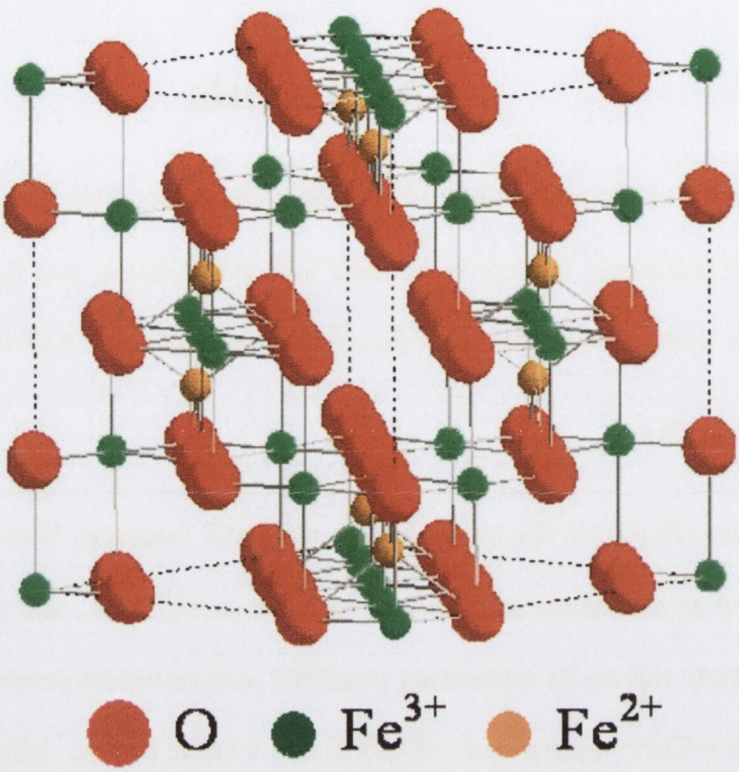

Figure 4.1 *Crystal structure of magnetite. The oxygen anions form a fcc lattice, with iron cations placed on the interstices.*

Magnetite is a type IIB half metal, conducting via electron hopping. $3d{\downarrow}t_{2g}$(Fe) electrons form polarons and hop among the B-sites in a fully $\downarrow$ polarised band [3]. Following previous studies on single crystal magnetite point contacts [4], contacts were made from a natural bulk polycrystalline sample. XRD analysis produced sharp peaks (fig. 4.2), which indicates a well-defined crystalline structure. Polycrystalline samples of magnetite plated with $\approx$ 10 nm of gold were also examined. These samples were supplied by Dr. W. Egelhoff at the National Institute of Standards and Technology (NIST) in Washington.

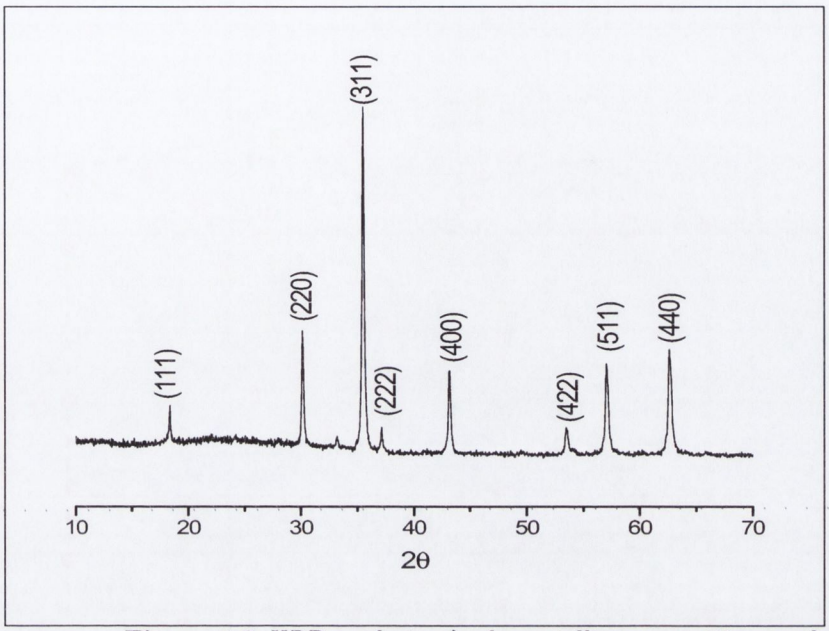

Figure 4.2 *XRD analysis of polycrystalline magnetite sample.*

4.2 SFMO

SFMO (Sr_2FeMoO_6) is a ferrimagnetic material with a double perovskite structure (see fig. 4.3). It has been classified as a type IB half metal [5]. It is a ferromagnet with a Curie temperature $T_C = 426$ K, and a saturation magnetisation of $4\mu_B$ per formula unit. It has a shiny black colour, and a room temperature resistivity of $\approx 4 \times 10^6$ Ω m. Single crystals of SFMO were grown by P. Berthet, at the Universite Paris Sud, using a laser imaging furnace. These were then used to make point contacts.

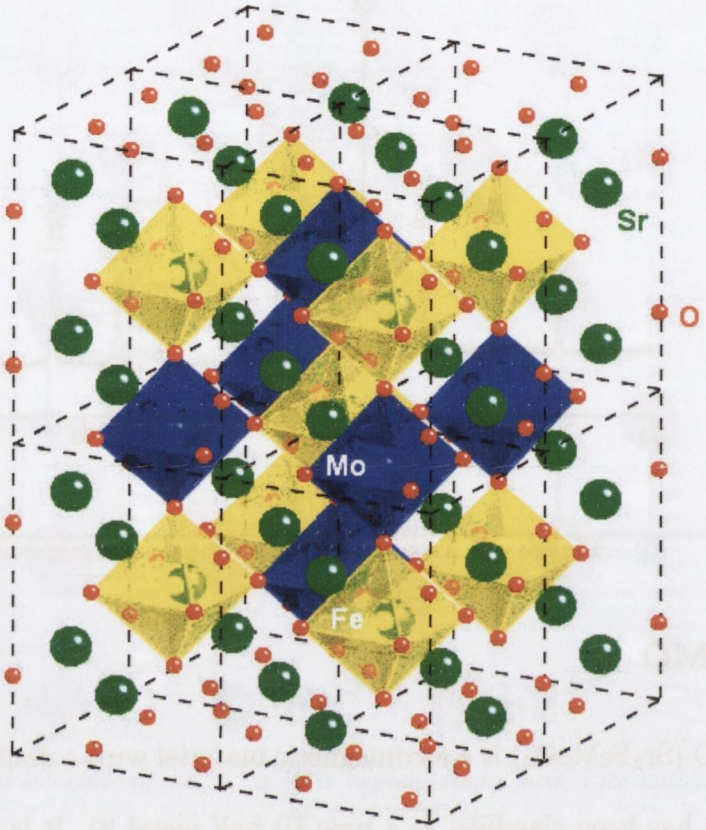

Figure 4.3 *Representation of an SFMO crystal, showing its double perovskite structure.*

4.3 MnBi

MnBi is an intermetallic compound. It has a high temperature zincblende phase ($Mn_{1.08}Bi$) with a transition temperature at 613 K. Below this it forms a hexagonal NiAs structure (see fig. 4.4). Recent calculations have suggested that this structure may be a type III half metal [6], with one of its spin bands highly localised so that only electrons with the opposite spin direction contribute significantly toward conduction.

MnBi has a coercivity which increases with increasing temperature, making it very interesting for high temperature magnetic applications. It also has good magneto-optical properties, with the Kerr rotation angle $\theta_K = 0.9°$ at a wavelength of 633 nm. Its Curie

temperature cannot be determined directly due to its phase transition; however data fitting suggests it has an estimated T_C of 775 K [7]. MnBi also has significant magnetocrystalline anisotropy, with $K_1 \simeq 1.2$ MJ m^{-3} at room temperature. This also increases with temperature, and an anisotropy field of 9 T at 512 K has been reported [7].

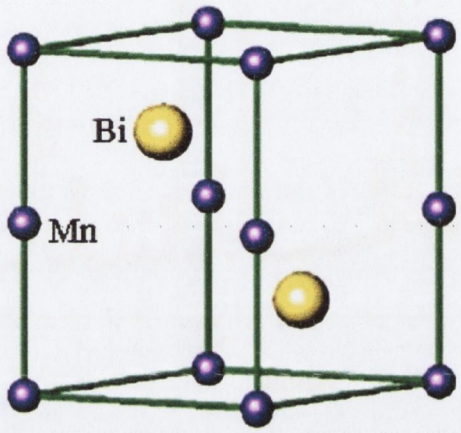

Figure 4.4 *Unit cell of the low temperature phase of MnBi. It shows a hexagonal NiAs structure.*

MnBi was formed in the lab by arc melting high purity (99.98%) manganese and bismuth (99.999%) under argon. This was repeated 3 or 4 times. The resulting sample was then slowly annealed in a vacuum at a rate of 3 K/min to 570 K. XRD analysis showed Mn and Bi peaks amongst the low-temperature phase MnBi (see fig. 4.5). SQUID measurements showed a magnetisation value of 0.9 μ_B/f.u.(see fig. 4.6). SEM and EDAX pictures showed both manganese rich and bismuth rich regions together with regions of MnBi (see fig. 4.7). An estimate of the concentration gives a composition of 75-80% MnBi, with the rest mostly bismuth clusters. This compares favourably with previous efforts using this method [8].

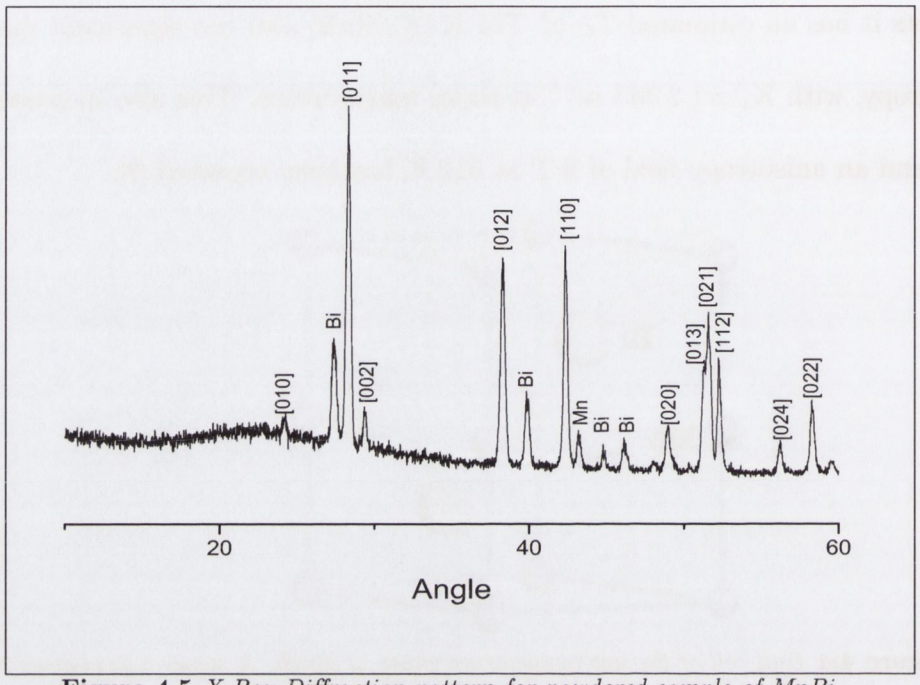

Figure 4.5 *X-Ray Diffraction pattern for powdered sample of MnBi.*

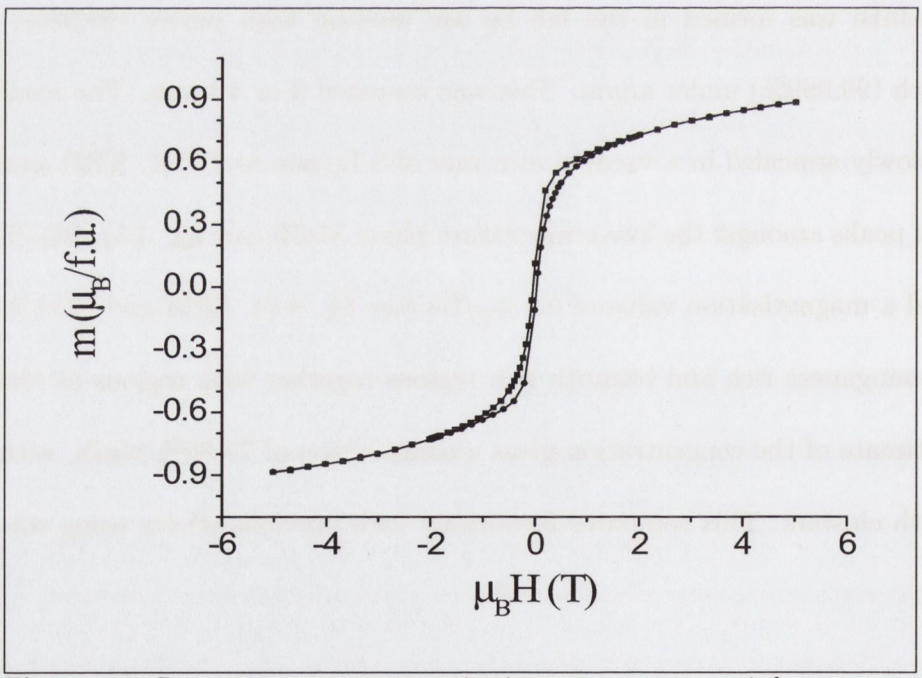

Figure 4.6. Room temperature magnetization measurement carried out on an MnBi sample in the SQUID magnetometer.

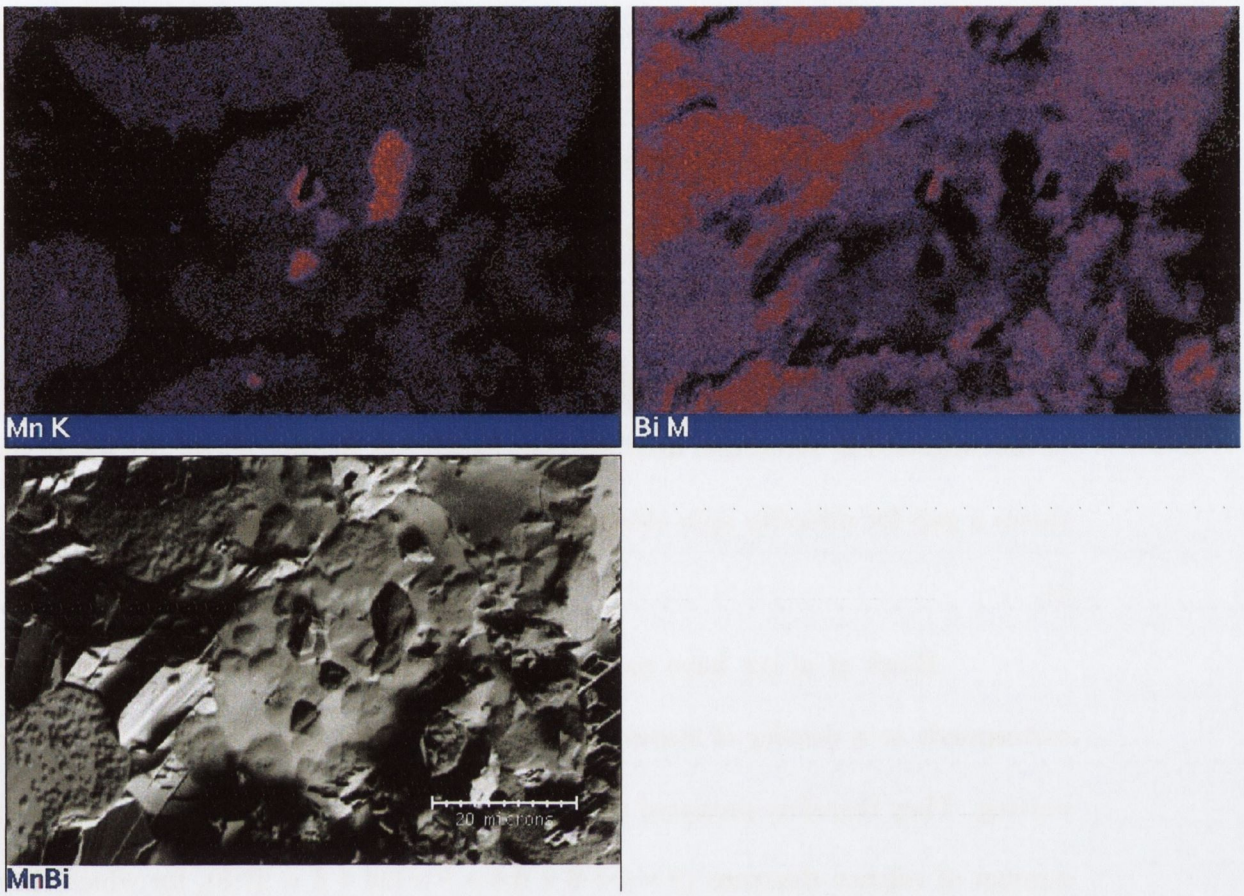

Figure 4.7 *SEM and EDAX of an MnBi sample. In the EDAX images (top), brighter spots indicate higher concentrations of the particular element (Mn on left, Bi on right). Dark spots indicate a lack of that element. Relatively large areas of pure bismuth can be seen to the left of the image, while a clump of manganese sits in the centre.*

4.4 $Co_2Cr_{0.6}Fe_{0.4}Al$

Co_2FeAl is a Heusler alloy with a Curie temperature $T_C = 340$ K. A Heusler alloy was originally defined as any magnetic alloy composed of metals that, in their pure state, are not magnetic [9]. The alloys are named after Fritz Heusler, 19th-century German mining engineer and chemist. Nowadays the term refers to magnetic face centred cubic alloys with a specific structure. The Heusler structures consist of four interpenetrating fcc sublattices with atoms at X_1 (0,0,0), X_2 (1/2, 1/2,1/2), Y (1/4, 1/4, 1/4) and Z (3/4, 3/4, 3/4), some of which may or may not be filled. Full Heusler alloys have the X_2YZ structure and all the

sublattices are filled. Half-Heusler alloys have the XYZ, where the X_1 sublattice is empty. There has recently been a focus on Heusler alloys [10] for spin electronic applications. They are semimetallic or semiconducting when formed of non-magnetic elements with a valence electron count of 24 per formula unit [11]. Ferromagnetic alloys with a greater number of electrons are candidate half-metals. Co_2CrAl, for example, has 27 valence electrons and is in the ordered $L2_1$ structure, as is the case for all full Heusler alloys. Its electronic structure shows a gap for minority spin electrons at the Fermi energy. It is thus a type IA half metal [5].

Block et al [12] have recently argued that the ideal electron count is 27.8, which corresponds to a density of states peak in the majority spin electrons due to Fermi surface nesting. They therefore prepared the compound $Co_2Cr_{0.6}Fe_{0.4}Al$, with precisely the requisite number of valence electrons ($9 \times 2 + 6 \times 0.6 + 8 \times 0.4 + 3 = 27.8$), for which they found T_C = 640 K.

We reproduced this alloy by arc-melting the constituent elements and then remelting with extra aluminium to compensate for weight loss. No annealing was carried out on the alloys. Arc-melted pieces were ground to powder using a steel percussion mortar for sample characterisation measurements. X-ray diffraction indicated a B2 structure (fig. 4.8) with a_0 = 573.6 pm. The B2 structure is essentially the same as the $L2_1$, except that there is disorder in the atomic structure. This is reflected by the lack of a (111) peak in the XRD pattern, which would normally be at $2\theta = 27°$. The (111) peak is a superlattice reflection, and its suppression indicates complete disorder beween the Al and both Cr and Fe atoms. However, the Co atoms are ordered within their sublattice, and this is shown by a sharp (200) superlattice peak.

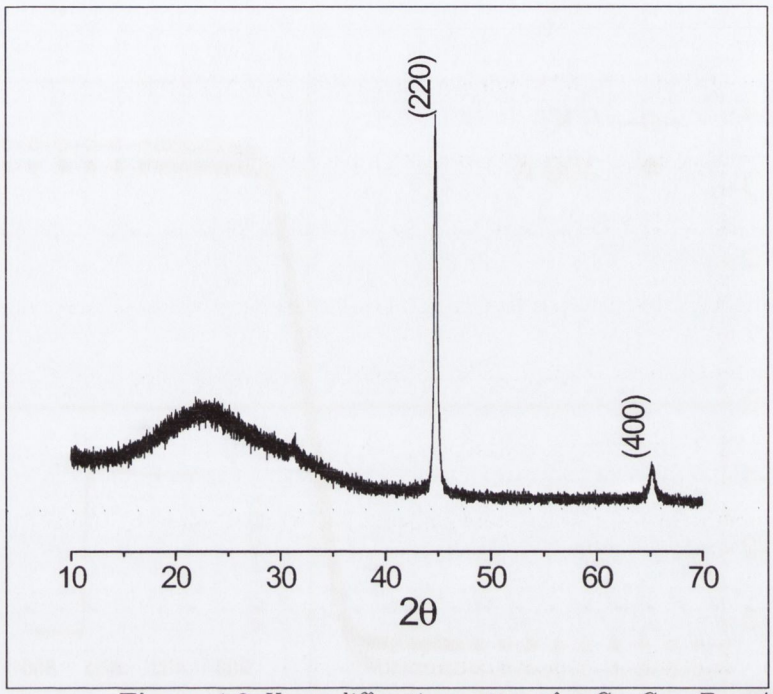

Figure 4.8 *X-ray diffraction pattern for* $Co_2Cr_{0.6}Fe_{0.4}Al$.

Magnetisation was measured using a SQUID magnetometer. The magnetisation curves (fig. 4.9) show the alloy to be a soft ferromagnet with a low-temperature saturated moment of 3.65 μ_B per formula unit, very close to the value of 3.7 μ_B predicted from the band structure calculations [13]. The Curie temperature of the alloy was found to be 665 $\pm$ 2 K. Resistivity at room temperature was 60 $\mu\Omega$ cm.

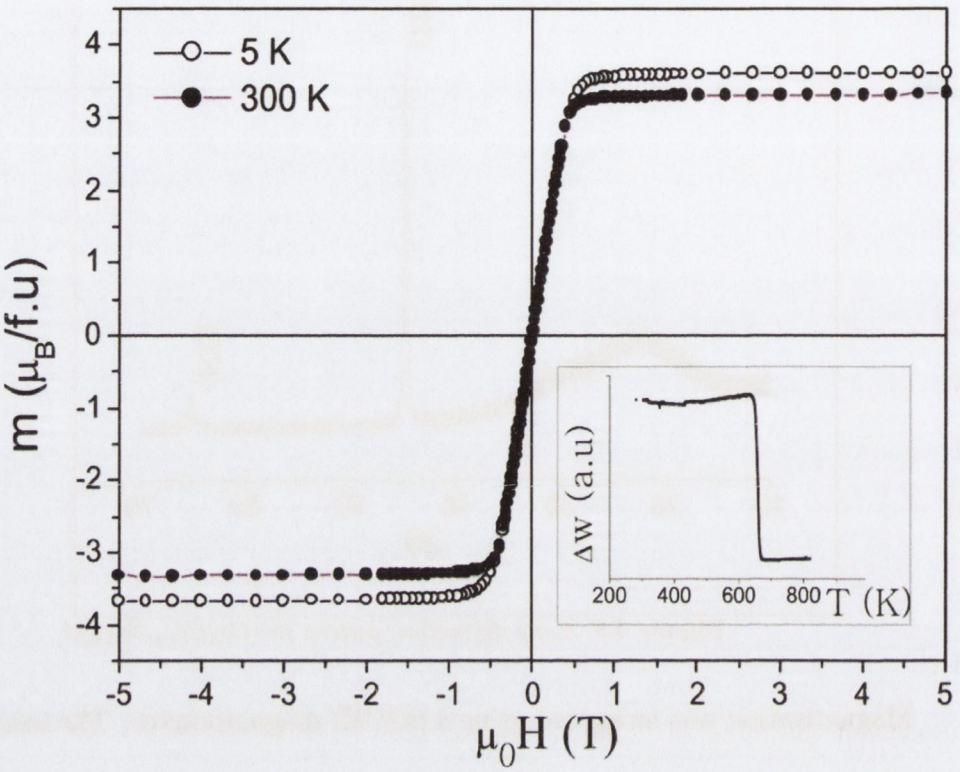

Figure 4.9 *Magnetisation loop of $Co_2Cr_{0.6}Fe_{0.4}Al$ at both room temperature and 5 K. The insert shows a measurement of the Curie temperature.*

Mössbauer spectra were obtained using a conventional constant-acceleration spectrometer with a source of 57 Co in Rh. The Mössbauer spectrum (fig. 4.10) shows a well-ordered structure with 90% of the absorption in a magnetically split pattern with a hyperfine field B_{hf} = 28.8 T, and a small central peak. The isomer shift is -0.10 mm s^{-1} relative to Fe in a Rh matrix and the quadrupole shift is 0.16 mm s^{-1}. The spectrum at 60 K shows a hyperfine field B_{hf} = 29.9 T and a similar central peak. This central peak is attributed to iron in environments with more Al and fewer Co neighbours than the expected (X, Z) (8,6) coordination, due to disorder of the X and Z sublattices. Extra aluminium neighbours tend to destroy the iron moment.

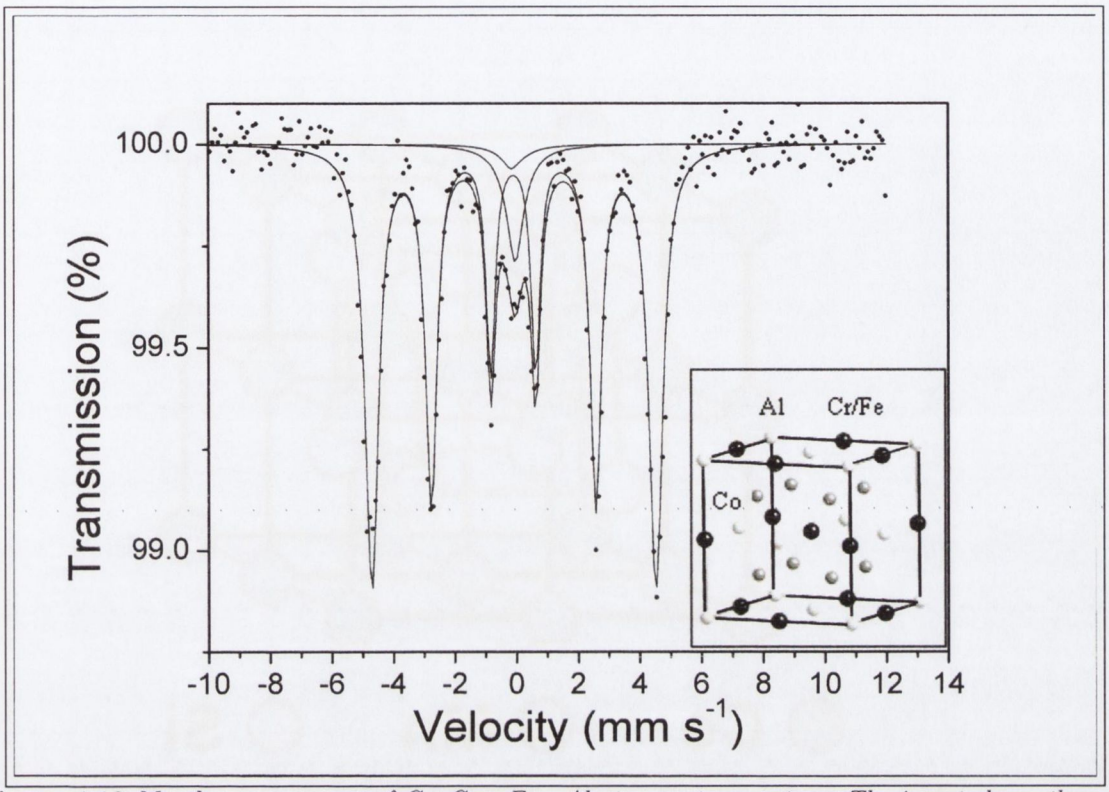

Figure 4.10 *Mossbauer spectrum of $Co_2Cr_{0.6}Fe_{0.4}Al$ at room temperature. The insert shows the ordered $L2_1$, X_2YZ structure, where Fe (Y) is in (8,6) coordination (8-Co, 6-Al).*

4.5 Co_2MnSi

Co_2MnSi is a particularly promising Heusler alloy, predicted to have a large energy gap in the minority band of 0.4 eV [14] and has a measured Curie temperature of 985 K [15], the highest amongst the known Heuslers. Co_2MnSi crystallizes in the $L2_1$ structure. The unit cell can be visualized as four interpenetrating fcc lattices, each occupied by one of the participating elements, as indicated in fig. 4.11. Co atoms occupy the X_1 and X_2 sublattices, with Mn occupying the Y sublattice and Si the Z. The manganese atoms are coupled to each other, and coupling also exists between the Mn and Co atoms, causing strong ferromagnetic behaviour in the material.

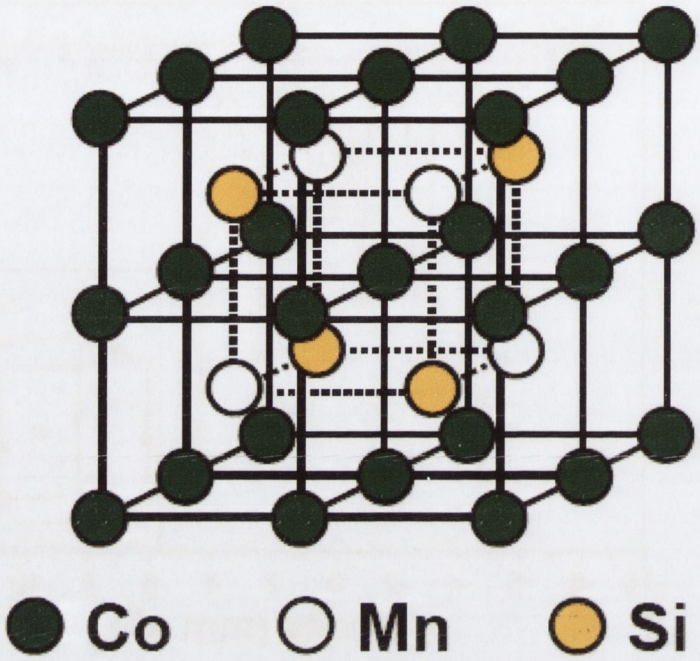

Figure 4.11 *Assembly of atoms in the Co2MnSi unit cell displaying the $L2_1$ structure: four interpenetrating fcc lattices, each occupied by one of the elements (Co, Co, Mn, and Si).*

Films of Co_2MnSi were grown by sputtering onto a silicon substrate. Samples were post-annealed under vacuum at 500° C for 2 hours. XRD analysis confirms the $L2_1$ structure (fig. 4.12).

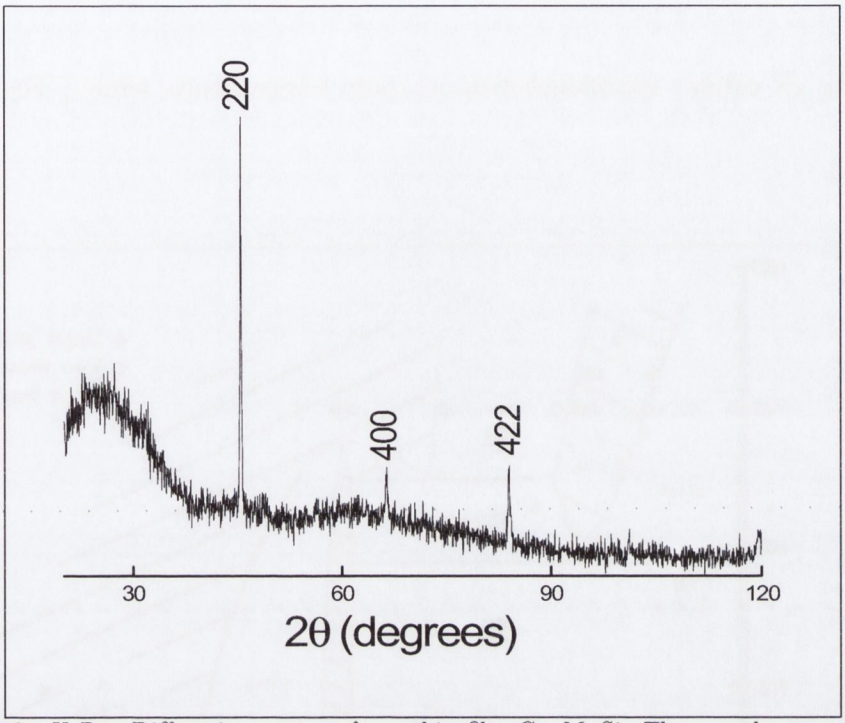

Figure 4.12. *X-Ray Diffraction pattern for a thin film Co_2MnSi. The sample was annealed under vacuum after sputtering for 2 hours at 500° C.*

4.6 ε-$Fe_{2-3}N$

The properties of iron-nitrogen systems have been investigated since the first half of the previous century, with extensive research carried out by Jack in the late 1940's and early 1950's [16]. This early interest was generated largely due to their roles in steel technology. However more recently a focus has been placed on their magnetic properties, which combined with their high corrosion and wear resistance make them strong contenders for magnetic data storage applications.

It has been found that iron nitride has a variety of phases with different crystal structures and magnetic properties owing to different nitrogen contents (see fig. 4.13). These are α''-$Fe_{16}N_2$ (BCT structure) [17],[18], γ'-Fe_4N (FCC structure)[19], [20], ϵ-$Fe_{2-3}N$ (hexagonal structure) [19] and ζ-Fe_2N (orthorhombic structure) [21]. Moreover, α''-$Fe_{16}N_2$, γ'-Fe_4N

and ϵ-$Fe_{2-3}N$ exhibit ferromagnetism at room temperature, while ζ-Fe_2N exhibits paramagnetism.

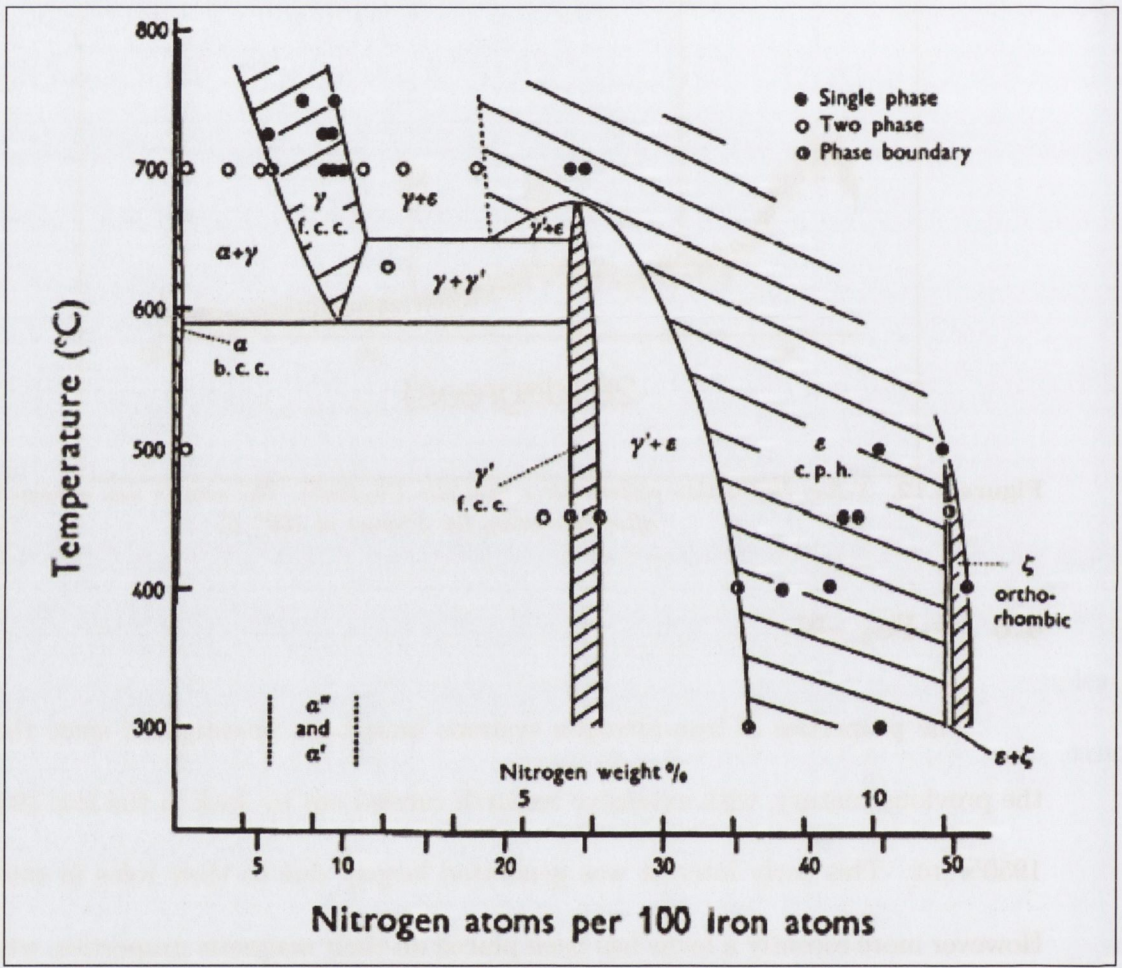

Figure 4.13 *Iron-nitrogen phase diagram* [16]

Iron-nitride films were grown in a Leybold Z550-S DC-magnetron sputtering machine using similar conditions to those described in [22]. The samples were grown on two inch Si (1 0 0) wafers. A 6 inch disk of pure iron (99.99 %) was used as the sputtering target. Two films were grown at 400 K, in an Ar/N_2 mixture. The base pressure of the chamber was 1.5×10^{-4} mbar, a nitrogen partial pressure of 2.5×10^{-4} mbar was used for the first film and 2.1×10^{-4} mbar for the second. The total pressure was 1.65×10^{-3} mbar. The DC power was 24 W and the film thickness was 120 nm for both.

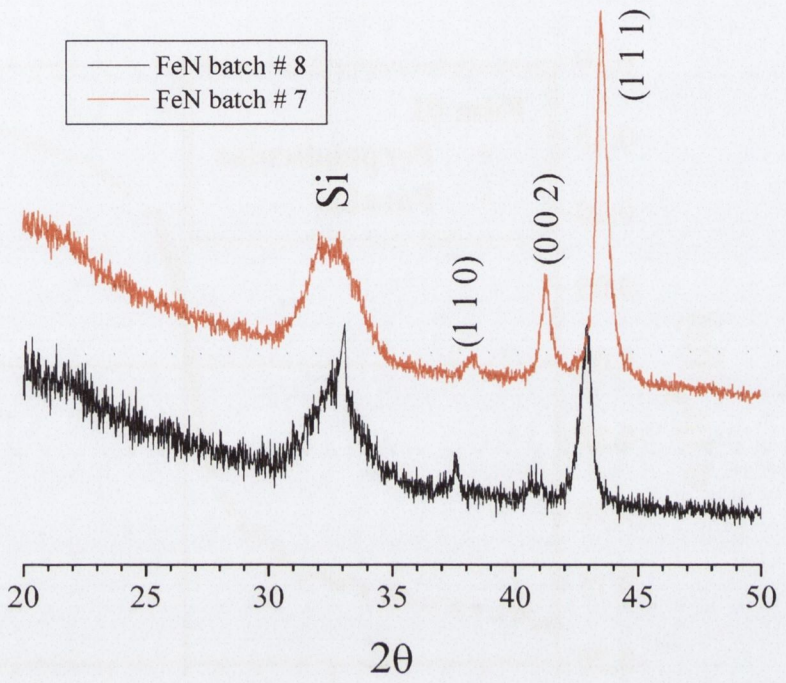

Figure 4.14 *X-ray diffraction pattern for iron nitride films. The peaks for Fe_3N are indicated.*

XRD analysis confirmed the hexagonal ε-$Fe_{2-3}N$ phase (see fig. 4.14), with the (1 0 0), (0 0 2), and (1 0 1) reflections clearly visible. The peaks are shifted for the second film, showing a reduction in the lattice parameters. This smaller unit cell is indicitave of a lower nitrogen concentration. Magnetisation measurements were carried out at 4.2 K using a Quantum Design SQUID magnetometer (figs. 4.15, 4.16). The first film showed isotropic behaviour, with no difference observed between in-plane and out-of-plane measurements. Magnetisation is unsaturated even at a field of 5 T. This suggests that another paramagnetic phase, ζ-Fe_2N, is also present in small amounts, reflecting previous reports on these films [22],[23]. A moment of 0.18 μ_B per formula unit is measured at 5 T. The second film showed some anisotropy. The moment saturated to a value of 2.9 μ_B at 0.5 T with the field parallel

to the sample, and 2.9 μ_B at 1.7 T with the field perpendicular.

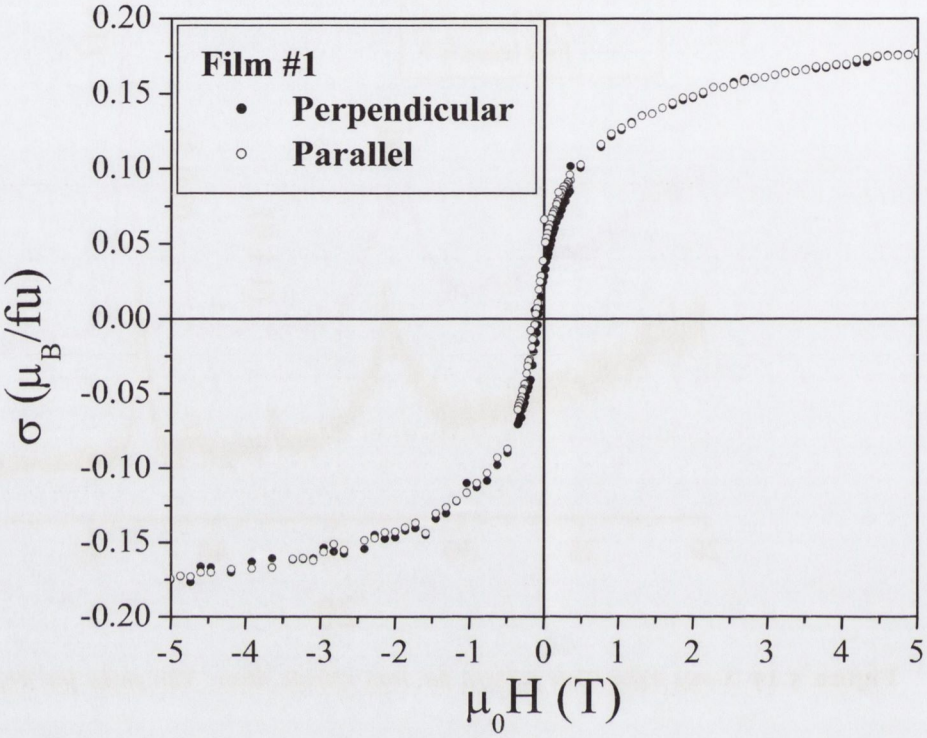

Figure 4.15 *Magnetisation loop of ε-$Fe_{2-3}N$, film #1, taken in a SQUID at 4.2 K.*

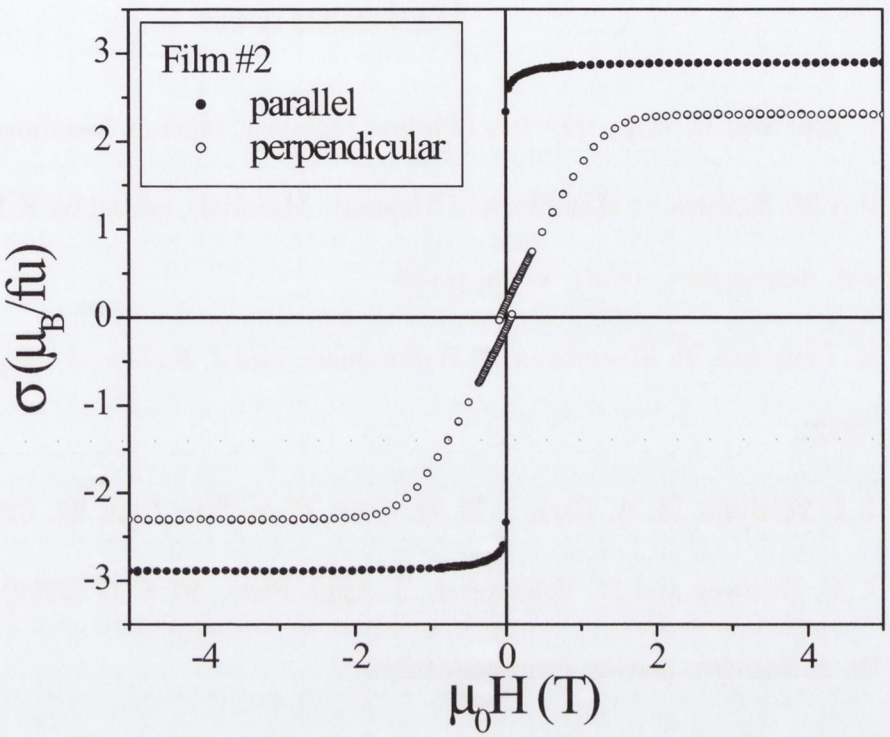

Figure 4.16 *Magnetisation loop of ε-$Fe_{2-3}N$, film #1, taken in a SQUID at 4.2 K.*

References

[1] J. Smit and H. Wijn, *Ferrites* (Philips Technical Library, Eindhoven, 1959).

[2] V.A.M. Brabers, in Handbook of Magnetic Materials, edited by K.H.J. Buschow (North Holland, Amsterdam, 1998), Vol 8, p.189.

[3] M. Pénicaud, B. Siberchicot, C.B. Sommers, and J. Kubler, J. Magn. Magn. Mat. **103**, 212 (1992).

[4] J. J. Versluijs, M. A. Bari, J. M. D. Coey, Phys. Rev. Lett. **87**, 026601 (2001).

[5] J. M. D. Coey and M. Venkatesan, J. Appl. Phys., **91** 8345 (2002).

[6] Dr. S. Sanvito, private communication.

[7] X. Guo, X. Chen, Z. Altounian, and J. O. Ström–Olsen , Phys. Rev. B **46**, 14578 (1992).

[8] J. B. Yang, K. Kamaraju, W. B. Yelon and W. J. James, Appl. Phys. Lett. **79**, 1846 (2001).

[9] F. Heusler, Verh. Dtsch. Phys. Ges. **5**, 219 (1903).

[10] C. Palmstrøm, MRS Bulletin **10,** 725 (2003).

[11] Y. Nishino, M. Kato and S. Asano, Phys. Rev. Lett. **79,** 1909 (1997).

[12] T. Block, C. Felser, G. Jakob, J. Ensling, B. Mühling, P. Guütlich, and R. J. Cava, J. Solid State Chem. **176,** 646 (2003).

[13] N. Auth, G. Jakob, T. Block and C. Felser, Phys. Rev. B **68,** 024403 (2003).

[14] S. Ishida, T. Masaki, S. Fujii, and S. Asano, Physica B **245**, 1 (1998).

[15] P. J. Brown, K. U. Neumann, P. J. Webster, and K. R. A. Ziebeck, J. Phys.: Condens. Matter **12**, 1827 (2000).

[16] K. H. Jack, Proc. Roy. Soc. A **195**, 34 (1948); K. H. Jack, Acta Cryst. **5**, 404 (1952).

[17] T. K. Kim and M. Takahashi, Appl. Phys. Lett. **20**, 492 (1972).

[18] J. M. D. Coey, K. O'Donnell., Q. Qinian, E. Touchais and K. H. Jack, J . Phys.: Condens. Matter **6,** L23 (1994).

[19] H. Jacobs, D. Rechenback, and U. Zachwieja, J. Alloys Comp. **227**, 10 (1995).

[20] Y. R. Jang, I. G. Kim, J. I. Lee, J. Magn. Magn. Mat. **263,** 366 (2003).

[21] D. C. Sun, E. Y. Jiang, H. Liu, S. L. Ming and C. Lin, J. Phys. D Appl. Phys. **28,** 4 (1995).

[22] H. M. Du, P. Wu, E. Y. Jiang, Z. Q. Li, C. Zhao, and H. L. Bai, J. Magn. Magn. Mat. **292**, 227 (2005).

[23] J. Q. Xiao and C. L.Chien, Appl. Phys. Lett. **64**, 384 (1994).

Chapter 5

Point Contact Measurements

5.1 Results

For point contact measurements, I-V curves were taken both in a field of 7 mT and without an applied field. The curves, often non-linear, were fitted to the following equation

$$I = GV + CV^3, \tag{1}$$

where G is the ohmic conductance of the sample at zero bias. The same behavior can be parameterized in terms of the height φ and width s of a rectangular tunnel barrier using the Simmons model [1]. The conductivity and the nonlinear coefficient can then be expressed as

$$G = \frac{3}{2sA}\left(\frac{e}{\hbar}\right)^2 (2m\varphi)^{1/2} \exp\left[-\left(\frac{4\pi s}{\hbar}\right)(2m\varphi)^{1/2}\right] \tag{2}$$

$$C = \frac{(\pi sm)^{\frac{3}{2}}}{(2\varphi)^{\frac{1}{2}}}\left(\frac{e}{\hbar}\right)^4 \exp\left[-\left(\frac{4\pi s}{\hbar}\right)(2m\varphi)^{1/2}\right] = \frac{Gs^2}{\varphi} \times const, \tag{3}$$

where A is the cross sectional area of the contact (see section 2.1.4). We can assume that for point contacts of a given material, the material composition of any barrier layer will be the same for different contacts. Thus the barrier height φ should not change, and the ratio C/G will give us an indication of the barrier thickness.

The magnetoresistance is calculated using

$$MR = 100\% \times \frac{G(H) - G(0)}{\max[G(H), G(0)]}, \tag{4}$$

where G(H) and G(0) are the conductances in an applied field and zero field respectively.

Note that with this definition the MR cannot exceed 100%, and it is positive when the resistance decreases in the applied field, as is usually the case. One difficulty with these experiments is that there is little control of the contact. When the measurement is repeated, a different contact is established so it is necessary to accumulate a great deal of data and view it statistically.

5.1.1 Magnetite

Magnetoresistance measurements were carried out on various point contacts of polycrystalline magnetite over a range of conductance values across the contact. A typical I-V curve is shown below (see fig. 5.1). Resistance was also measured as a function of field for a few contacts, an example of this is given in fig. 5.2.

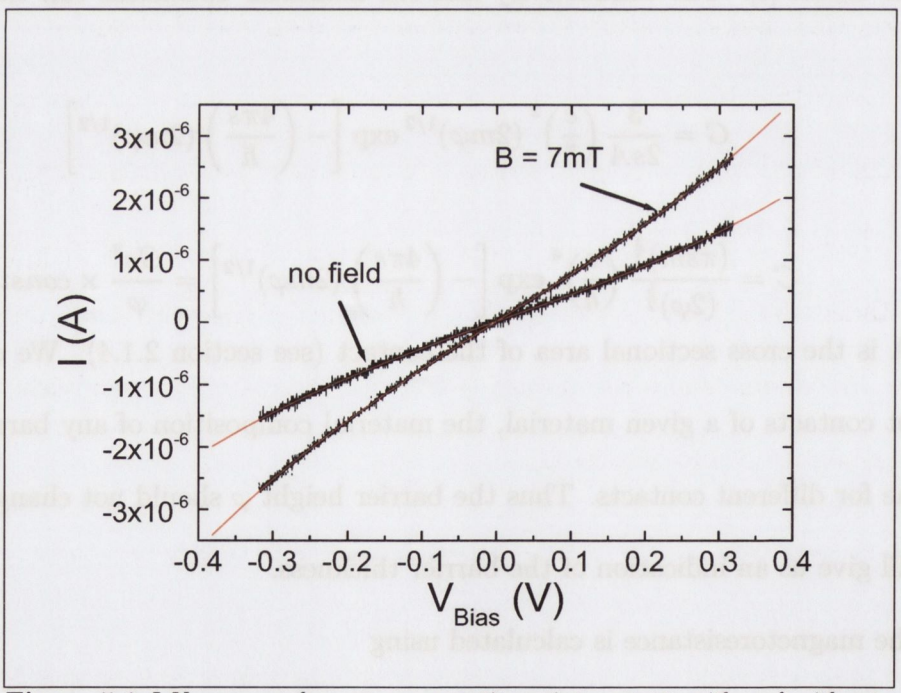

Figure 5.1 *I-V curves taken on a magnetite point contact, with and without an applied field, fitted to* $I = GV + CV^3$. *The conductance of this contact was 0.03* G_0, *and the calculated MR was 93%.*

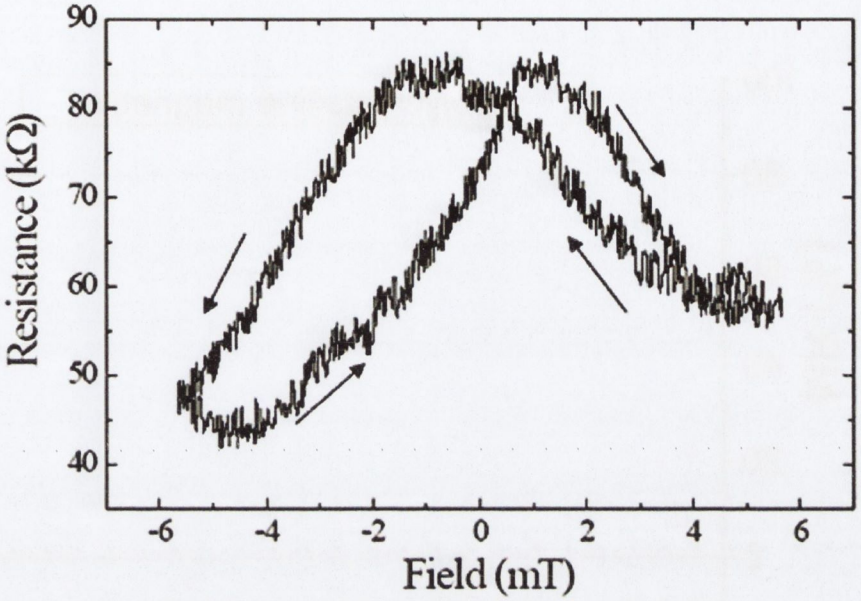

Figure 5.2 *Resistance against applied magnetic field for a magnetite point contact with conductance* $\approx 0.14G_0$.

Figure 5.3 shows a scatter plot of the magnetoresistance for various magnetite contacts. It can be seen that there is little magnetoresistance when $G > G_0$, the quantum of conductance $(12900\ \Omega)^{-1}$, but when $G < G_0$ the effect can exceed 80% (i.e. over 500% increase in conductivity). It is also evident that the magnetoresistance is almost always positive, i.e. the resistance almost always reduces in the presence of the field. Only one curve showed a negative MR value. These results are quite similar to previously published data for single crystal magnetite point contacts [2].

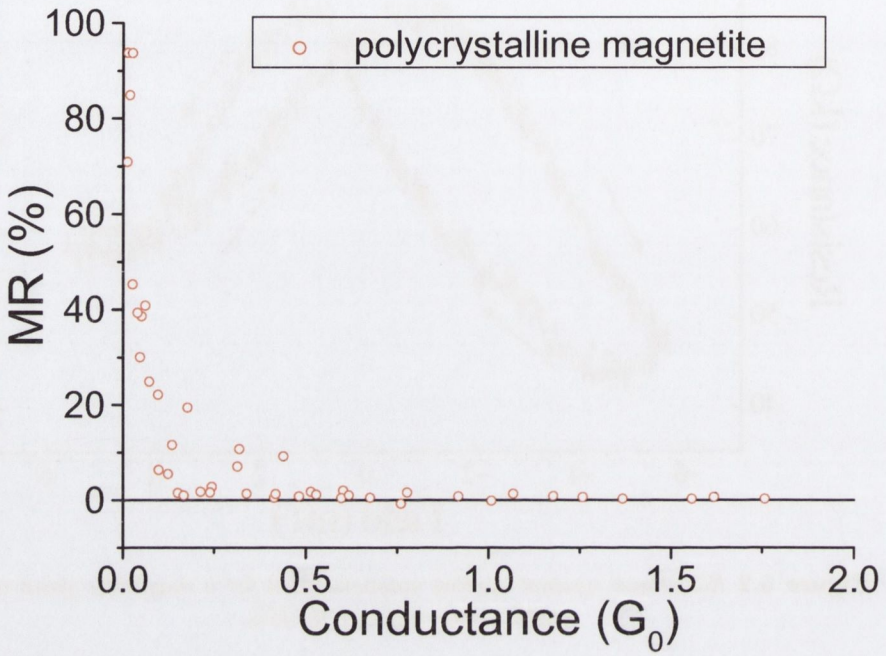

Figure 5.3 *Magnetoresistance as a function of conductance in zero field across a magnetite point contact. The applied field was 7 mT.*

In fitting the curves using (1), there is a clear inverse correlation between C/G and G; the less conducting the contact, the less linear the I-V curve (see fig. 5.4). This would suggest that when $G < G_0$, there is no direct metallic contact, and some sort of tunnel barrier is present. Quantised conductance measurements were also carried out on magnetite point contacts, but no steps in conduction were observed. This is not surprising considering the hopping conduction model used to describe electron transport in Fe_3O_4. The results obtained on point-contacts of magnetite have been published in the Journal of Applied Physics [3].

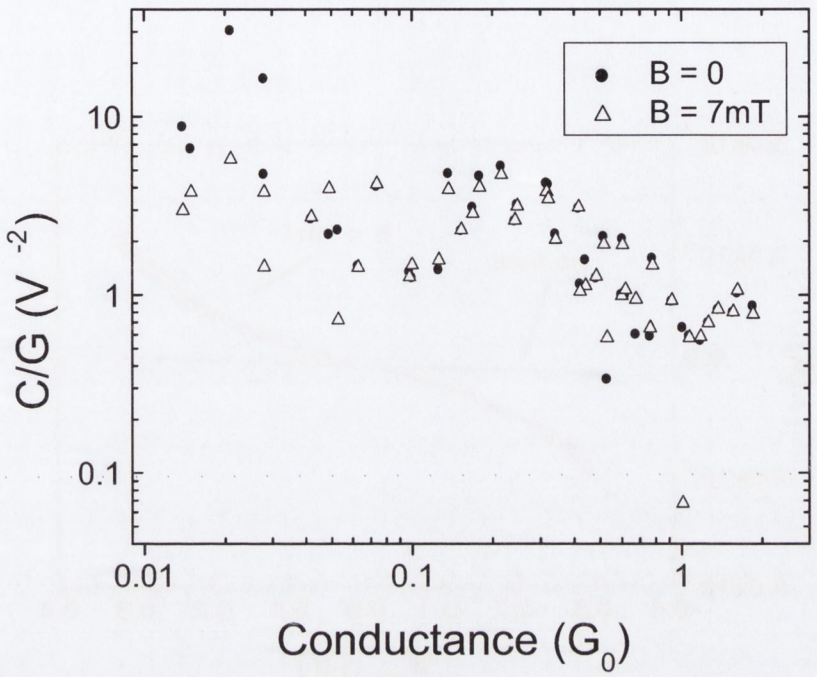

Figure 5.4 *Plot of C/G against conductance (normalised with respect to G_0) for magnetite point contacts, both with and without an applied field.*

5.1.2 Gold-plated Magnetite

In gold plated magnetite, values of magnetoresistance of up to 89% were recorded (see fig. 5.5). No significant negative MR was observed. Resistance was also measured as a function of field (fig. 5.6), showing a similar hysteresis to that observed in fig. 5.2. Once again non-linearity was clearly apparent in curves with low conductance. As in the case of uncoated magnetite, C/G rises sharply as the conductance drops (see fig 5.7) - however it seems to drop again for conductance values below $0.01G_0$. The magnitude of C/G was in general slightly lower than for uncoated magnetite. This is presumably due to a more metallic contact being formed by the gold layer.

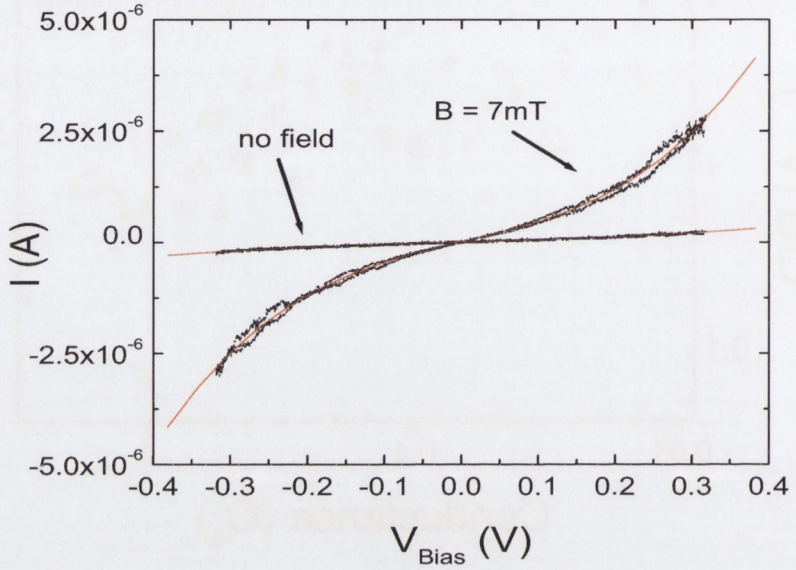

Figure 5.5 *I-V curves taken on a gold-plated magnetite point contact, with and without a field, fitted to* $I = GV + CV^3$. *The conductance of this contact was* $\approx 0.01G_0$, *and the calculated MR was 89%.*

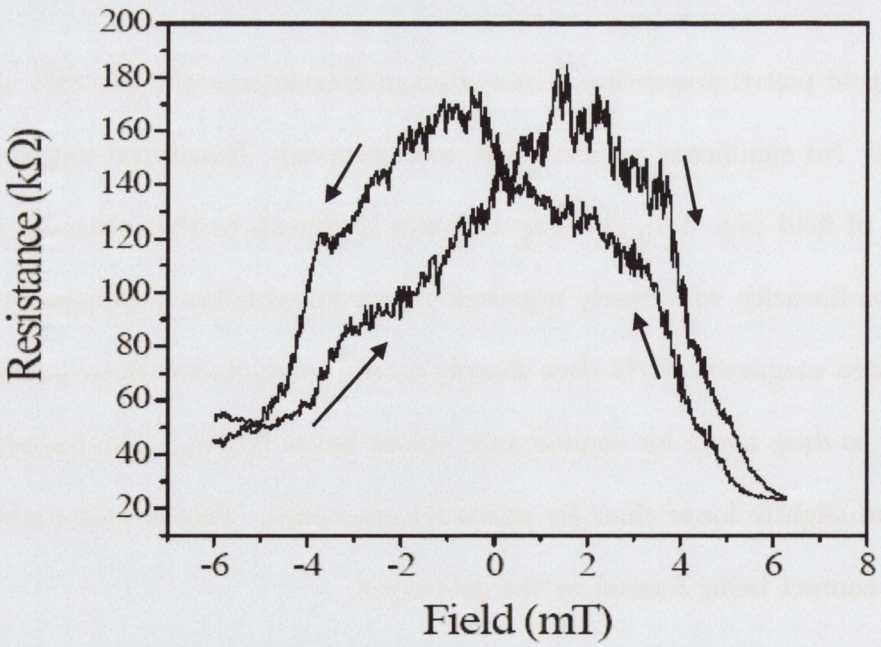

Figure 5.6 *Resistance against applied magnetic field for a gold-plated magnetite point contact with conductance* $\approx 0.08G_0$.

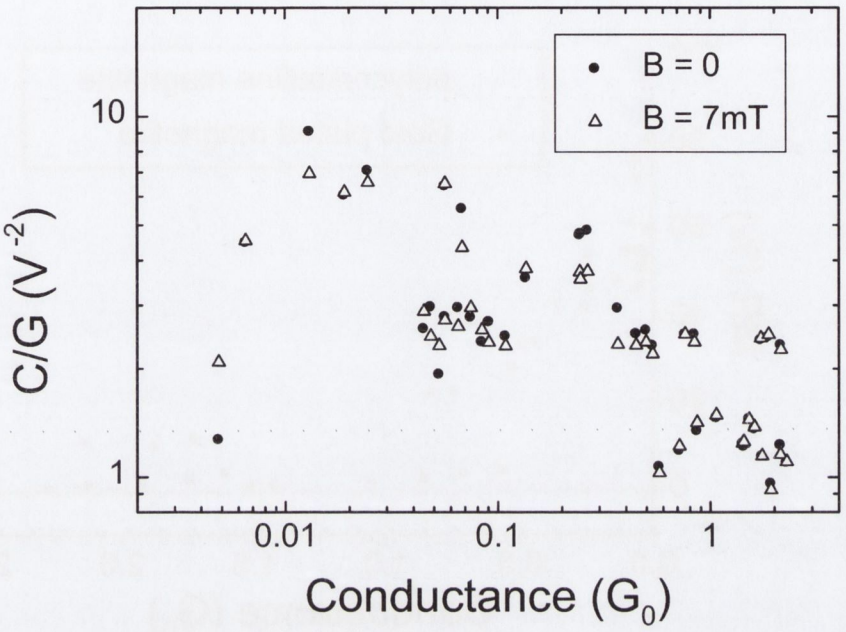

Figure 5.7 *C/G plotted against conductance for gold-plated magnetite point contacts, both with and without applied field (7 mT).*

Except for the smallest contacts, the magnetoresistance for gold-plated contacts gave generally higher values than for uncoated samples of equivalent conductance. A plot of magnetoresistance as a function of conductance is plotted along with those for uncoated magnetite (see fig 5.8) .

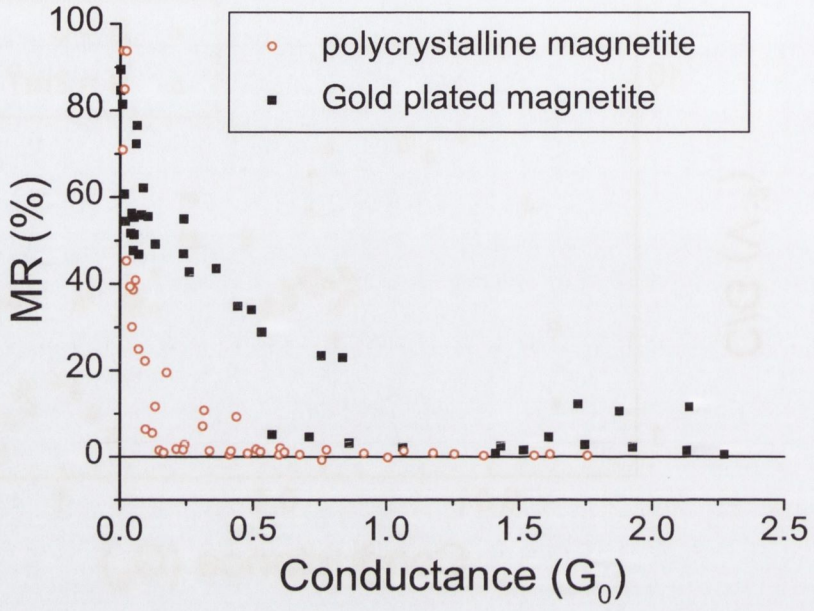

Figure 5.8 *Magnetoresistance as a function of conductance across gold-coated magnetite point contacts, shown with the same for polycrystalline magnetite point contacts. The applied field was 7 mT.*

Quantised conductance measurements were also performed on the gold-plated magnetite point contacts. No consistent quantization was observed, however an occasional contact did show steps in the conductance with multiples of G_0 (see fig 5.9), which are characteristic of gold nanocontacts.

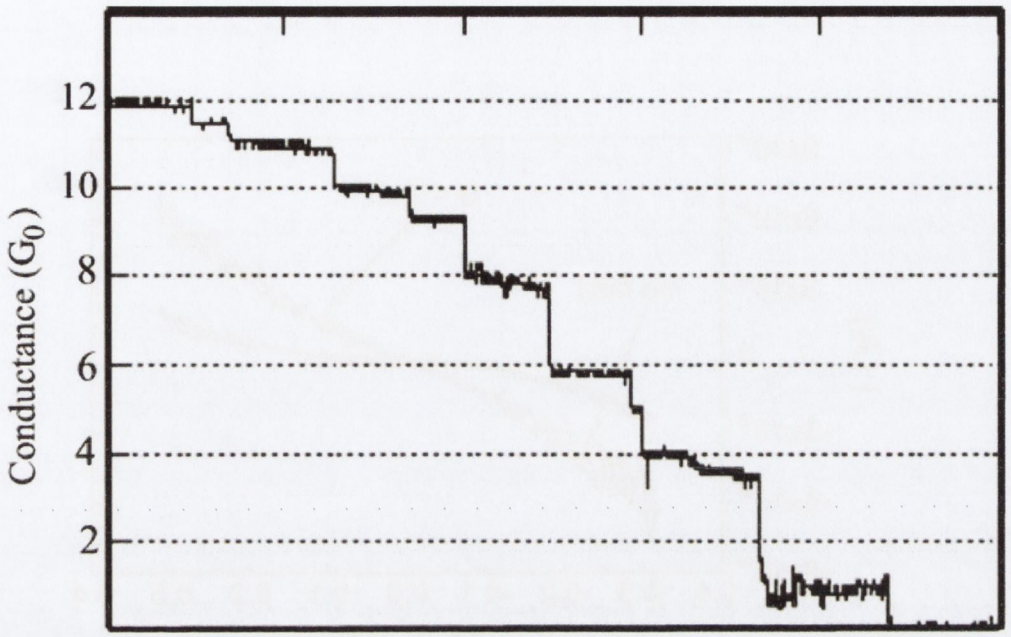

Figure 5.9 *Quantised conductance steps observed in a breaking contact of gold-plated magnetite.*

5.1.3 Gold/Magnetite

A contact was made between a magnetite crystal and a piece of gold so as to observe the field effects on what is essentially a nonmagnetic point contact. Both positive and negative values of magnetoresistance were recorded, with maximum values of 80% (see fig 5.10) and -99% (see fig 5.11) accordingly (note that for the definition of magnetoresistance used, the highest obtainable positive value is 100%). For low conductance contacts that showed negative MR, the curves were non-linear. However for those that showed positive MR, the curves were more linear. Switching behaviour was often found in the IV curves, with the conductance jumping back and forth between a low and a high value. Unfortunately point contacts between the substances were difficult to maintain for more than a few seconds, making IV measurements quite problematic.

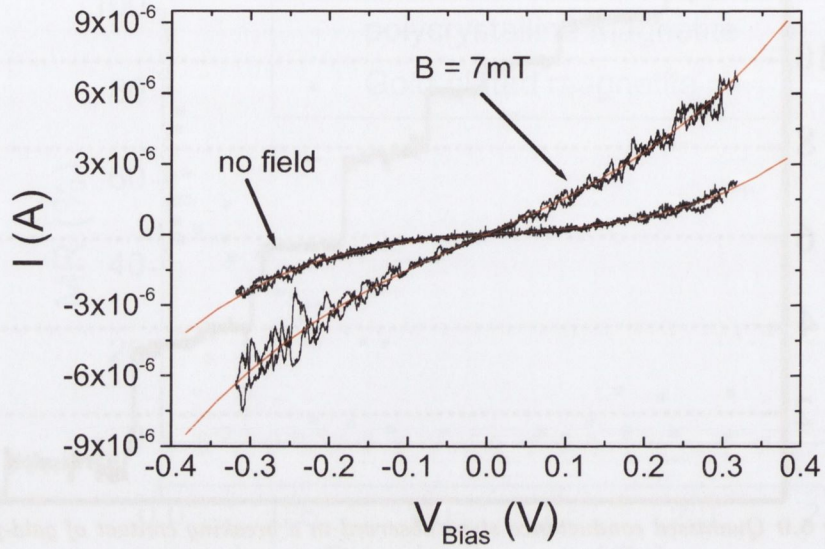

Figure 5.10 *I-V curves taken on a point contact consisting of magnetite against a piece of gold, with and without a field, fitted to* $I = GV + CV^3$. *The conductance of this contact was* $0.03G_0$, *and the calculated MR was 88%.*

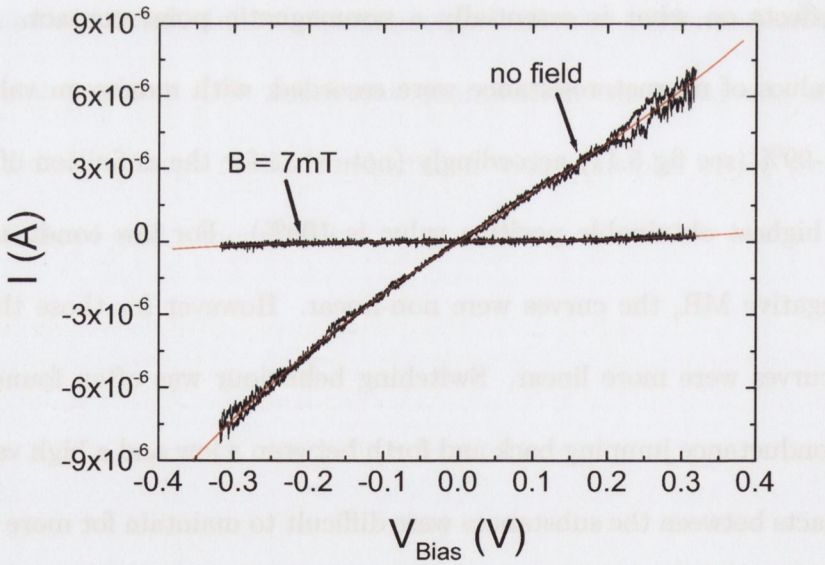

Figure 5.11 *I-V curves taken on a point contact consisting of magnetite against a piece of gold, with and without a field, fitted to* $I = GV + CV^3$. *The conductance of this contact was* $0.3G_0$, *and the calculated MR was -99%.*

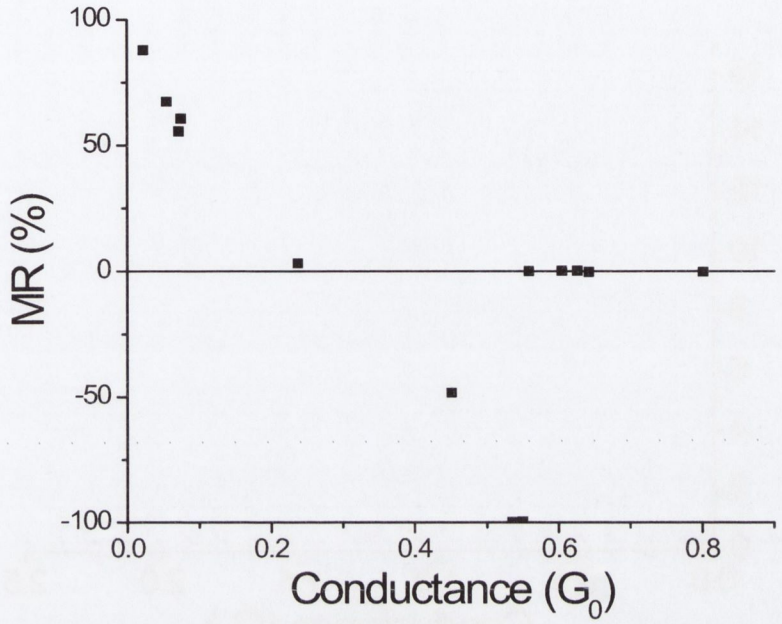

Figure 5.12 *Plot of MR obtained from point contacts obtained between a piece of gold and a magnetite crystallite. Both positive and negative values were observed.*

5.1.4 SFMO

In samples of single crystal SFMO, values of magnetoresistance of up to 15% were recorded for conductance values less than 0.1 G_0 across the contact (see fig. 5.13). No significant negative MR was recorded. Once again, curves were non-linear for low values of conductance (see fig 5.14), and C/G rises sharply as the conductance reduces (see fig 5.15). However the values of C/G are much smaller than those obtained for magnetite and gold-plated magnetite.

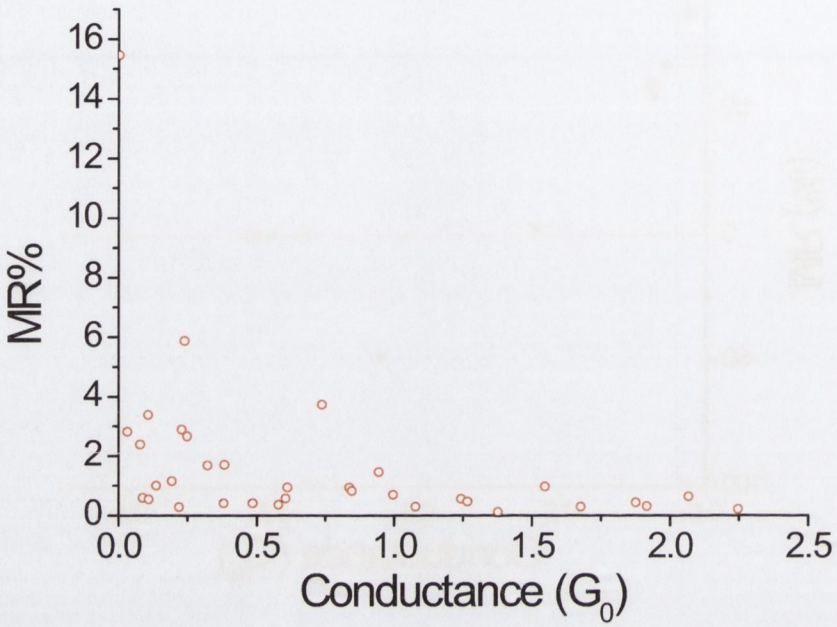

Figure 5.13 *Magnetoresistance as a function of conductance across SFMO point contacts. The applied field was 7 mT.*

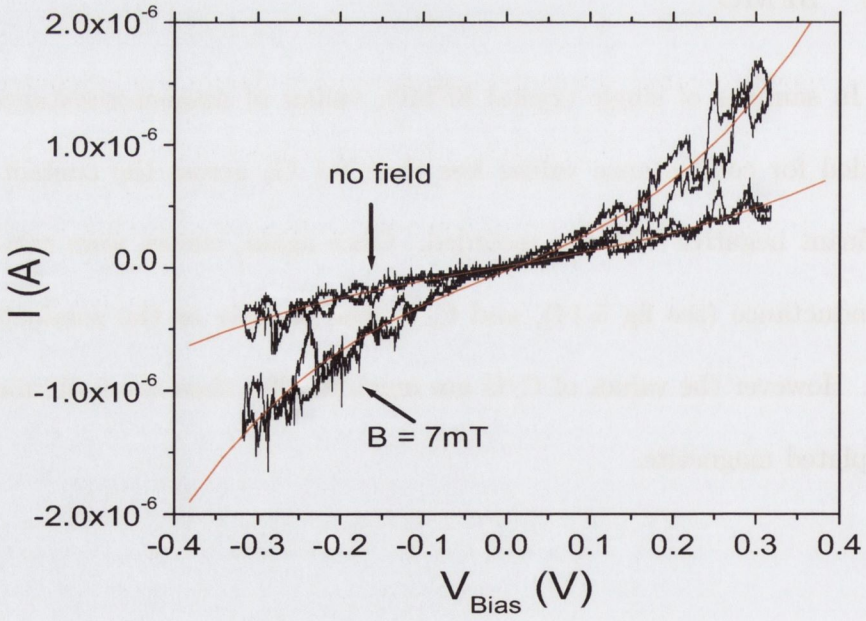

Figure 5.14 *I-V curves obtained across a point contact of SFMO. These curves are for a contact with conductance <0.01 G_0 and show magnetoresistance of 15%.*

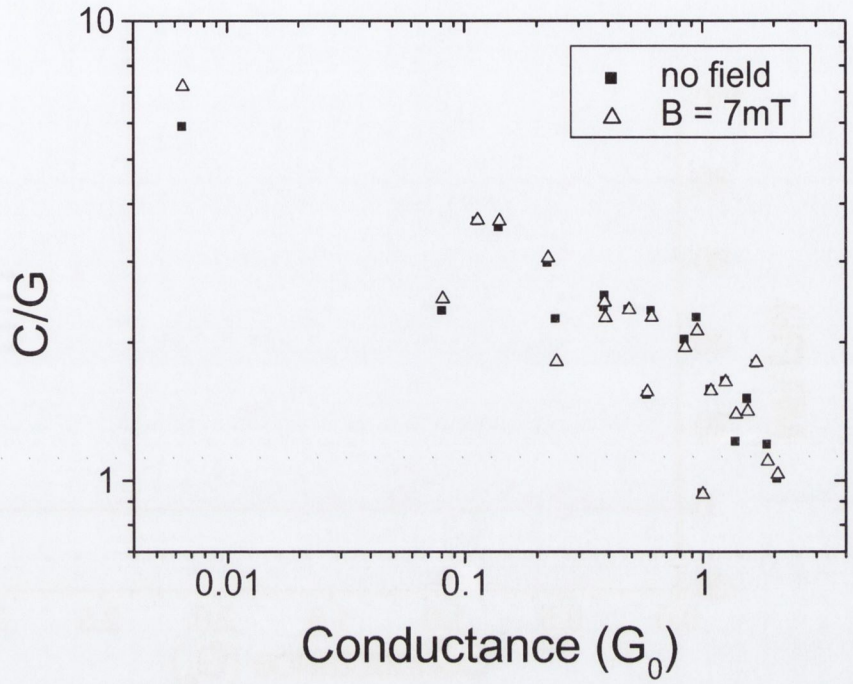

Figure 5.15 *C/G plotted against conductance for single crystal SFMO point contacts, both with and without an applied field (7 mT).*

5.1.5 MnBi

Magnetoresistance measurements were carried out on point contacts consisting of MnBi crystallites. Quite high magnetoresistance was observed even in relatively highly conductive contacts (see fig 5.16) . However some contacts showed no magnetoresistance at all, even at very low conductances. One contact showed negative magnetoresistance (i.e. resistance increased in field).

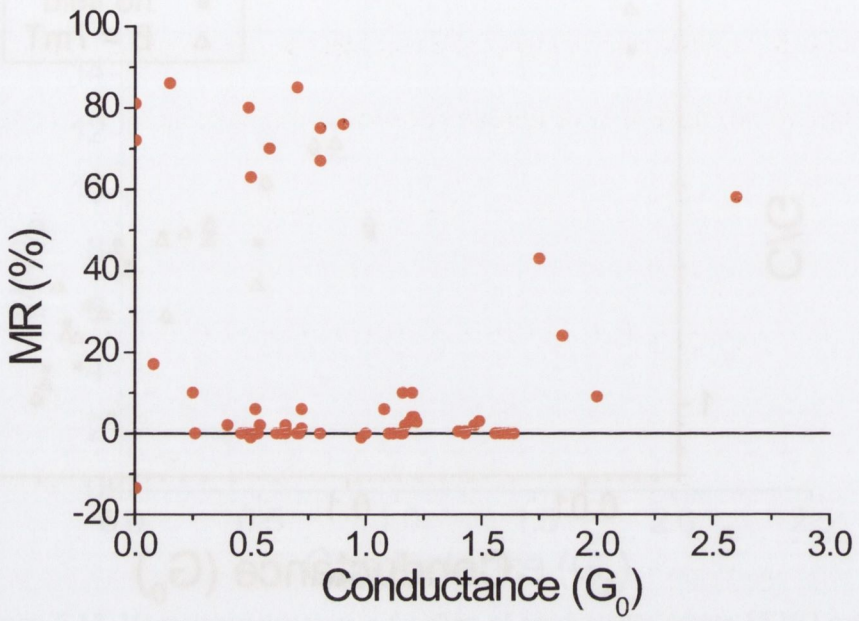

Figure 5.16 *Magnetoresistance as a function of conductance across MnBi point contacts. The applied field was 7 mT. One negative value of MR was obtained.*

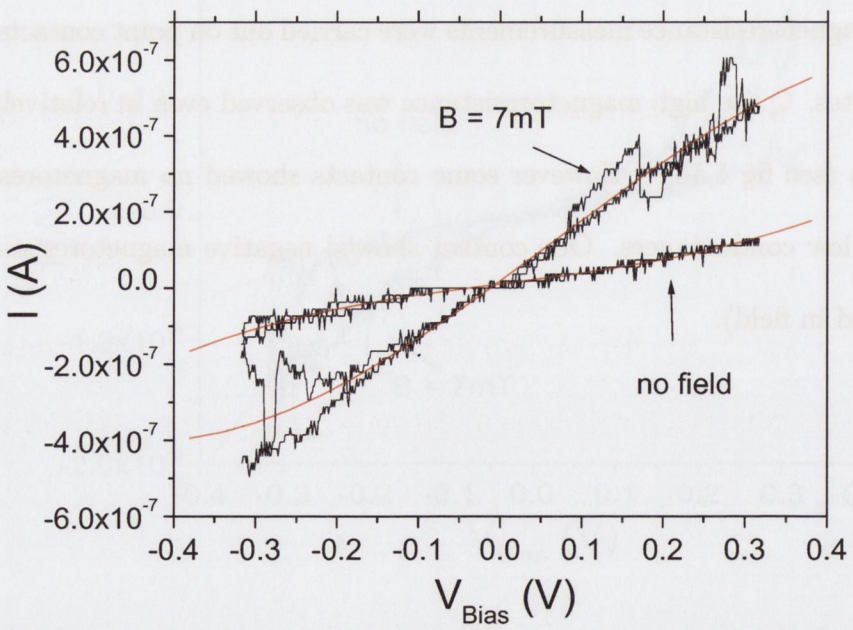

Figure 5.17 *I-V curves obtained on an MnBi point contact. 72% magnetoresistance is observed here. The conductance of this contact was $\approx 0.003\ G_0$ in zero field.*

The IV curves showed some nonlinearity (see fig 5.17), but were certainly more linear than those obtained from SFMO and magnetite point contacts. Switching behaviour was often found in the I-V curves, with the conductance jumping back and forth between a low and a high value. This is presumably caused by rearrangement of the contact size.

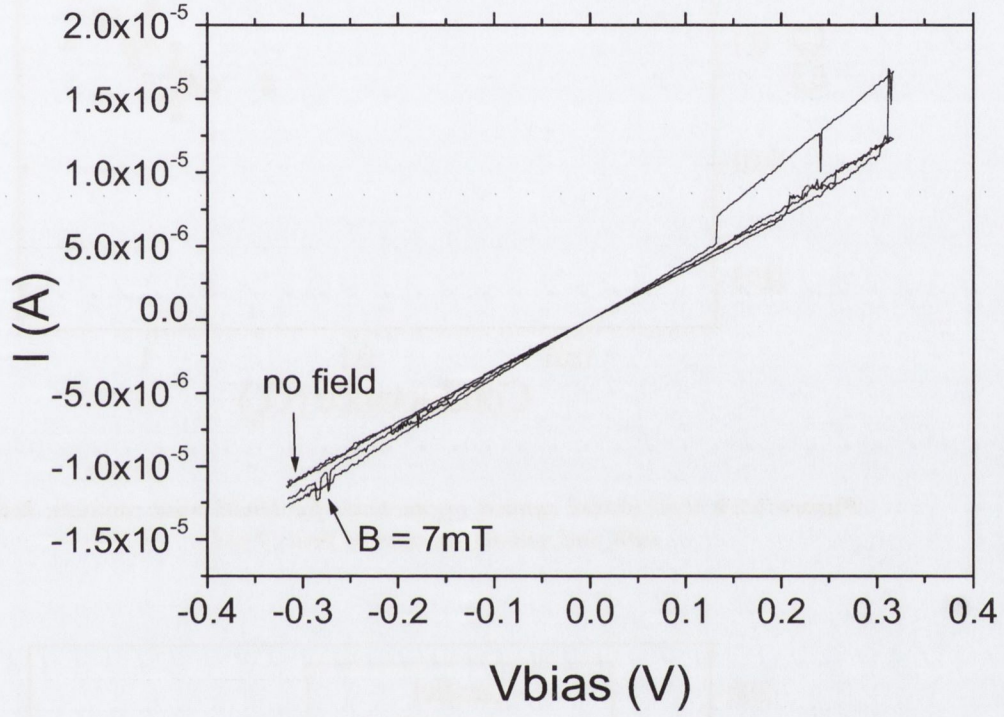

Figure 5.18 *I-V curves obtained on an MnBi point contact. The two curves almost overlap; the magnetoresistance is negligible. Some switching is seen in the curve in field. The conductance here was* $\approx 0.45G_0$.

The values of C/G are much smaller than those obtained from the other materials (see fig 5.19), reflecting the relative linearity of the curves. Unlike the case with magnetite and SFMO point contacts, the C/G values do not seem to increase with decreasing conductance.

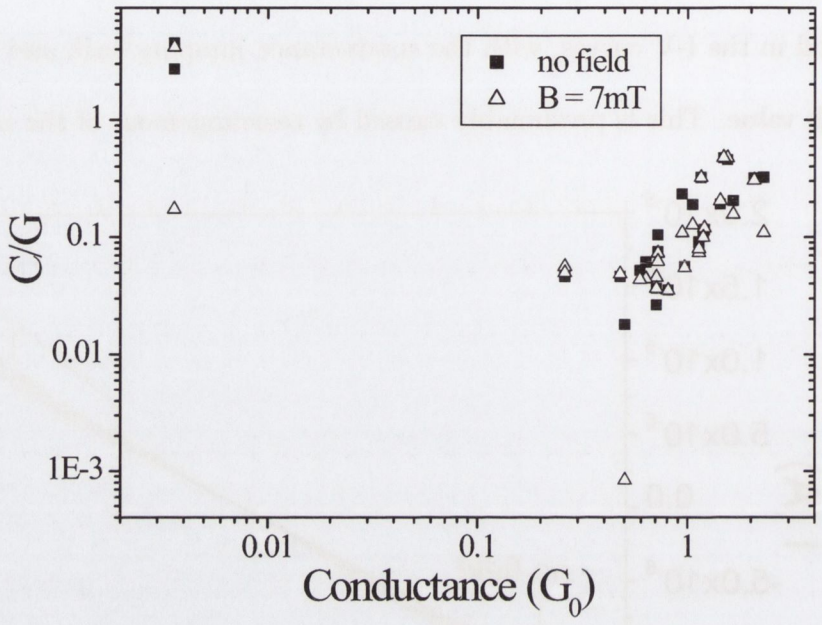

Figure 5.19 *C/G plotted against conductance for MnBi point contacts, both with and without an applied field (7 mT).*

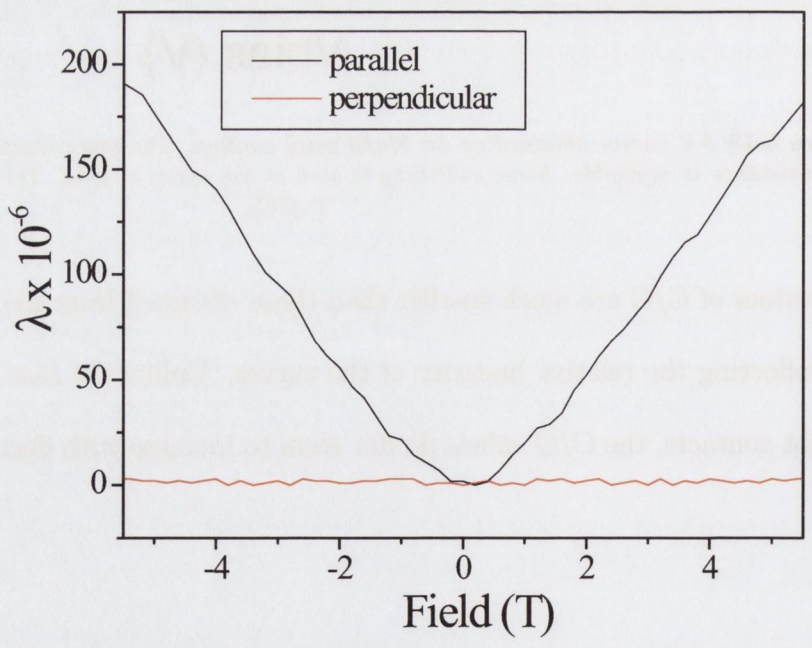

Figure 5.20 *Parallel and perpendicular components of magnetostriction in MnBi as a function of applied field, where λ is the relative change in length.*

Magnetostriction was also directly measured (see fig 5.20). A large magnetostriction was observed parallel to the field. This was unsaturated at 5 T, where the relative length change λ was close to 190 $\times 10^{-6}$. The value obtained for λ at 7 mT was within the noise level of the measurement i.e. a relative length change of less than 0.3×10^{-6}. No significant magnetostriction was observed perpendicular to field. The results for MnBi point contacts were published in the Journal of Magnetism and Magnetic Materials [4]

5.1.6 $Co_2Cr_{0.4}Fe_{0.6}Al$

Point contacts were made from $Co_2Cr_{0.4}Fe_{0.6}Al$ crystallites, and I-V curves were taken both with and without an applied field (see fig 5.21). A scatter plot of around 40 measurements is shown in fig. 5.22. Points were taken both in vacuum and under ambient pressure. Carrying out the measurements under vacuum would presumably remove any water vapour that could condense at the point contact, however a comparison between the two data sets shows no significant differences. Any magnetoresistance observed was generally positive, however five contacts did show negative MR. The MR values were typically 10 - 40% when $G < G_0$; in a few instances it was as high as 80%.

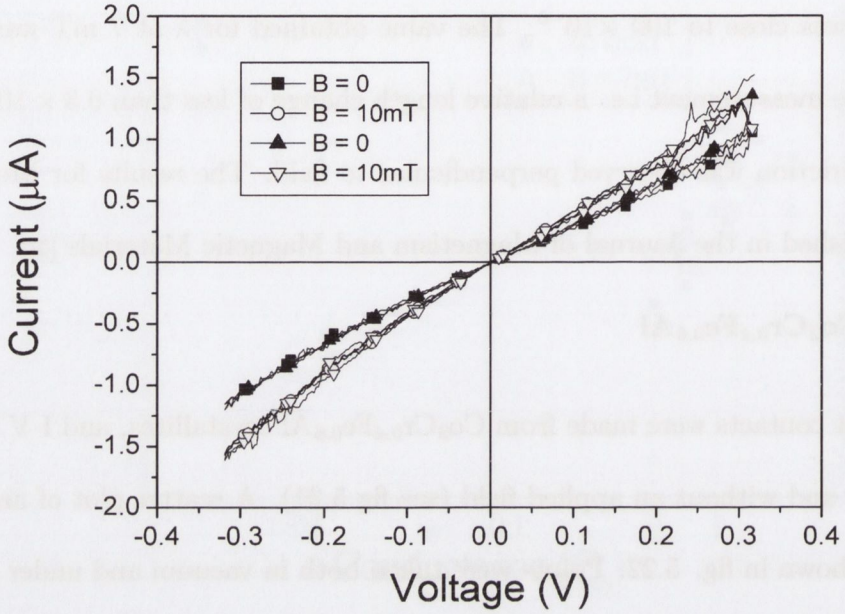

Figure 5.21 *Typical magnetoresistance data for a $Co_2Cr_{0.4}Fe_{0.6}Al$ point contact. The applied field is 10 mT.*

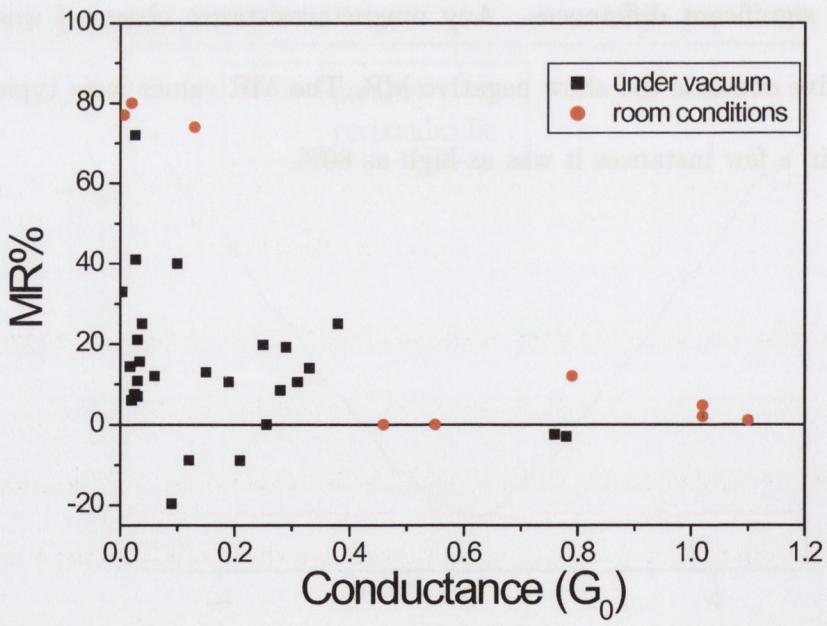

Figure 5.22 *Scatter plot showing magnetoresistance measured in 36 $Co_2Cr_{0.4}Fe_{0.6}Al$ point contacts at room temperature.*

Magnetostriction measurements were also carried out on a piece of $Co_2Cr_{0.4}Fe_{0.6}Al$ (see

fig 5.23). The magnetostriction is small, saturating at 5×10^{-6}, but there is no discernible length change in fields less than 100 mT. This is because the initial magnetisation process involves domain wall motion, not magnetisation rotation. Movement of a 180° wall does not influence the magnetostrictive strain.

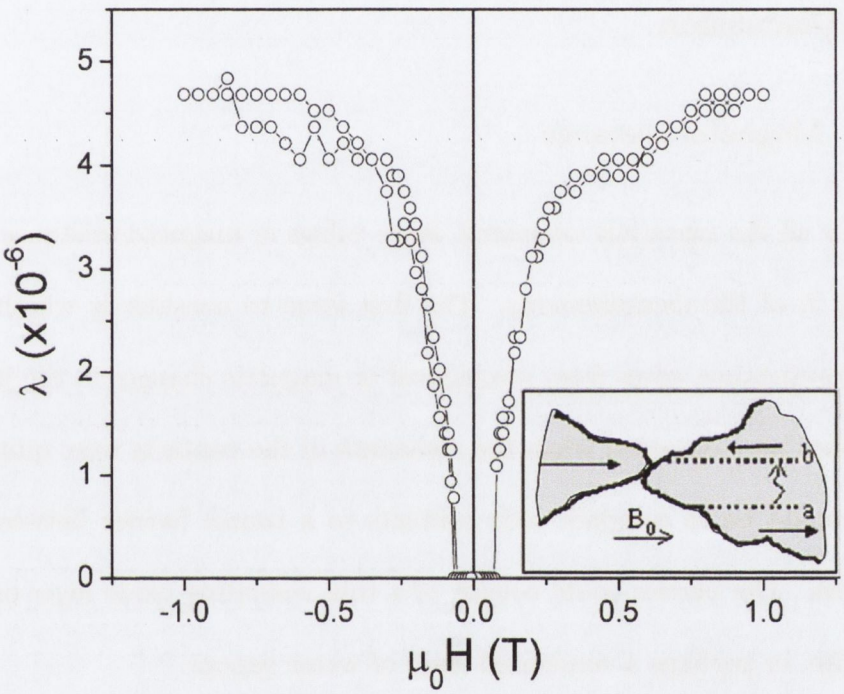

Figure 5.23 *Magnetostriction measurement carried out on a piece of $Co_2Cr_{0.6}Fe_{0.4}Al$. The insert shows a possible domain wall movement from $a \rightarrow b$ which produces maximum magnetoresistance but no magnetostrictive strain.*

Following previous reported results [5], MR measurements were carried out on pressed powders of $Co_2Cr_{0.4}Fe_{0.6}Al$. Powders were created by crushing the powders in a steel percussion grinder, followed by further grinding in a standard marble mortar and pestle. For PMR measurements, the powder was pressed into disks of diameter 5 mm and thickness ≈1 mm using cold compression under pressures of up to 10 MPa. In some cases, the powder was mixed with various amounts of Teflon powder to bring the mixture closer to the percolation threshold. The powder magnetoresistance was measured at room temperature for

pressed powders and metal/Teflon composites with resistances ranging from 50 mΩ to 10 kΩ, and a field of up to 2 T was applied. However in no case were we able to measure PMR in excess of 1 %. The results obtained for $Co_2Cr_{0.4}Fe_{0.6}Al$ were published in Solid State Communications [6].

5.2 Discussion

5.2.1 Magnetoresistance

For all the materials examined, large values of magnetoresistance were obtained on at least 50 % of the measurements. The first issue to consider is whether the point-contact magnetoresistance arises from mechanical or magnetic changes in the junction. The highest MR values were obtained when the resistance of the contacts were quite high. One possible model would be to compare such contacts to a tunnel barrier between two ferromagnetic electrodes. The barrier could consist of a thin insulating oxide layer on the surface of each crystallite, or perhaps a condensed layer of water vapour.

Let us first suppose that there is no direct local magnetic effect on the conductance across the contact, but only a magnetomechanical effect on the barrier. It is then expected that there will be a decrease in the barrier thickness, and hence C/G, upon application of a magnetic field.

However this cannot be the case for all of the contacts showing MR; fig 5.24 shows the C/G in an applied field divided by C/G in zero field, plotted against the conductance of the contact in zero field. A value of less than one for this ratio means that the thickness of any tunnel barrier is decreased in the presence of a field. For all but the most highly resistive contacts, the value of this ratio is close to one, with many contacts having a ratio greater

than one. This suggests that the magnetoresistance for these contacts is related to the spin-polarized transmission probability as opposed to any mechanical change in the contact. Also the hysteresis observed in resistance as a function of applied field for magnetite [see fig. 5.2] supports the theory that the MR must be related to the magnetisation processes of the crystallites.

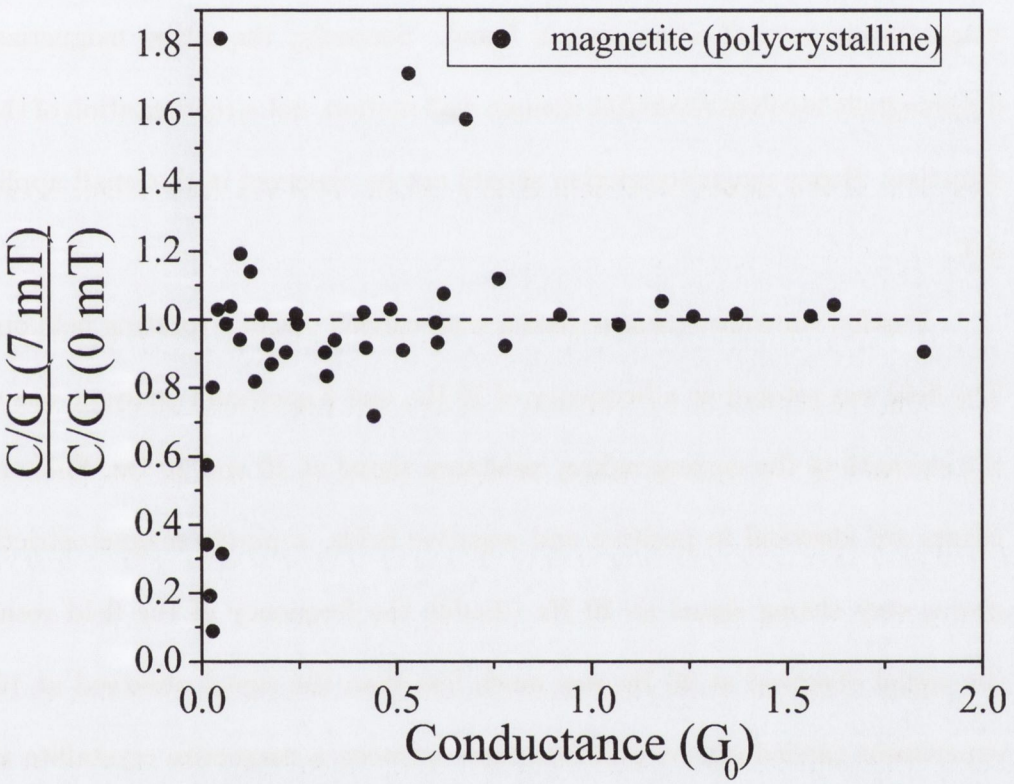

Figure 5.24 C/G in an applied field divided by C/G in zero field, plotted against the conductance of the contact in zero field for polycrystalline magnetite point contacts. C/G gives an indication of tunnel barrier thickness. When C/G is independent of field (dashed line) the barrier remains unchanged and any MR is a magnetic rather than a mechanical effect.

The possibility of magnetostriction, which might be expected to influence the barrier thickness, or indeed contact area, was investigated in several ways. The experiments with point contacts between polycrystalline magnetite and a gold electrode established that magnetoresistance of either sign could be observed [figs 5.10 & 5.11]. In that case, the magnetoresistance was as often negative as positive and the average was near zero. Since gold

is obviously non-magnetic, the MR observed here was more than likely due to magnetomechanical effects, most probably magnetostriction.

However we discount magnetostriction as the major reason for the magnetoresistance of the point contacts between magnetic materials for several reasons. Firstly, the observed magnetoresistance is almost always positive, unlike in the case of magnetite and gold where magnetoresistance of either sign is found. Secondly, the initial magnetization process in ferromagnets involves reversible domain wall motion, not a reorientation of the magnetization direction. Hence magnetostriction should not be observed in the small applied fields of 7-10 mT.

Finally, resistance measurements were carried out in a rotating field on point contacts. The field was rotated at a frequency of 10 Hz, and a spectrum analyzer was used to examine the strength of the corresponding resistance signal at 10 and 20 Hz. Since magnetostrictive effects are identical in positive and negative fields, a purely magnetostrictive effect would give a very strong signal at 20 Hz (double the frequency of the field rotation). However the signal observed at 20 Hz was much less than the signal observed at 10 Hz. A similar experiment carried out on point contacts between a magnetite crystallite and a gold piece gave the opposite result, with a much stronger signal observed at 20 Hz.

Another possible magnetomechanical effect arises from the dipole-dipole interaction between the crystallites [7]. The dipolar force between the two crystallites is of order $\mu_0 H_d M d^2$, where d is the crystallite diameter, and the field H_d produced by one crystallite on the other is approximately $(1/4\pi)M$. The strain ε produced by this force is $\mu_0 M^2/4\pi Y$, where Y is Young's modulus. Taking Y as 2×10^{11} Nm^{-2}, and $M = 400$ kAm^{-1} (the saturation magnetization for magnetite) gives $\varepsilon = 8 \times 10^{-8}$. Since $d \approx 10^{-4}$ m for our magnetite crys-

tallites, the change in size of the gap due to dipolar forces is at most 0.01 nm, and therefore negligible.

Let us now look at possible magnetic effects on the conductance across a point contact. Two possible magnetization processes, both involving domain wall movement, that can give rise to large magnetoresistance are illustrated in figure 5.25. In one case, a domain wall at the contact is pushed into an adjacent crystallite. In the other case, a wall present in one crystallite is swept across the contact.

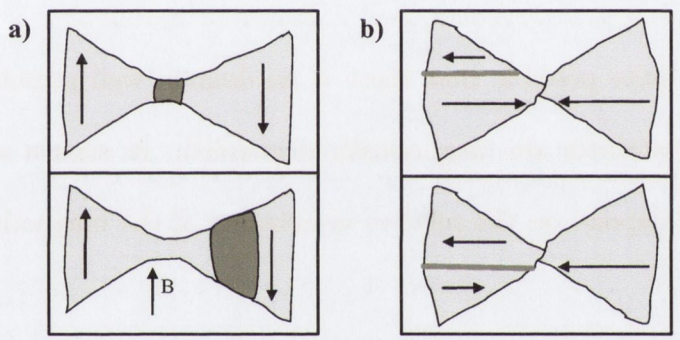

Figure 5.25 Two magnetization processes that can give rise to a large magnetoresistance. a) a domain wall at the contact is pushed into an adjacent crystallite. b) a wall present in one crystallite is swept across the contact.

In the more conducting point contacts with no gold plating it is expected that exchange coupling propagates across the contact (gold acts as an exchange barrier). A domain wall is likely to form there, as it is well known that domain walls tend to become trapped at the narrowest part of a nanoconstriction [8], [9]. As discussed in section 2.1.3, a domain wall at a narrow point contact will also be quite narrow, of the order of the actual width of the contact. Such narrow domain walls would have a very large resistance associated with them, as a polarised spin current would experience fewer spin flips before entering the unaligned region. This would also explain why MR increases sharply as the conductance (and thus the size) of the contact decreases.

The position of the domain wall will be modified by the applied field. As it is pushed into a wider area, the domain wall width would increase (see fig 5.25a), and the resistance associated with it would reduce. It is also possible that the domain wall could be pushed away from the contact altogether, meaning that the current would no longer have to pass through it (see fig 5.25b). Any change in the resistance caused by the field is reversible, changing to its original value once the applied field is switched off. This indicates that if there is a domain wall at the contact, it returns to its original position when the field is removed.

It is also quite possible that there is no domain wall present at the interface at all, i.e. the two crystallites are magnetically decoupled. In such a scenario the transmission probability will depend on the relative orientation of the magnetisation of the crystallites, $\theta_{1,2}$, i.e.

$$T \propto \cos^2(\frac{\theta_{1,2}}{2}). \tag{5}$$

As a field is applied, the magnetisation directions would rotate in the direction of the applied field, the transmission probability would increase and the resistance would reduce. This would explain why large magnetoresistance is only observed when $G < G_0$ - eliminating direct metallic contact would reduce the exchange coupling at the interface and ensure a sharp change of magnetisation direction from one crystallite to the next. If there is exchange coupling, a domain wall tends to form between the crystallites, and the magnetic interface is diffuse. This would increase the likelihood of spin-scattering events for the electrons, and the effect of magnetisation alignment between the two crystallite on the resistance would be less pronounced.

The maximum values of MR obtained for magnetite and gold-plated magnetite respec-

tively are 93 % and 89 %. According to Jullière [10], MR is related to the polarisation by equation (6), chapter 1. This gives us approximate polarisation values of 0.93 and 0.89 respectively for contacts of magnetite and gold plated magnetite which showed the highest MR. It is somewhat surprising that, in the case of gold-plated magnetite, the gold layer does not spin-scatter the electrons. However it is quite possible, especially for the more highly resistive contacts, that the act of forcing the crystallites together has removed the gold coating at the actual point contact.

In SFMO, the observed magnetoresistance was not as high. This may be due to the presence of defects in the crystal structure, such as antiphase boundaries and antisite defects, which would allow spin-flip scattering to take place, reducing the spin polarisation of the current. Such defects are common in Fe-Mo based double perovskite crystals [11]. Using the Jullière formula, a spin polarisation value of 0.11 is obtained for the most highly resistive SFMO contact.

Many of the curves obtained from MnBi point contacts show no magnetoresistance even at very low conductances. This is most likely due to the high degree of phase segregation in the sample. If we accept the suggested percentage of MnBi in the sample i.e. 75%, the probability of both contacts consisting of MnBi becomes $\approx$ 56%. Even if both contacts are MnBi, we are not assured that a domain wall will be trapped at the constriction. The highest MR obtained in MnBi point contacts was 86%, giving a spin polarisation of 0.87.

The magnetisation measured for $Co_2(Cr_{0.4}Fe_{0.6})Al$ at room temperature is around 90% of its value at 5 K. If we assume that the polarisation scales with temperature in a similar way we can thus presume an upper limit on the spin polarisation of 90%. In point contacts of this material, it is seen that the magnetoresistance can be as high as 80%. We deduce

from the Jullière formula that the spin polarisation is 81% for these contacts. Otherwise, taking a more typical value of 25% for the magnetoresistance, we get P $\approx$ 38 % at room temperature.

5.2.2 Non-linearity of I-V curves

Almost all of the I-V curves taken on point contacts show some degree of non-linearity. The relationship between C and G shows us that the I-V curves become less linear as the resistance across the point contact increases. The most obvious explanation for this is the presence of a tunnel barrier, with shape of the curves depending on the height and thickness of the barrier according to the Simmons model [see section 2.1.4].

The crystal interface is also likely to contain a disordered region with impurities and defects, which could act like a barrier containing localised states. As the potential across the barrier increases, more localised stated become involved in the tunnelling process and the resistance reduces.

The I-V curves for MnBi point contacts appear more linear than those obtained for other materials [see fig. 5.19 as opposed to figs. 5.4, 5.15]. One possible reason for this is that any secondary phases in the substance would still be likely to be quite metallic and thus highly conducting. Thus the main source of tunnelling would be across the grain boundary, and the tunnel barrier effect described above would be suppressed.

It has been speculated elsewhere that non-linearity in point contact I-V's may be due to domain wall movement [12]. In this model spin pressure acts on the domain wall at the contact, causing it to move into a region with greater cross section. According to Bruno, this would mean that the width of the domain wall would expand, reducing the resistance across it. This would be similar to the magnetic field effect on a domain wall as shown in fig. 5.25a.

It has been shown on many occasions that domain walls can be moved using spin-polarised currents (eg.[13],[14]), and current densities of the order of 10^6 A/cm^2 are typically reported as being necessary for this movement. If we take a nanocontact with an area 10 nm $\times$ 10 nm, this means a current of the order of 1 μA should be sufficient to move a domain wall.

However one problem with this model is that once the domain wall is fully removed from the constriction, its width, and therefore resistance, should no longer depend on its position. Thus we should see the non-linearity disappear at higher currents. Also due to the random nature of the point contacts, it is unlikely that the aspect ratio of the crystallites would be equal either side of the contact. Thus we should expect the change in domain wall width, and thus resistance, to vary depending on current direction. However no asymmetry has observed in the I-V curves.

References

[1] J. G. Simmons and G. J. Unterkofler, J. Appl. Phys. **34** 1828 (1963).

[2] J. J. Versluijs, M. A. Bari, J. M. D. Coey, Phys. Rev. Lett. **87**, 026601 (2001).

[3] O. Céspedes, E. Clifford, and J. M. D. Coey, J. Appl. Phys. **97**, 064305 (2005).

[4] E. Clifford, M.Venkatesan, and J. M. D. Coey, J. Magn. Magn. Mat. **272-276,** 1614 (2004).

[5] T. Block, C. Felser, G. Jakob, J. Ensling, B. Mühling, P. Guütlich, and R. J. Cava, J. Solid State Chem. **176,** 646 (2003).

[6] E. Clifford, M. Venkatesan, R. Gunning, and J. M. D. Coey, Solid State Comm. **131,** 61 (2004).

[7] H. Bourdonnay, J. Phys. (Paris), Colloq. **32**, C1-1182 (1971).

[8] I. V. Roshchin, J. Yu, A. D. Kent, G. W. Stupian, and M. S. Leung, IEEE Trans. Mag., **37**, 2101 (2001).

[9] J. D. Burton, A. Kashyap, M. Y. Zhuravlev, R. Skomski, E. Y. Tsymbal, and S. S. Jaswal, Appl. Phys. Lett. **85,** 251 (2004).

[10] M. Jullière, Phys. Lett. A, **54,** 225 (1975).

[11] J. M. Greneche, M. Venkatesan, M. Grafoute, A. Douvalis, R. Surynarayan, and J. M. D. Coey, Phys. Rev. B **63,** 174403 (2001).

[12] J. J. Versluijs, M. A. Bari, and J. M. D. Coey, Phys. Rev. Lett. **87,** 026601 (2001).

[13] J. Grollier, D. Lacour, V. Cros, A. Hamzic, A. Vaures, A. Fert, D. Adam, and G. Faini, J. Appl. Phys **92**, 4825 (2002).

[14] T. Kimura, Y. Otani, K. Tsukagoshi, and Y. Aoyagi, J. Appl. Phys **94**, 7947 (2003).

Chapter 6

Andreev Reflection Measurements

6.1 Results

The PCAR curves obtained were fitted using a procedure based on the BTK model [1] written in Mathcad (see Appendix I). Data is fitted using the variable parameters, Δ, P, and Z, where Δ is the superconducting gap for the superconductor, P is the spin polarisation and Z is the barrier coefficient.

6.1.1 Niobium Tip

PCAR measurements were taken on materials by pressing a sharpened niobium tip against the material. The contact size was controlled using a piezo-actuator, as described in section 3.5.1. The Niobium wires showed a superconducting transition at 9.2 K.

6.1.1.1 Copper

Copper is a highly conductive non-magnetic metal and was used to test and compare the different measurement techniques. A sharpened niobium wire was pressed against a mechanically polished piece of copper (99.99% pure) and data was taken at both 4.2 K and 2 K. Curves showed a near doubling of the conductance at zero bias voltage. A typical curve is shown in fig 6.1. A value of 0.08 was used for Z in this fit.

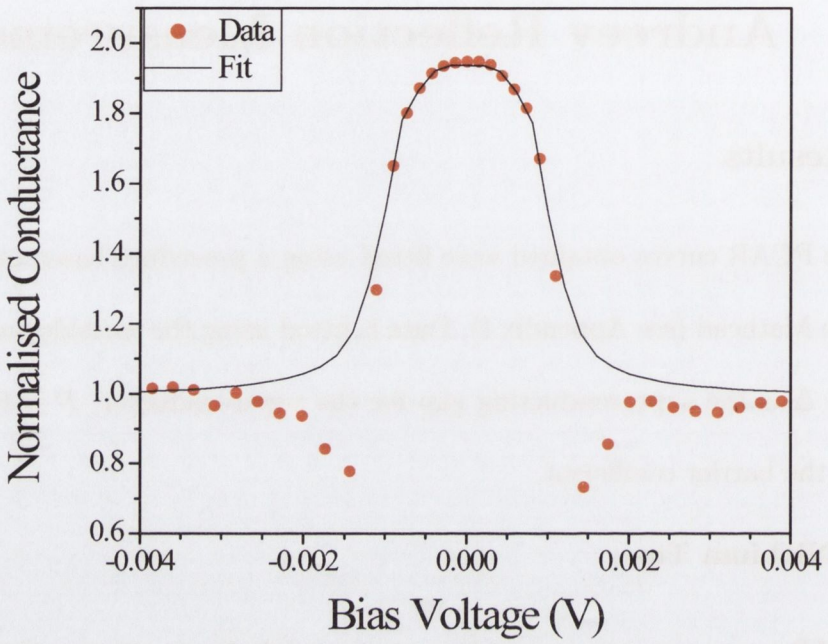

Figure 6.1 *Andreev reflection measurement carried out on a point contact between copper and niobium. The fit parameters were* $\Delta = 1.0$ *meV* , $P = 0$ *and* $Z = 0.08$.

The curve was fitted with a superconducting gap $\Delta = 1.0$ meV, which is much less than experimentally measured values for bulk niobium (1.35-1.5 meV) [2],[3]. The data clearly shows the presence of a dip in conductance around the superconducting gap energy. A temperature of 2K was used in the fit, which was the measurement temperature. The resistance of this particular contact was 1.2 Ω.

6.1.1.2 Cobalt

Measurements were carried out on point contacts between a cobalt film and a sharpened niobium tip (see fig. 6.2). The doubling of conductance below the superconducting gap is suppressed due to the spin polarisation of the ferromagnetic metal. A value of $P = 0.41$ is inferred from the data. The value for the superconducting gap ($\Delta = 1$ meV) used in the fit is less than the accepted value for niobium. A temperature of 4.2 K is used to fit the data,

which is also the experimental temperature.

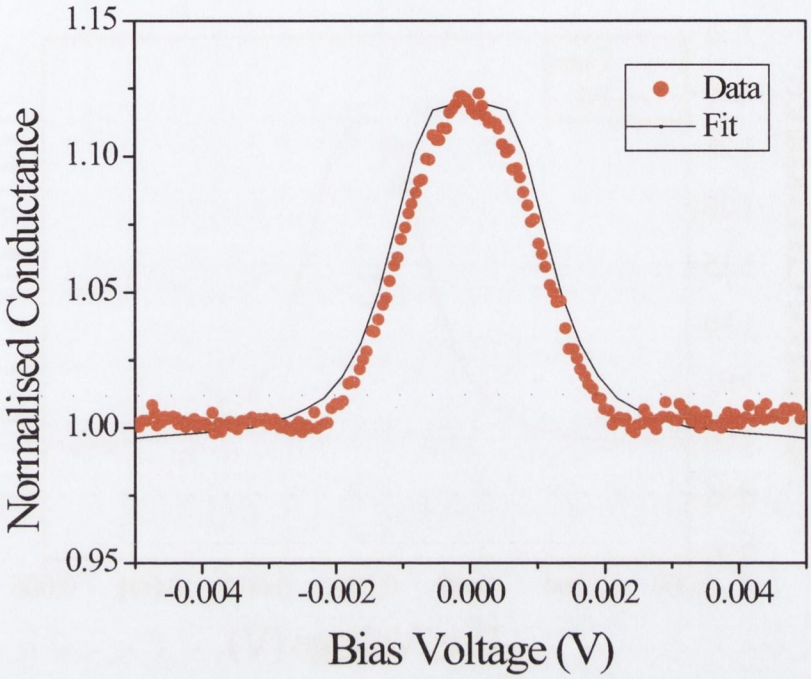

Figure 6.2 *Andreev reflection measurement carried out on a point contact between cobalt and niobium. The fit parameters were* $\Delta = 1.0\ meV$, $P = 0.41$ *and* $Z = 0.05$. *The resistance of the sample was 27* Ω.

6.1.1.3 Nickel

Measurements were carried out on a 60 nm film of nickel on a silicon oxide substrate. A value of 0.34 for the spin-polarisation was inferred from the data. Once again the data was fitted at the experimental temperature, 4.2 K, and a value of $\Delta = 1$ meV for the superconducting gap had to be used.

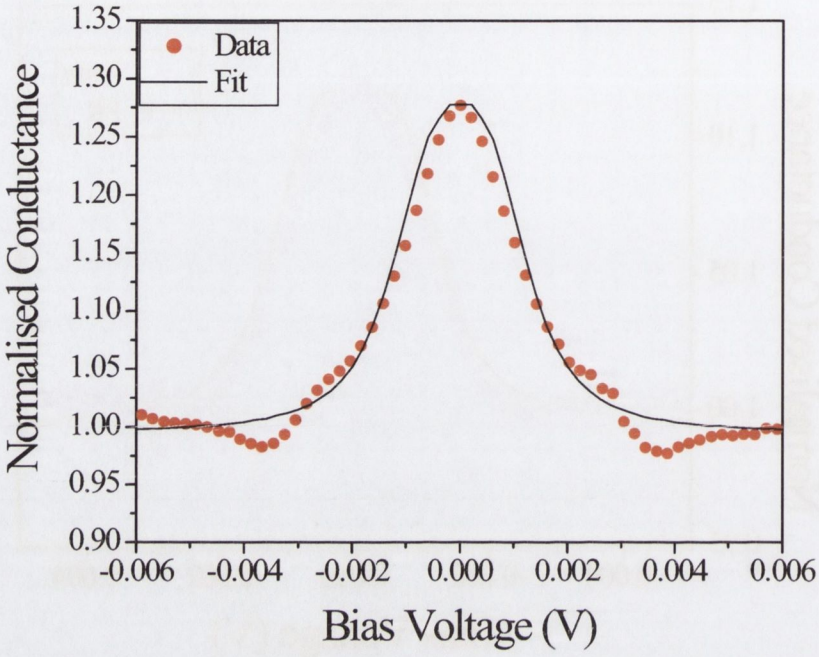

Figure 6.3 *Andreev reflection measurement carried out on a point contact between nickel and niobium. The fit parameters were* $\Delta = 1.0\ meV$, $P = 0.34$ *and* $Z = 0.04$. *The resistance of the sample was* $\approx 5\ \Omega$.

6.1.2 Lateral Nanojunctions

PCAR measurements were carried out on lateral nanojunctions. These junctions were made using the novel 8 step process outlined in section 3.5.3. Due to the difficulty in successfully creating these lateral junctions, only two materials were measured; copper and nickel. The superconducting layer consisted of 60 nm thick niobium film. This showed a superconducting transition at 6.4 K (see fig. 6.4), significantly less than the transition temperature in bulk niobium (9.2 K), however a reduced transition temperature is expected for a thin film of niobium [4]. The production of these lateral junctions is quite tricky and time consuming, and we had some difficulty in creating low resistance junctions.

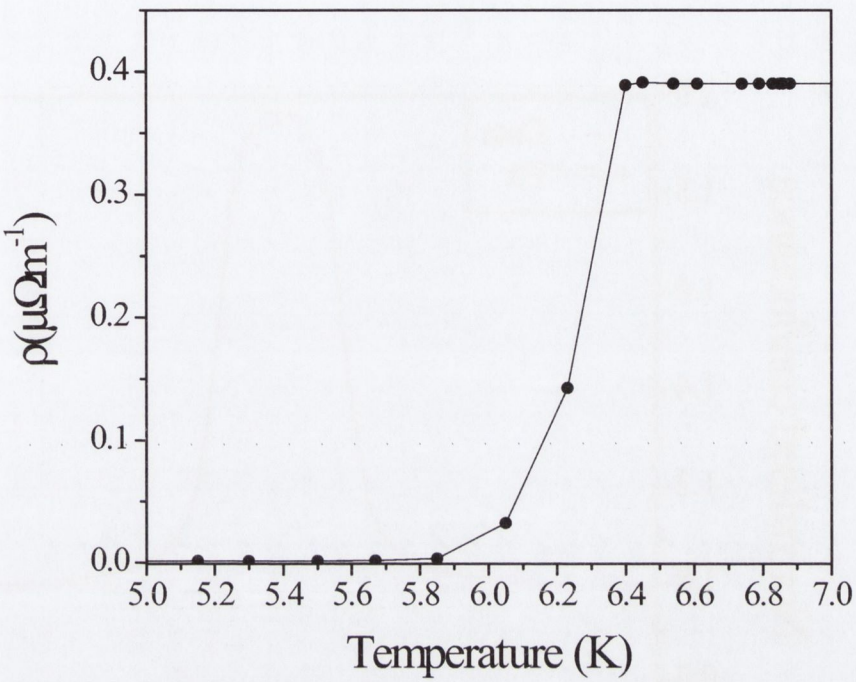

Figure 6.4 *The superconducting transition for a 60 nm Nb film is observed at 6.4 K.*

6.1.2.1 Copper

We successfully created a copper junction with a resistance of $\approx 350\ \Omega$ on which we were able to make some measurements (fig 6.5). The data obtained is very similar to that obtained using the niobium tip technique. A temperature of 2 K was required for the fitting, despite the fact the measurement took place at 4.2 K.

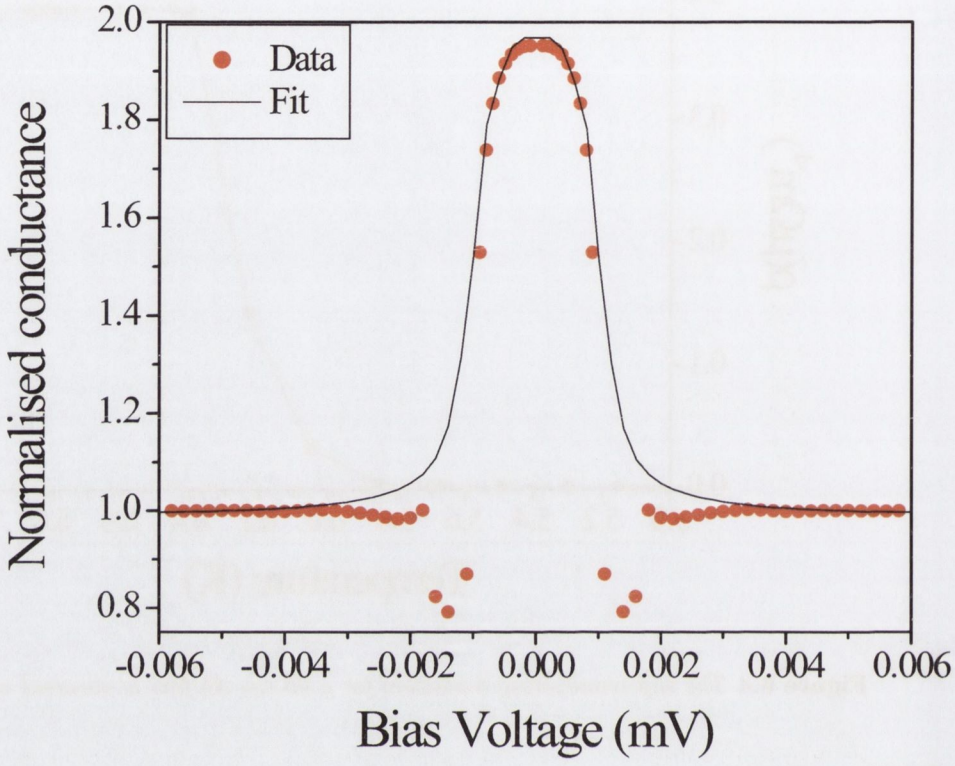

Figure 6.5 *Andreev reflection measurement carried out on lateral nanojunction between copper and niobium. The fit parameters were* $\Delta_1 = 1.0\ meV$, $P = 0$ *and* $Z = 0.01$.

6.1.2.2 Nickel

We were able to fabricate two nickel junctions with relative success. The first of these samples (fig 6.6) was highly resistive ($\approx 1\ k\Omega$), most likely due to a poor interface at the contact. This is reflected by the high value for the Z-parameter used to fit the data, indicating a strong barrier at the interface. Such a strong barrier would invariably lead to much spin-flip scattering at the interface, effectively eliminating any polarisation of the current.

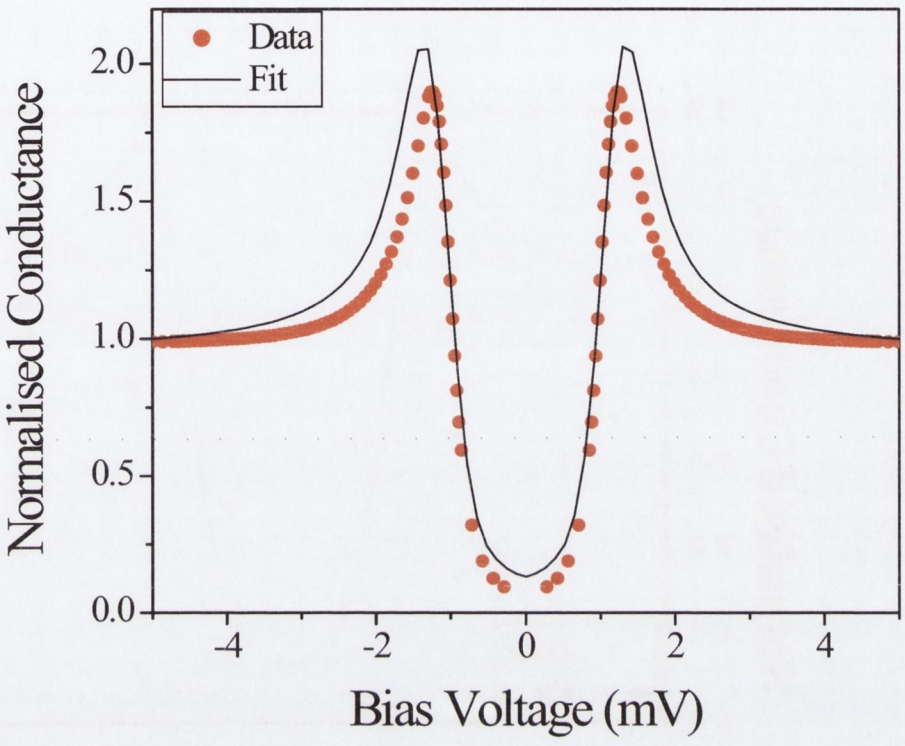

Figure 6.6 *Andreev reflection curve for a lateral Ni-Nb contact. The fit parameters were* $\Delta = 1.2\ meV$, $P = 0$ *and* $Z = 1.94$. *The resistance of the sample was* $\approx 1\ k\Omega$. *A temperature of 2 K was used in the data fit.*

The resistance of the second measurable sample (fig 6.7) was not as high ($\approx$100 Ω), however a high value of Z was still required to fit the data obtained. A value of 0.7 was obtained for the spin-polarisation in this sample. A temperature of 2 K was used for the fit, despite the measurement occurring at 4.2 K, as was the case for all of the lateral nano-junctions. The results for these junctions were presented at the Joint European Magnetism Symposium (JEMS) in Dresden, 2004 [11].

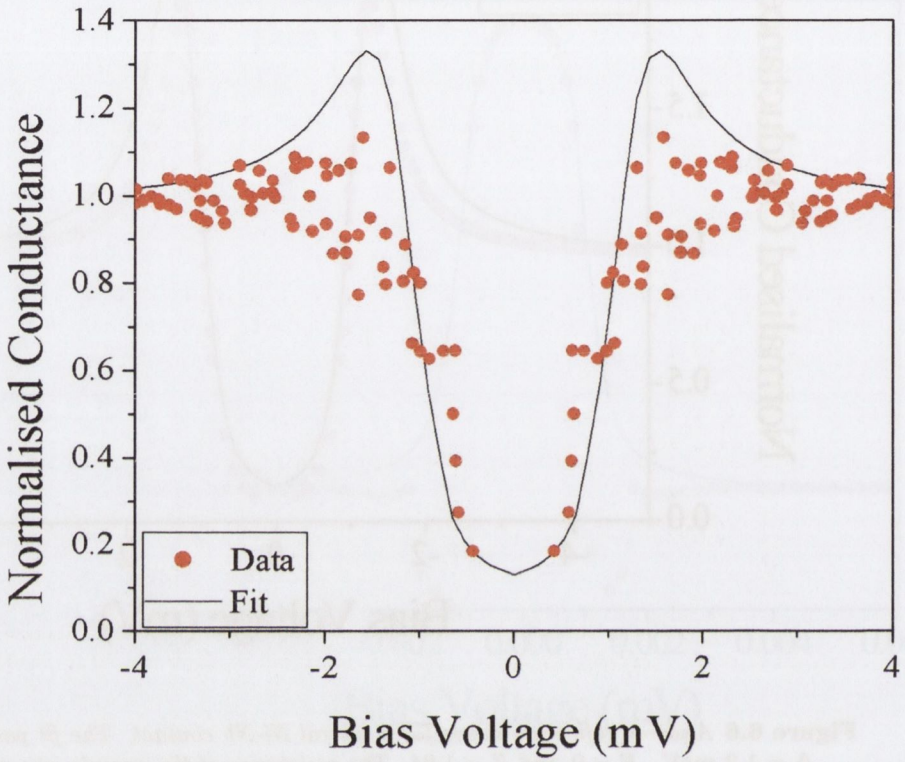

Figure 6.7 *Andreev reflection curve for a lateral Ni-Nb contact. The fit parameters were* $\Delta = 1.2$ *meV* , $P = 0.7$ *and* $Z = 1.0$. *A temperature of 2 K was used in the data fit.*

6.1.3 Nanocontacts deposited through nanoholes in PMMA

Andreev point contacts were created by depositing lead onto the subject material through a nanohole in PMMA, as described in section 3.5.2. A 150 nm lead layer was evaporated onto all samples, showing a transition temperature of 7.09 K, quite close to the expected value of 7.19 K [3]

6.1.3.1 Copper

Copper was studied firstly as a proof of concept to test the nanostructures. An increase of the conductance is clearly seen below the superconducting gap (fig 6.8). A fit of the data gave a value of 0.14 for Z. Once again the value used for Δ was lower than expected. A

temperature of 2 K was used in the data fit, which was the experimental temperature. Dips were observed around the superconducting gap.

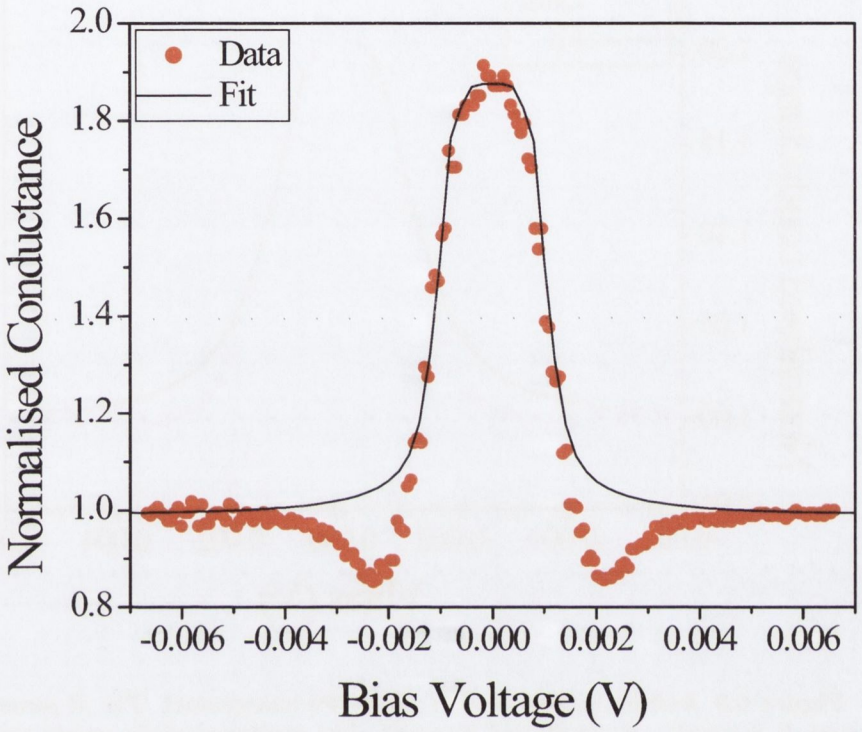

Figure 6.8 *Andreev reflection curve for Cu/Pb nanocontact. The fit parameters were* $\Delta = 1$ *meV* , $P = 0$ *and* $Z = 0.14$. *The resistance of the sample was* $\approx 3\ \Omega$. *A temperature of 2 K was used in the data fit.*

6.1.3.2 Nickel

Measurements were carried out on a 90 nm film of nickel on a silicon oxide substrate (fig 6.9). A value of 0.39 for the spin-polarisation was inferred from the data. The data was fitted using the experimental temperature of 4.2 K, and once more a lower value ($\Delta = 1$ meV) for the superconducting gap than expected had to be used.

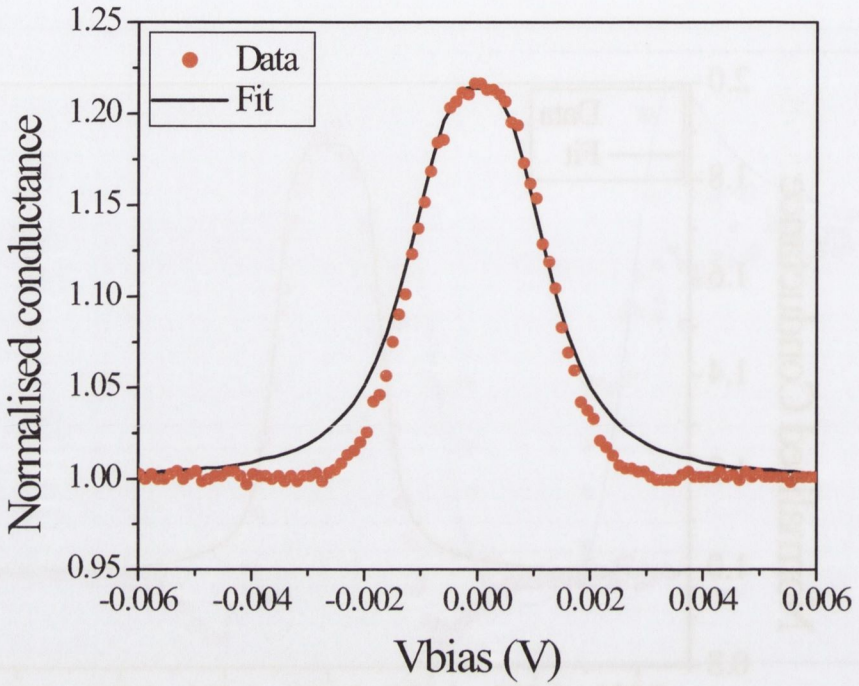

Figure 6.9 *Andreev reflection curve for Ni/Pb nanocontact. The fit parameters were* $\Delta = 1$ *meV* , $P = 0.38$ *and* $Z = 0.01$. *The resistance of the sample was* $\approx$ *14* Ω. *A temperature of 4.2 K was used in the data fit.*

6.1.3.3 Co_2MnSi

Measurements were carried out on films of Co_2MnSi grown a silicon substrate (fig 6.10). The films were post-annealed under vacuum at 500° C for 2 hours. A value of 0.2 was obtained for the spin-polarisation. Once again quite a low Z-value (0.12) was used in the fit, and the fitting temperature was the same as the measurement temperature.

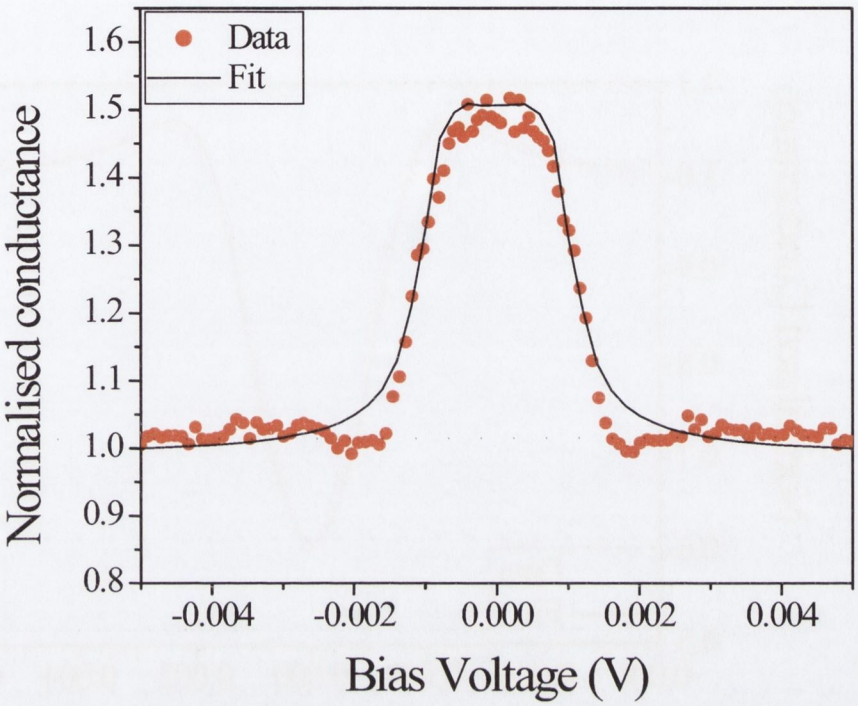

Figure 6.10 *Andreev reflection curve for Co_2MnSi/Pb nanocontact. The fit parameters were $\Delta = 1$ meV , $P = 0.20$ and $Z = 0.12$. The resistance of the sample was $\approx 14\ \Omega$. A temperature of 2 K was used in the data fit.*

6.1.3.4 ϵ-$Fe_{2-3}N$

Measurements were carried out on two 120 nm films of ϵ-$Fe_{2-3}N$. A typical curve form the first film is shown in fig. 6.11. The fit shows a spin polarisation of 0.58 and a value of 0.4 for Z. In this case a value of 1.4 meV was used for Δ. The fitting temperature was carried out at the same temperature as the experimental temperature i.e. 4.2 K.

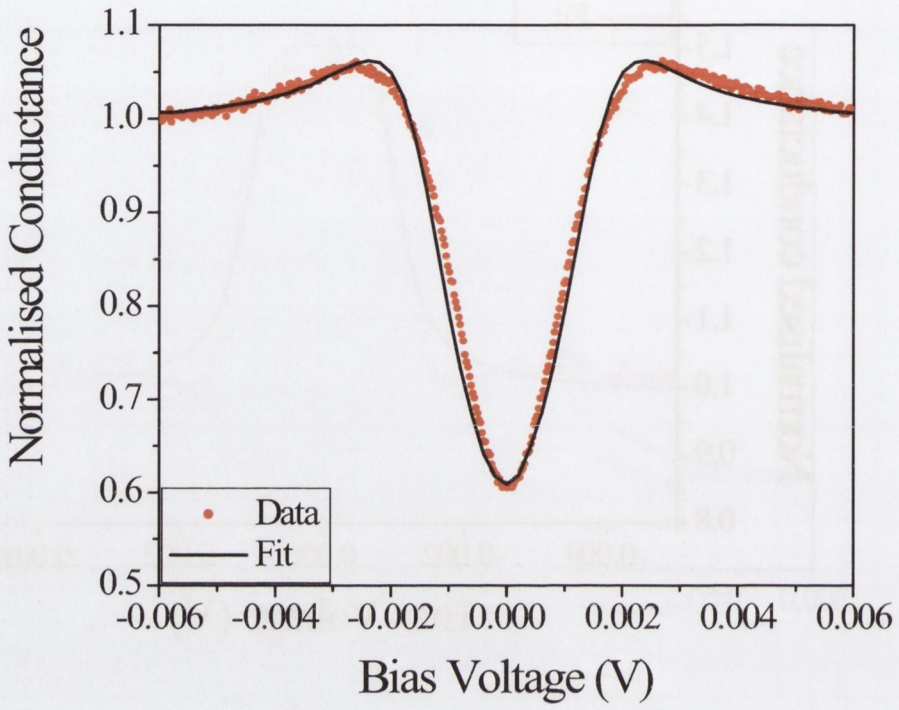

Figure 6.11 *Andreev reflection curve for $Fe_{2-3}N/Pb$ nanocontact (film #1). The fit parameters were $\Delta = 1.4$ meV , $P = 0.58$ and $Z = 0.40$. The resistance of the sample was $\approx$ 20 Ω. A temperature of 4.2 K was used in the data fit.*

Similar results were obtained on the second film (fig 6.12). Here a spin polarization of 0.53 was obtained, with a value of 0.1 for Z.

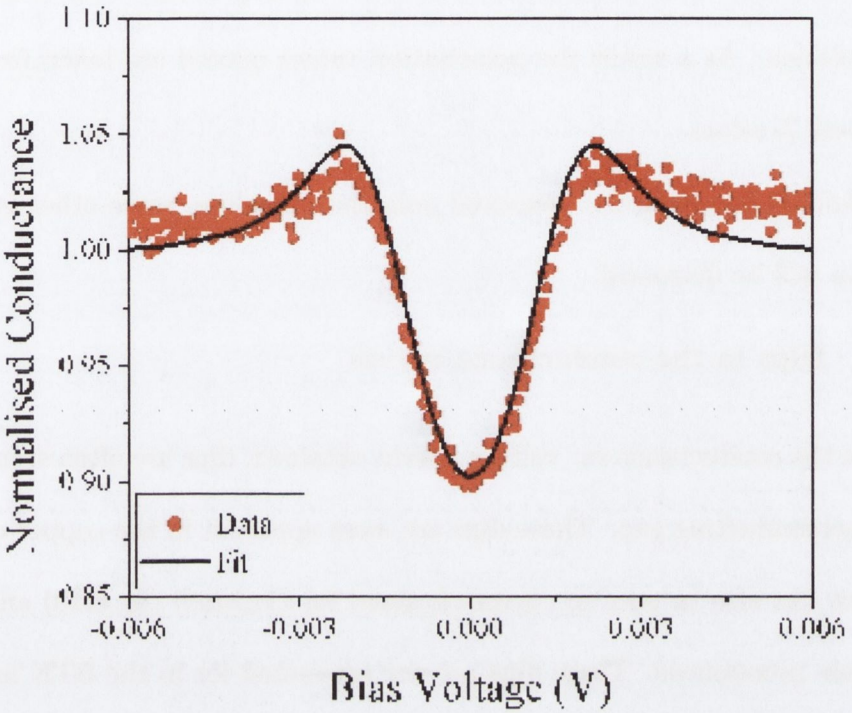

Figure 6.12 *Andreev reflection curve for $Fe_{2-3}N/Pb$ nanocontact (film #2). The fit parameters were $\Delta = 1.4$ meV , $P = 0.53$ and $Z = 0.10$. The resistance of the sample was $\approx 18\ \Omega$. A temperature of 4.2 K was used in the data fit.*

6.2 Discussion

Successful PCAR measurements were carried out using three different methods, giving polarisation measurements for various materials. All of the data obtained from the AFM indented nanocontacts showed a very low Z-value, characterised by the lack of a dip at zero bias in the conductance vs. voltage curves. The relationship between Z and P has been studied extensively (e.g. [5],[6], see section 2.2.3). It has been shown that curves with higher Z-values give lower polarisation values, presumably due to increased interface scattering due to a stronger barrier. It is common practice to obtain polarisation values for several different barrier strengths and extrapolate to Z = 0. However in this study we have tried to keep

the values of Z as low as possible in all our data (see [7]), thus eliminating the need for extrapolation. As a result the polarisation values quoted are taken from the samples with the lowest Z-values.

Before examining the measured polarisation values, some other issues that arose with the data will be discussed.

6.2.1 Dips in the conductance curves

In the conductance vs. voltage curves obtained, dips are often seen around the value of the superconducting gap. These dips are most apparent in the copper curves (figs. 6.1, 6.5, 6.8), but can also be seen in curves obtained for Co_2MnSi (fig 6.10) and Ni (fig 6.3), albeit much less pronounced. These dips are not accounted for in the BTK model. However their most likely cause is the proximity effect, where leaking of Cooper pairs from a superconductor into an adjacent material produces a superconducting layer in this material (see section 2.3). This superconducting proximity layer has a lower transition temperature and a lower Δ than the bulk. The Andreev reflection process, occurring at the metal/proximity-layer interface, is therefore limited to bias voltages smaller than the superconducting gap value of the proximity layer. However, quasiparticles can only enter the superconductor for voltages higher than the bulk gap of the superconductor. As a result a dip in the conductance would occur at energies between the superconducting gap of the proximity layer and that of the superconductor.

The Strijkers model [1] discussed in section 2.3 takes this proximity layer and incorporates it within the BTK model. Two superconducting gaps are used, one for the proximity layer (Δ_1) and one for the superconductor itself (Δ_2). This new model produces conductance curves that do indeed show dips around the superconducting gap (see figure 2.8).

We therefore refitted the data for copper from figure 6.1 using this model (see fig 6.13).

A pronounced proximity layer would be expected in a relatively clean (i.e. low Z value) contact such as this, as there would be very few impurities at the interface to impede the proximity effect. The model gives a very good fit for the dips, and indicates a value of 1.0 meV for the superconducting gap of the proximity layer and 1.60 meV for niobium, somewhat higher than the expected value. Thus it seems in fitting with the BTK model we are in fact using the superconducting gap of the proximity layer as opposed to that of the superconductor itself. The reason that these dips are not as pronounced in the magnetic samples is that ferromagnetism and the superconducting proximity effect are competing processes - ferromagnetism inhibits the formation of cooper pairs.

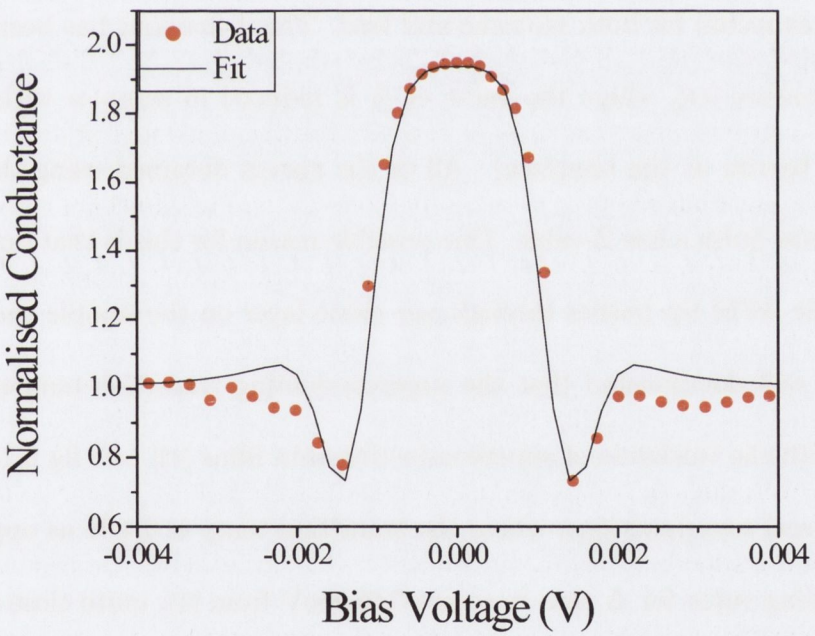

Figure 6.13 *A fit for a Cu/Nb andreev curve using a model that takes into account the proximity layer. The fitting parameters were* $Z = 0.08$, $P = 0$, $\Delta_1 = 1.0$ meV, $\Delta_2 = 1.60$ meV.

6.2.2 Reduced value of Δ

The transition temperature, T_C, for bulk niobium and lead are 7.19 K and 9.26 K

respectively. From BCS (Bardeen-Cooper-Schrieffer) theory [8] we can calculate the superconducting gap using

$$2\Delta \approx 3.5 k_B T_C. \tag{1}$$

This gives us values of 1.38 and 1.08 meV for the gaps of niobium and lead respectively. However recent studies suggest that lead may not always follow the BCS model very closely, and results from a study of the material using photoemission spectra give a value of 1.2 meV for the gap[3]. Other calculations [9] have indicated a gap of 1.36 meV for lead, and this value has been used in previous Andreev studies [10].

In many of the fitted curves, the value for the superconducting gap is significantly less than that expected for both niobium and lead. This behaviour has been reported elsewhere in the literature [14], where the value of Δ is reduced in samples with a low Z value (i.e. negligible barrier at the interface). All of the curves obtained using the AFM indentation method show quite a low Z-value. One possible reason for this is that during the indentation process, the AFM tip pushes through any oxide layer on the sample surface.

It is well documented that the superconducting transition temperature, and thus Δ, reduces with the thickness of superconducting thin films [12] (see fig 6.14). This is observed for the lateral nanojunctions, where the transition temp is 6.4 K as opposed to 9.2 K. The corresponding value for Δ thus becomes 0.95 meV from (1), quite close to the value used in the fitting.

One proposed explanation for this reduction is due to the so called scaling-theory [13]; in low dimensional metallic systems all ground state electrons become localised, however weak the disorder. This leads to a suppression of the superconducting density of states and an enhanced Coulomb repulsive interaction [16]. We have seen how this affects the

lateral nanojunctions; it may have a similar effect in the AFM indented nanocontacts and the niobium tip nanocontacts. Since we are dealing with nano-scale point contacts we can expect a reduction of the critical temperature localised at the contact itself. However this would not effect the rest of the sample, and a sharp drop in resistance will still be seen at the bulk transition temperature.

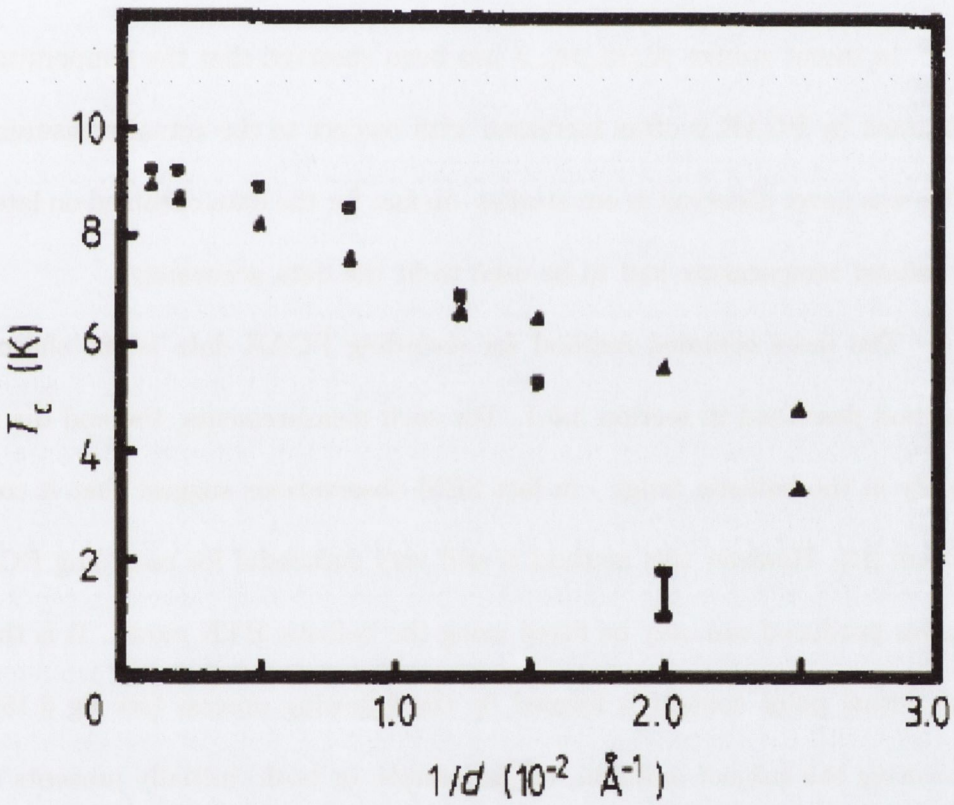

Figure 6.14 *Relationship between transition temperature and film thickness, d, for single crystal (squares) and polycrystalline (circles) Nb thin films (from Jiang et al* [4]*).*

Another possible reason for the reduced values of Δ is the proximity effect, as discussed in the previous section - we may actually be fitting to the gap value of a proximity layer as opposed to that of the superconductor. This may also explain why the trend observed by Miyoshi et al. [14] showed the reduction to be less pronounced for contacts with a higher Z-value, as a stronger barrier at the interface would impede the superconducting proximity

effect. This would explain the use of a more acceptable value for Δ in the $Fe_{2-3}N$ data. Since the material shows a much higher level of polarisation, the proximity effect is more likely to be eliminated - a reduction in the Andreev reflection process generally means a suppression of the proximity effect, since both require electrons of both spin.

6.2.3 Value of fitting temperature

In recent studies [6],[15],[18], it has been observed that the temperature used to fit data obtained by PCAR is often increased with respect to the actual measurement temperature. This was never observed in our studies - in fact for the data obtained on lateral nanojunctions a *reduced* temperature had to be used to fit the data accurately.

The most common method for recording PCAR data is the sharpened niobium tip method described in section 3.5.1. For such measurements, the end diameter of the tip is rarely in the ballistic range - in fact SEM observations suggest that it could be as large as 50 μm [17]. However this method is still very successful for recording PCAR data, and the curves produced can only be fitted using the ballistic BTK model. It is therefore likely that the actual point contact is formed by the following process (see fig 6.15). An oxide layer (covering the subject material, or the sample, or both) initially prevents metallic transport across the interface. Pressure between the tip and the substrate causes cracks or weak spots to appear in the oxide layer. Application of a potential difference across the contact causes a breakdown across the oxide at these weak spots, and conduction can now occur. The breakdown voltage for the oxide would be relatively low, since the thickness of this layer would be quite thin (of the order of nanometers), especially at these weak spots.

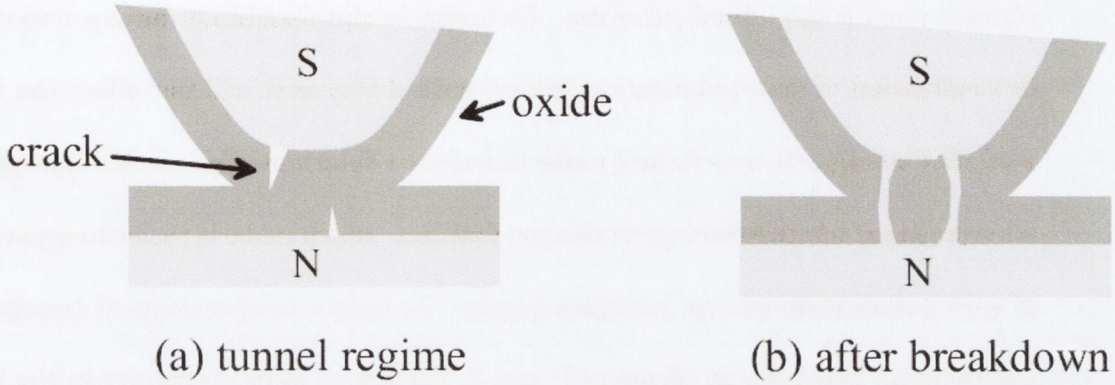

Figure 6.15 *Possible scenario allowing formation of point contacts between a niobium tip and a sample. Pressure from the tip causes weak spots to form in the oxide layer. Breakdown then occurs across the oxide layer, allowing conduction paths to form.*

In such a scenario it is likely that there are in fact many parallel conduction paths formed between the superconductor and the subject material, and thus the measured spectra are the superposition of the characteristics of these paths. This averaging would spread the features of the PCAR curves in a similar manner to thermal broadening, and a larger temperature would thus have to be used in the fitting. This idea was discussed in Bugoslavsky et al. [18]

In both the lateral nanojunctions and the AFM indented nanocontacts there is only one conduction path present. As a result the broadening mentioned above will not occur and no increase is required for the fitting temperature. In our niobium tip method, a piezo-actuator is used to control the size of the point contact. This is in contrast to most set-ups reported in the literature where the contact size is controlled using just a micrometer screw gauge. It is thus likely that in our set-up the physical size of the point contact is of the order of nanometers, and thus multiple conduction paths will not be formed.

However this does not explain why the fitting temperature used is less than the exper-

imental one for the lateral junctions. Fortunately this should not have a major effect on the determination of spin-polarisation from the data fits, as it will not affect the conduction at zero bias voltage. It may in fact make it easier to determine the correct spin-polarisation, as a lower fitting temperature gives sharper features, which make it easier to separate the effects of spin polarisation and an interface barrier. At higher temperatures it becomes difficult to discriminate between the effects of P and Z, leading to some ambiguity in the interpretation of the PCAR curves.

6.2.4 Spin polarisation values

Spin polarisation was measured in Cu, Ni, Co and Co_2MnSi using the three different methods. In all three methods, fits to the copper data showed zero polarisation, supporting the validity of the three different techniques. The value obtained for cobalt using a niobium tip (0.41) is quite reasonable, comparing well to quoted literature values (see table 8.1). The same can be said for those obtained for nickel using both the niobium tip and the AFM indentation method, giving 0.34 and 0.39 respectively.

	Nb tip	**Lateral nanojunction**	**AFM indented nanocontact**	**Literature**
Ni	0.34	0.7	0.39	0.32 [10], 0.37 [1]
Co	0.41	-	-	0.37 [10], 0.46 [20]
Co_2MnSi	-	-	0.2	0.55 [21], 0.50-0.60 [22]
$Fe_{2-3}N$	-	-	0.60	-

Table 6.1 *Polarisation values obtained for various materials in this work and in the literatur*

However the value obtained for nickel using the lateral nanojunction, P=0.70, is much greater than reported elsewhere. Our proposed explanation is the presence of nickel oxide at the interface. The absorption of *s* electrons by the oxygen atoms of the NiOx layer and the

local narrowing of the d band in the nanostructure could have a spin filtering effect on the electrons, enhancing the polarisation of the current [23]. It is also possible that the difference in polarisation measured here is because we are measuring the current parallel to the film, whereas all of the measurements in the literature have had the current perpendicular to the plane of the film.

The polarisation value obtained for Co_2MnSi (P=0.2) using the AFM indented nanocontact method is somewhat disappointing for a material predicted to be a fully-polarised half metal. This low value could be explained by antisite disorder, particularly between the Co and Mn atoms, which have a similar atomic radius. Studies have shown Co-Mn site swapping of up to 18 % for this material [22]. While the literature has reported higher values, it still is nowhere near 100 %. In fact a recent study by Wang et al. estimated a polarisation value of only 0.12 at the Fermi level using spin-resolved photoemission spectra [24].

The maximum values of polarisation observed for the $Fe_{2-3}N$ samples were 0.58 and 0.53 for the first and the second films respectively. The value for the first film is surprisingly high, especially considering the relatively low moment of the films (0.18 μ_B/f.u.). The presence of small amounts of the paramagnetic ζ-Fe_2N may account for a lowering of this value; the moment at the actual point contact may be slightly higher. It is possible that, while the overall band structure of the material may not show significant spin-polarisation, the actual charge carriers do. This could occur if an electron band with high-mobility was spin polarised, for example. In PCAR it is the spin polarisation of the current itself we are measuring, not the actual density of states. However considering the similar value obtained for the second film, which had a much higher moment, the former scenario is more likely. No band structure calculations showing any of the iron nitrides to be half-metallic have been

reported in the literature ([25] calculates no half-metallicity in Fe_3N). However, since it is so difficult to accurately determine the nitrogen concentration in $Fe_{2-3}N$, a realistic density of states would be extremely hard to calculate.

References

[1] G. J. Strijkers, Y. Ji, F. Y. Yang, C. L. Chien, and J. M. Byers, Phys. Rev. B **63**, 104510 (2001).

[2] A. Yazdani, B. A. Jones, C. P. Lutz, M. F. Crommie, D. M. Eigler, Science **275**, 1767 (1997).

[3] A. Chainani, T. Yokoya, T. Kiss, and S. Shin, Phys. Rev. Lett. **85**, 1966 (2000).

[4] Q. D. Jiang, Y. L. Xie, W. B. Zhang, H. Gu, Z. Y. Ye, K. Wu, J. L. Zhang, C. Y. Li and D. L.Yin, J. Phys.: Condens. Matter **2,** 3567 (1990).

[5] G. T. Woods, R. J. Soulen, Jr., I. Mazin, B. Nadgorny, M. S. Osofsky, J. Sanders, H. Srikanth, W. F. Egelhoff, and R. Datla, Phys. Rev. B **70**, 054416 (2004).

[6] C. H. Kant, O. Kurnosikov, A. T. Filip, H. J. M. Swagten, and W. J. M. de Jonge, J. Appl. Phys. **93,** 7528 (2003).

[7] J. Sanders, G. T. Woods, P. Poddar, H. Srikanth, B. Dabrowski and S. Kolesnik, J. Appl. Phys. **97,** 10C912 (2005).

[8] For a good introduction to superconductivity and the BCS theory, see Introduction to Superconductivity by Michael Tinkham, McGraw-Hill (1975)

[9] W. L. McMillan and J. M. Rowell, Phys. Rev. Lett. **14**, 108 (1965).

[10] S. K. Upadhyay, A. Palanisami, R. N. Louie, and R. A. Buhrman, Phys. Rev. Lett. **81**, 3247 (1998).

[11] O. Céspedes, E. Clifford, and J. M. D. Coey, J. Magn. Magn. Mat. **290-291**, 113 (2005).

[12] M. S. M. Minhaj, S. Meepagala, J. T. Chen, and L. E. Wenger, Phys. Rev. B **49**, 15235

(1994).

[13] P. W. Anderson, E. Abraham and T. V. Ramakrishan, Phys. Rev. Lett. **43,** 718 (1979).

[14] Y. Miyoshi, Y. Bugoslavsky, and L. F. Cohen, Phys. Rev. B **72**, 012502 (2005).

[15] B. Nadgorny, R. J. Soulen Jr.,, M. S. Osofsky, I. I. Mazin, G. Laprade, R. J. M. van de Veerdonk, A. A. Smits, S. F. Cheng, E. F. Skelton, and S. B. Qadri, Phys. Rev. B **61**, R3788 (2000).

[16] S. Maekawa and H. Fukuyama, J. Phys. Soc. Jpn. **51**, 1380 (1981).

[17] Y. Bugoslavsky, Y. Miyoshi, G. K. Perkins, A. D. Caplin, L. F. Cohen, A. V. Pogrebnyakov, and X. X. Xi, Phys. Rev. B **69**, 132508 (2004).

[18] Y. Bugoslavsky, Y. Miyoshi, S. K. Clowes, W. R. Branford, M. Lake, I. Brown, A. D. Caplin, and L. F. Cohen, Phys. Rev. B **71**, 104523 (2005).

[19] T. Block, C. Felser, G. Jakob, J. Ensling, B. Mühling, P. Guütlich, and R. J. Cava, J. Solid State Chem. **176,** 646 (2003).

[20] C. H. Kant, O. Kurnosikov, A. T. Filip, P. LeClair, H. J. M. Swagten, and W. J. M. de Jonge, Phys. Rev. B **66**, 212403 (2002).

[21] L. D. Ritchie, G. Xiao, Y. Ji, T. Y. Chen, C. L. Chien, M. Zhang, J. Chen, Z. Liu, G. Wu and X. X. Zhang, Phys. Rev. B **68**, 104430 (2003).

[22] S. F. Cheng, B. Nadgorny, K. Bussmann, E. E. Carpenter, B. N. Das, G. Trotter, M. P. Raphael, and V. G. Harris, IEEE Trans. Mag., **37**, 2176 (2001).

[23] N. Papanikolau, J.Phys.: Cond. Mat. **15,** 5049 (2003); N. García, cond-mat/0207323 (2002).

[24] W. H. Wang, M. Przybylski, W. Kuch, L. I. Chelaru, J. Wang, Y. F. Lu, J. Barthel, H.

L. Meyerheim, and J. Kirschner, Phys. Rev. B **71**, 104416 (2005).

[25] S. Matar, B. Siberchicot, M. Penicaud, and G. Demazeau, J. Phys. I France **2,** 1819 (1992).

Chapter 7

Conclusion and Future Work

The study presented in this thesis has been concerned with measuring spin polarisation in magnetic materials. Materials have been examined using room temperature point contacts and Andreev reflection. Two novel Andreev techniques for measuring spin-polarisation have been developed successfully.

7.1 Point Contacts

The magneto-transport properties of several materials have been examined using point contacts. It has been proposed that the huge values of magnetoresistance observed in these point contacts are caused by spin-polarised transport through a domain wall, as well as spin-polarised tunneling transport, between two crystallites. A maximum spin polarisation has been inferred using the Jullière formula (chapter 1, equation (6)); these are tabulated below.

Material	Spin Polarisation
Polycrystalline magnetite	0.93
Gold-plated magnetite	0.89
Sr_2FeMoO_6	0.11
MnBi	0.87
$Co_2Cr_{0.6}Fe_{0.4}Al$	0.81

These measurements provide a simple and fast method to get a rough estimation of the spin polarisation of a ferromagnet at room temperature and thus determine its suitability for use in spintronics devices. This method can thus be used to examine the new potentially high spin-polarised materials that are constantly appearing in the scientific community, such as

Co_2FeSi [1] and Co_2FeGa [2], [3]. These are both Heusler alloys with high Curie temperatures and thus show great promise for spintronics applications - Co_2FeSi shows the highest Curie temperature (1100 K) and magnetic moment (6 μ_B) of any potential half-metal. The work could also be extended to lower temperatures to examine, for example, the relationship between spin polarisation and temperature in different materials.

The set-up could also be modified to measure breaking contacts in a similar manner to that described by Viret et al [4]. This would allow us to examine polarisation in thin films as well as bulk crystallites, where the structure is well defined.

7.2 Andreev Reflection

Two novel methods of recording point contact Andreev reflection data were developed and compared with the established method. In the lateral nanojunctions, nickel was measured with some success. The difficulty in producing these junctions meant that very few reliable samples could be produced. The lift-off process required was rarely fully successful, often leaving a poorly defined interface. However this could be overcome by making use of electron lithography processes, which are better equipped for creating features on a nanometre scale. Another problem encountered was thermal contraction of the two films as the samples were cooled towards the transition temperature of the superconductor. The strain often proved too great for the samples, and many of them broke before any Andreev measurements could be made. This method would therefore be more suitable in examining materials with a low thermal expansion coefficient.

The AFM indented nanocontacts proved to be very succesful for recording PCAR data. Once the procedure had been optimised, samples could be produced with relative ease. These had many advantages over using the standard niobium tip method. The samples are robust

and could be measured several times and then stored. The nanohole produced by the tip can be imaged, thus giving us an idea of its diameter and its profile. Only one conduction path is present, thus reducing the 'smearing' effect that multiple paths have on the curve features, and enabling a more reliable fit. Also, most of the samples produced by this method gave a very low Z value, indicating a low barrier. It is acknowledged that such measurements give a more accurate value for the spin-polarisation of the material as there is less likelihood of spin-scattering events.

The AFM indentation method could be developed further in a variety of ways. Different tips could be used to give holes of different profiles, enabling us to see the effect this would have on the Andreev curves and on superconducting nanocontacts in general. Also multiple channels could be deliberately produced to see what effect this would have on the 'smearing' of the PCAR curve features.

The high value of spin polarisation observed in the iron nitride films show that it could be suitable for spin-electronics applications, and certainly warrants further investigation. Its suitability for use in structures such as spin valves and magnetic tunnel junctions could be examined; the facilities to make such structures are available in our laboratory. It may be interesting to directly probe the density of states of the material using spin-resolved photoemission spectroscopy, to see if its band-structure reflects the spin polarisation observed. Single phase films of the material could also be made with differenty nitrogen concentrations, allowing us to study the spin polarisation as a function of the nitrogen concentration..

Further studies on these films could also be carried out using Mössbauer studies. It is possible that the moment of the iron atoms are much higher than the magnetisation curves indicate, but that the overall moment is reduced by an uncompensated antiferromagnetic

structure. This would be confirmed by a strong hyperfine field for the Fe-57 isotopes. Otherwise the large spin polarization may be mainly due to the 4s electrons (or due to N holes).

Further materials could be examined using this method, such as the Heusler alloys mentioned in the previous section. Also much interest has arisen recently in magnetic semiconductors [5]. This method could be developed to study spin polarisation materials. This may require doping of the semiconductor to increase its conductance, thus reducing the effects of series resistance and improving the transparency of the interface. Also some recent PCAR studies of magnetic semiconductors [6] indicate that some modifications of the BTK theory may have to made to accommodate the physics involved.

References

[1] S. Wurmehl, G. H. Fecher, H. C. Kandpal, V. Ksenofontov, C. Felser, H. Lin, J. Morais, cond-mat/0506729 (2005).

[2] M. Zhang, E. Bruck, F. R. de Boer, Z. Li, and G. Wu, J. Phys. D: Appl. Phys. **37,** 2049 (2004).

[3] K. Kobayashi, R. Y. Umetsu, A. Fujita, K. Oikawa, R. Kainuma, K. Fukamichi, and K. Ishida, J. All. Comp. **399**, 60 (2005).

[4] M. Viret, S. Berger, M. Gabureac, F. Ott, D. Olligs, I. Petej, JF Gregg, C. Fermon, G. Francinet, and G. Le Goff, Phys. Rev. B **66**, 220401 (2002).

[5] J. M. D. Coey, M. Venkatesan and C. B. Fitzgerald, Nature Materials **4**, 173 (2005).

[6] R.P. Panguluri, K.C. Ku, T. Wojtowicz, X. Liu, J.K. Furdyna, Y.B. Lyanda-Geller, N. Samarth, and B. Nadgorny, Phys. Rev. B **72**, 054510 (2005).

Appendix I: Fitting Procedure for Andreev Reflection data

$T := 4.2$ temperature

$Ef := 0$

$Pc := 0.2$ polarisation

$\Delta := 1 \cdot 10^{-3}$ superconducting gap

$Z := .12$ height of scattering barrier

$k := 8.6317 \cdot 10^{-5}$ Boltzmann in electron volts

$$f(E) := \frac{1}{e^{\frac{E - Ef}{k \cdot T}} + 1}$$ Fermi function

Below are the equations for determinig probabilities of Andreev reflection, normal backscattering etc as defined in Strijkers paper

$$\varepsilon(E) := \frac{E}{\sqrt{E^2 - \Delta^2}}$$

$$A1(E) := \frac{\Delta^2}{E^2 + \left(\Delta^2 - E^2\right) \cdot \left(1 + 2 \cdot Z^2\right)^2}$$

$$A2(E) := \frac{\varepsilon(E)^2 - 1}{\left[\varepsilon(E)^2 + \left(1 + 2 \cdot Z^2\right)\right]^2}$$

$$B1(E) := 1 - A1(E)$$

$$B2(E) := 4 \cdot Z^2 \cdot \frac{\left(1 + Z^2\right)}{\left[\varepsilon(E)^2 + \left(1 + 2 \cdot Z^2\right)\right]^2}$$

$$A(x) := \begin{cases} A1(x) & \text{if } |x| < \Delta \\ A2(x) & \text{if } |x| \geq \Delta \end{cases}$$

$$Bunp(x) := \begin{cases} B1(x) & \text{if } |x| < \Delta \\ B2(x) & \text{if } |x| \geq \Delta \end{cases}$$

$$Bpol(x) := \begin{cases} 1 & \text{if } |x| < \Delta \\ \frac{B2(x)}{1 - A2(x)} & \text{if } |x| \geq \Delta \end{cases}$$

$$I\_unp(V) := \int_{-.0015}^{.0105} (f(E - V) - f(E)) \cdot (1 + A(E) - Bunp(E))\, dE$$ unpolarised current

$$I\_pol(V) := \int_{-.0015}^{.0105} (f(E - V) - f(E)) \cdot (1 - Bpol(E))\, dE$$ polarised current

$I(V) := (1 - Pc) \cdot I\_unp(V) + Pc \cdot I\_pol(V)$ total current

$i := 1 .. 100$

$da := 0.0002001$

$a_0 := -.01$

$a_i := a_{i-1} + da$ creates bias voltage values

$$p(x) := \begin{cases} I(x) & \text{if } x > 0 \\ -I(-x) & \text{if } x < 0 \\ 0 & \text{if } x = 0 \end{cases}$$

$$G(V) := \frac{d}{dV} p(V)$$

$$out_i := \frac{\overrightarrow{G(a_i)}}{G(.008)}$$ normalised conductance

$data := augment(a, out)$

WRITEPRN("D:\Andreev\fits\Fit1.dat") := data

Appendix II: List of Publications

1. "Magnetoresistance in point contacts of the Heusler alloy $Co_2Cr_{0.6}Fe_{0.4}Al$" E. Clifford, M. Venkatesan, R. Gunning and J. M. D. Coey, Solid State Communications **131,** 61 (2004).

2. "Large magnetoresistance in MnBi point contacts" E. Clifford, M. Venkatesan, J.M.D. Coey, Journal of Magnetism and Magnetic Materials **272 – 276,** 1614 (2004).

3. "Spin polarization of nickel measured by Andreev reflection in planar thin film nanocontacts", O. Céspedes, E. Clifford, and J.M.D. Coey, Journal of Magnetism and Magnetic Materials **290-291**, 113 (2005).

4. "Magnetoresistance of magnetite point contacts and nanoconstrictions" O. Céspedes, E. Clifford, and J. M. D. Coey, Journal of Applied Physics **97**, 064305 (2005)

5. "Magnetoresistance of nickel nanocontacts fabricated by different methods" H.Wei, R. Langford, T.Wang, E. Clifford, X. Han and J. M. D. Coey, Journal of Applied Physics, to be published.

6. "Study of magnetotransport in nickel nanocontacts" R. Langford, T.Wang, E. Clifford, H.Wei, X. Han and J. M. D. Coey, submitted to Nanotechnology

7. "Point Contact Andreev Reflection by nanoindentation of PMMA", E. Clifford and J.M.D. Coey, submitted to Applied Physics Letters